Summer 7-29-2019

The Production Cross Section of the J/ψ Meson Measured Using the PHENIX Detector at $\sqrt{s}$ =510 GeV

Katherine Marie DeBlasio
University of New Mexico

Katherine M. DeBlasio

Candidate

Physics and Astronomy

Department

This dissertation is approved, and it is acceptable in quality and form for publication:

Approved by the Dissertation Committee:

Dr. Douglas E. Fields , Chairperson

Dr. Rouzbeh Allahverdi

Dr. Michael Gold

Dr. Adam Hecht

The Production Cross Section of the J/ψ Meson Measured Using the PHENIX Detector at $\sqrt{s} = 510$ GeV

by

Katherine M. DeBlasio

B.S., Physics, Rensselaer Polytechnic Institute, 2011
M.S., Physics, University of New Mexico, 2014

DISSERTATION

Submitted in Partial Fulfillment of the
Requirements for the Degree of

Doctor of Philosophy
Physics

The University of New Mexico

Albuquerque, New Mexico

December, 2019

Dedication

To my mother, Diane, who introduced me to the wonders of science.

Acknowledgments

I would like to thank my advisor, Professor Douglas E. Fields, for his support, motivational talks and stimulating conversation. Thanks for keeping me going when I needed a pep talk. Alisa, thanks for keeping the graduate students in line, and making sure we all know what we need to do.

For my colleagues at Los Alamos National Lab, I would like to thank Cesar L. Da Silva, Matt Durham, Sanghoon Lim, Xuan Li, Ming Liu, Melynda Brooks, and Pat McGaughey for mentoring me on this analysis. Without your guidance and friendship, this would not have been possible. Cesar, thank you one thousand times for mentoring me on muon analyses, working with me on the Muon Tracker efficiencies, and sharing your coffee, time, and funny stories. You have made this journey infinitely more enjoyable. Sanghoon, thank you for your guidance on simulations and the MuID efficiency studies. Thank you Matt for teaching me about the Crystal Ball function. Thank you Ming for having me up as a summer student. Pat, thanks for inviting me to stay at your place when I would come up to LANL.

Many thanks to Gregory Ottino, for your collaboration on the Vernier Scan analysis. I am looking forward to seeing your contributions to science in the future. Additionally, I would like to thank PHENIX collaborators Michael Beaumier, Amaresh Datta, Itaru Nakagawa, and Martin Purshke for your indispensable insight.

To my family and friends, thank you for your unwavering support and love. Without you all, this dissertation would never have been completed. To my parents, thank you for listening when I had a hard day, and encouraging me to keep going. Thank you Paytsar Ayvazyan and Eugene DeBlasio for helping me to achieve this life goal. I would like to thank my aunts, uncles and cousins for listening, encouraging, and helping to realize the importance of my work. Chris, Rachel and Matt, thank you for taking me in, believing in me, and giving me the time I needed to finish this work. I don't know what I would do without you. Genevieve, Satomi, Andy, Kendra, Matthias, Julian, Esther, Frank, and Nathaniel, thank you for your empathy, long walks and hikes, friendship and tea.

The Production Cross Section of the J/ψ Meson Measured Using the PHENIX Detector at $\sqrt{s} = 510$ GeV

by

Katherine M. DeBlasio

B.S., Physics, Rensselaer Polytechnic Institute, 2011
M.S., Physics, University of New Mexico, 2014

Ph.D., Physics, University of New Mexico, 2019

Abstract

The inclusive differential production cross section of the J/ψ meson is measured with the PHENIX detector for $p + p$ collisions at $\sqrt{s} = 510$ GeV using the 2013 RHIC dataset. The measurement is performed using the dimuon decay channel at forward and backward rapidity ranges of $1.2 < |y| < 2.2$ and for transverse momenta up to 12 GeV/c. The experimental results are compared to current predictions in NRQCD and serves to shed light on the ambiguity of the J/ψ production mechanism. The 2013 RHIC dataset provides unique challenges to the cross section measurement due to the effects of detector pile-up from multiple collisions. Techniques to quantify these effects are discussed.

Contents

List of Figures

List of Tables

Glossary

RHIC	Relativistic Heavy Ion Collider
PHENIX	Pioneering High Energy Nuclear Interaction eXperiment
BBC	Beam Beam Counter
MB	Minimum Bias
ZDC	Zero Degree Calorimeter
PISA	GEANT3 simulator as applied to PHENIX
σ_{BBC}	Cross section of the Minimum Bias trigger of the BBC
MUID	Muon Identifier
MuTr	Muon Tracker
MUID2D	Muon Identifier's 2 deep trigger for 2 muons passing the fourth gap in the MUID in an event.
FVTX	Forward Silicon Vertex Tracker
CERN	European Organization for Nuclear Research

Chapter 1

Introduction

After decades of measurements combined with theoretical models, the production mechanism of the J/ψ meson remains unknown. Theoretical models of the production mechanism aim to explain the hadronization of the J/ψ in particle collisions. Mathematical techniques and other experiments all contribute to the calculation of these models and are discussed in the next chapter. Previous results from RHIC[1, 2], TEVATRON[3] and LHC indicate that J/psi production is dominated by octet wave functions. However, polarization measurements indicate that singlet states might be dominant. This result fills in between previous 200 GeV results at RHIC [4] and 1.1 TeV at TEVATRON[5], which can help in solve the charmonia production puzzle. Theoretical predictions and how they are calculated are discussed in Chapter 2.

To test these theoretical models and measure the cross section of the J/ψ meson, the Relativistic Heavy Ion Collider at Brookhaven National Laboratory is used to collide protons at center of mass energies of 510 GeV. The Pioneering High Energy Interaction eXperiment (PHENIX) is the detector used to detect proton collisions and measure the dimuons decaying from the J/ψ meson. The Muon Arm Spectrometers are utilized, as well as the vertex tracking upgrade, the Forward Silicon Vertex

detector (FVTX). The experimental apparatus is discussed in Chapter 3.

Analysis of the RHIC 2013 proton-proton dataset requires calculations of correction factors to the J/ψ yield. This includes measurements of PHENIX Muon Arm detector acceptance and reconstruction efficiency, as well as the efficiency of the muon trigger used to identify muon candidates in an event. Run 13 presented a unique challenge to cross section measurements in that the high luminosity of the run enabled a high probability of multiple collisions. This has a non-negligible effect on the cross sections. The Run 13 J/ψ cross section measurement and its challenges are discussed in Chapter 4.

A cross section measurement must be normalized by the integrated luminosity for the entire run period. It must be measured using a technique called the Vernier Scan, detailed in Chapter 5. The technique utilizes the minimum bias detectors at PHENIX as luminosity monitors and measures the proton-proton cross section seen by the minimum bias trigger. This minimum bias cross section is a parameter used in the luminosity calculation.

The inclusive differential J/ψ production cross section is measured for PHENIX forward and backward rapidity at $\sqrt{s} = 510$ GeV as functions of transverse momentum and rapidity. Comparison to the CGC+NRQCD [6] model shows good agreement at low transverse momentum. At higher transverse momentum, NLO+NRQCD predictions [7] underestimate the data.

The 2013 PHENIX dataset has such high luminosity, that it negatively affected the performance of the PHENIX muon arms. The effects of high luminosity on the Muon Tracker (MuTr) hit efficiency are studied in this thesis. These effects have now been quantified in simulations and the 2013 dataset can be used for more muon analyses with reasonable systematic uncertainties.

Chapter 2

Theoretical Motivation

This chapter details what parameters and techniques are necessary for making a theoretical production cross section calculation for the J/ψ meson in proton-proton collisions. Cross section calculations for proton-proton collisions require as input the theoretical framework of particle physics, perturbative calculation techniques, and data from collision and scattering experiments which frame non-perturbative models of hadronization.

In a proton-proton collision that produces a J/ψ meson, see Figure 2.1, two partons inside the proton, each carrying a specific momentum fraction, x_i of the original proton's momentum, p_i, labeled step 1, interact in a hard scattering process, labeled step 2. An outgoing quark then hadronizes into a J/ψ meson, step 3.

In order to calculate the the hard scattering cross section of step 2, it is essential to understand the Standard Model of particle physics, perturbative Quantum Chromodynamics (pQCD), and Feynman diagrams. These topics are discussed in Sections 2.1 through 2.2.3. These sections provide a theoretical basis for experiments and calculations in particle physics.

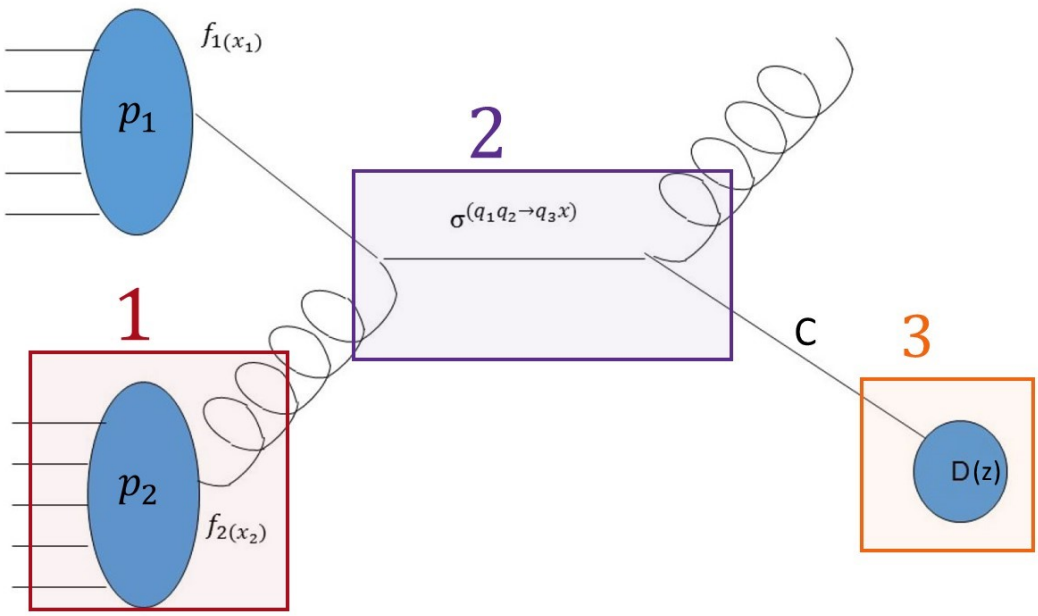

Figure 2.1: A diagram of a proton-proton collision. The total cross section for a process can be factorized in terms of the parton distribution functions (PDFs) ($f_a(x_a, \mu^2)$ of step 1, hard-scattering partonic cross sections ($\hat{\sigma}(q_1q_2 \to q_3X)$) of step two, and fragmentation functions ($D_c^h(z, \mu_f^2)$) of step 3. (Please see text for definitions of these terms)

Steps 1 and 3 are "soft" processes and cannot be calculated through pQCD techniques. They require a phenomenological model and experimental input.

In order to understand collision dynamics in step 1 for protons, a complex, composite particle, the structure of hadrons must be detailed. Section 2.3 discusses hadron structure functions, parton distribution functions (PDFs), and the Deep Inelastic Scattering (DIS) experiments used to measure them. Proton structure functions are related to PDFs, which describe the momentum probability distribution of partons inside the proton, discussed in section 2.3.2.

A final step in a collision is the hadronization of a new particle from the hard scattering of partons in a collision, shown in step 3. This process is described using a

fragmentation function, and presented in Section 2.3.3. In the case of the J/ψ meson, the fragmentation function is not well understood, which motivates the measurement of the J/ψ cross section of this thesis.

A powerful technique for cross section calculations, utilizing all steps in a proton-proton collision, is factorization, considered in Section 2.3.3. Using factorization, PDFs of the interacting partons are convoluted with the hard scattering cross section of the partons and the fragmentation function into the resulting hadron, see Figure 2.1. Using factorization, and phenomenological inputs, a theoretical cross-section can be calculated and compared to experiments. The comparison can lead to better understanding of the theoretical framework in which the calculation was made.

These quantities and techniques are applied to the cross section calculation for the J/ψ meson for proton-proton collisions at $\sqrt{s} = 510$GeV in section 2.4. These calculations are carried out for three different production mechanisms of the J/ψ meson.

2.1 The Standard Model

The Standard Model of particle physics is a theoretical framework of fundamental particles; spin-1/2 fermions, and their interactions propagated through integer spin gauge bosons. The theory is based upon fundamental symmetries and is formulated as non-Abelian group SU(3)$\otimes$SU(2)$\otimes$U(1). Strong interactions of Quantum Chromodynamics (QCD) are described by group SU(3), weak interactions by SU(2), and electromagnetic interactions of Quantum Electrodynamics (QED) by U(1). The beauty of the theory is that it is all based upon the requirement of local gauge invariance. Though not quite complete, to this date, the Standard Model has withstood every experimental test, and made some of the most accurate predictions in all of

physics.

The fermions contained within the Standard Model are the quarks and leptons. All of these particles have their own antiparticle. There are three generations of all quarks and leptons. The first generation of quarks contains the up and down quarks, the lightest and most abundant quarks. A hadron is a bound state of quarks held together by gluons, the propagators of the strong nuclear force. Hadrons consist of two particle types, baryons and mesons. A baryon is a bound state of three valence quarks; a meson is a bound state of a quark-antiquark pair, each held together in a gluon field. The most familiar hadrons are the baryons, the proton and neutron, and are made up of up and down quarks. The next generation of quarks includes the charm and strange quarks, heavier than the up and down quarks, and are mainly produced in collider experiments. The third generation, top, and bottom, is even higher in mass and requires high energy particle collisions for production. Quarks make up all forms of stable matter. Regarding the leptons, there are the massive and electrically charged electron, muon and tau particles, each with their own neutrino. Neutrinos are nearly massless, and neutral in charge. In the following chapters, the charm and the anti-charm quarks, and the positive and negative muons are examined through proton collisions at the Relativistic Heavy Ion Collider.

The integer spin bosons are the photon, gluon, and $W^{\pm}$ and Z^0. Electromagnetic interactions are propagated by a photon from gauge group U(1). The number of gauge bosons of the gauge group SU(N) corresponds to the dimensions, or generators, $N^2 - 1$ of the group[8]. Weak particle interactions and decays of group SU(2), are mediated by the three weak bosons, $W^{\pm}$ and Z^0. Strong nuclear interactions of group SU(3) are carried out by eight flavors of massless gluons. These flavors are based upon a unique property of quarks and gluons, called color charge. Gluons, with quarks, make up the constituents of hadrons, collectively referred to as partons. Gravitons, theorized propagators of the gravitational force, have not yet been discovered. The

spin-0 Higgs boson propagates the Higgs field, which is responsible for the mass of the fundamental particles.

These fundamental particles, and their interactions with bosons from the four fundamental forces in nature create the universe as we have observed it. For more information on the Standard Model, the Review of Particle Physics provides a comprehensive resource[9].

2.2 Quantum Chromodynamics

In 1964, Gell-Mann[10] and Zweig[11] independently proposed the quark model from SU(3) group symmetries. This thesis concerns the group SU(3) strong flavor interactions of QCD mediated by gluon exchanges.

2.2.1 Color

In QED there are defined observable electrical charges, positive, negative and neutral. In QCD the electrically charged quarks have an analog to the QED charges called "color" charges. The QCD color charges are labeled "red," "blue," and "green," with each color having an anti-color. Observable hadrons are in "colorless" states. A colorless state is a combination of blue, red, and green; anti-red, anti-blue, and anti-green; or a color and its anti-color, such as, red and anti-red. Quarks have a single color. Gluons are bi-colored; they carry one color and one anti-color. The eight gluon flavors are:

$$g_i = \lambda_i \begin{pmatrix} r\bar{r} & r\bar{b} & r\bar{g} \\ b\bar{r} & b\bar{b} & b\bar{g} \\ g\bar{r} & g\bar{b} & g\bar{g} \end{pmatrix} \tag{2.1}$$

where i =1,2,...8, and the λ_i represent the Gell-Mann matrices that generate SU(3) symmetries. Confinement, discussed in the next section, requires that all naturally

observable particles exist in a color singlet state. For mesons, the state is

$$\frac{1}{\sqrt{3}}(r\bar{r} + b\bar{b} + g\bar{g}). \tag{2.2}$$

Baryon singlet states have a similar combination of rbg. In consequence, gluons cannot exist as free particles[12]. Due to the gluons carrying their own color, they can couple directly to one another, which leads to confinement of quarks and asymptotic freedom.

2.2.2 Asymptotic Freedom and Perturbative QCD

In 1973, David Gross and Frank Wilczek[13], and David Politzer[14] theorized a property of quarks and gluons called asymptotic freedom. Asymptotic freedom describes how the force between the quarks in a bound state increases as the distance between the quarks increases, and the force between the two quarks decreases as the quarks move closer together.

The renormalized QCD strong coupling constant,

$$\alpha_s(Q^2) = \frac{\alpha_s(\mu^2)}{1 + \frac{\alpha_s(\mu^2)}{12\pi}(11N - 2f)\ln(Q^2/\mu^2)} \tag{2.3}$$

describes the strength of the strong interaction mediated by virtual gluons of mass μ with momentum transfer Q^2. The mass of the virtual gluon sets the reference value, or energy scale of the strong interaction as $\alpha_s(Q^2 = \mu^2)$[15]. For group SU(3), $N = 3$, and f is the number of flavors in the interaction.

By introducing

$$\Lambda^2 = \mu^2 \exp\left[\frac{-12\pi}{(33 - 2f)\alpha_s(\mu^2)}\right] \tag{2.4}$$

equation 2.3 can be written as

$$\alpha_s(Q^2) = \frac{12\pi}{(33 - 2f)\ln(Q^2/\Lambda^2)} \tag{2.5}$$

where $\alpha_s(Q^2)$ depends on only one parameter. As momentum transfer increases, the effective coupling constant decreases logarithmically, which implies that at very short distance scales, quarks are essentially free. This defines the running strong coupling. As Q^2 becomes much larger than Λ^2, the strong coupling is small and perturbative calculations of interacting quarks and gluons are valid. The experimentally determined $\Lambda_{QCD} = 0.2 \pm 0.1 \text{GeV/c}$[16] can be considered to mark the boundary between quasi-free quarks and gluons, and that of hadrons[17]. In deep inelastic scattering (DIS), discussed in Section 2.3.2, where Q^2 is large, DIS can provide justification for the quark-parton model predictions in QCD[15]. In high energy hadron collisions, the momentum transfer is great enough for perturbative approximations in calculations to be quite precise[18].

2.2.3 Confinement

As a consequence of asymptotic freedom, the strength of the coupling increases as distance increases. This implies that quarks are confined to hadrons as bound states by gluons. Quarks have yet to be observed unbound. As a consequence, in particle collisions, where quarks and gluons interact at high energies, quarks will pull quark-anti-quark pairs out of the vacuum to form bound, colorless states, thus remaining confined.

2.3 Hadron Structure

The model for hadron structure has evolved considerably over the past century. J.J. Thomson's "plum pudding" atomic model [19] was quickly disproved by Rutherford's scattering experiment which showed that the atom is mostly empty space, with a dense, positively charged, nucleus containing most of the atomic mass at the

center[20]. This led to the discovery of the proton. Increasingly modern probing techniques have yielded further insight into the structure of hadrons.

The simplest nucleus to study for hadron collisions is the proton. The proton is a baryon with three valence quarks, uud, held together by gluons with a sea of quark-anti-quark pairs. It has charge +1, spin-1/2, and mass of 938.27 MeV/c^2. The proton has a lifetime of at least 10^{34} years. The principle of conservation of baryon number accounts for this stability, since the proton is the lightest baryon. This conservation law requires the number of baryons in the universe to be constant, and even though Grand Unified Theories (GUTs) allow for minute violation in baryon number [21], free proton decay has not yet been observed.

2.3.1 Cross Sections in Experiments

A cross section measurement, in terms of experimental particle physics, is essentially a measure of the probability of going from an initial state, to a final state, detected within a certain kinematic region. Cross section measurements can help to refine theoretical models for hadronization and production mechanisms. It is necessary to accurately model the structure of the proton for theoretical cross section calculations to be compared to experimental cross section measurements. Cross sections are of the form

$$\sigma = \int d\Omega \frac{d\sigma}{d\Omega} \tag{2.6}$$

where $d\Omega$ is the solid angle, and $\frac{d\sigma}{d\Omega}$ is the differential cross section with respect to the solid angle, or volume in which the particles interact.

It is sometimes useful to represent a partonic cross section as a differential cross section. The differential cross section can be taken for any kinematic variable, but

the most useful are energy, E, and three-momentum, p [22] and can be written as

$$E\frac{d^3\sigma}{dp^3} = \frac{1}{2\pi p_T}\frac{d^2\sigma}{dp_z dp_T} \tag{2.7}$$

Typical kinematic variables used in equation 2.7 are rapidity (y) for the longitudinal momentum, p_z, and the transverse momentum of the particle (p_T). Rapidity is defined as

$$y = \frac{1}{2}\ln\frac{E + p_z c}{E - p_z c} \tag{2.8}$$

where p_z is the particle's momentum along the beam axis [23], and is a relativistic approximation of pseudorapidity, defined as

$$\eta = -\ln\left[\tan\left(\frac{\theta}{2}\right)\right] \tag{2.9}$$

where θ is the angle the particle's trajectory makes with the beam axis.

For cross section measurements in collider experiments, the cross section is dependent on the number of events, N. The cross section is normalized by the beam luminosity, L, as

$$\sigma(pp \to X) = \frac{N}{L}. \tag{2.10}$$

The number of desired events is dependent on detector geometry, the efficiencies of the detector event triggers, and the efficiency of the particle track reconstruction algorithm. Luminosity and event yield calculations are explored further in chapters 4 and 5.

2.3.2 Deep Inelastic Scattering and Structure Functions

Since quarks cannot be observed freely outside of hadrons due to confinement, scientists must observe their interactions through the scattering of hadrons. One technique

for probing inside the proton to examine its structure is deep inelastic scattering (DIS). This technique scatters beams of leptons on protons at varying energies to observe the structure of the proton at different energy, and therefore distance scales. The concept of DIS is similar to that of Rutherford's gold foil experiment. DIS experiments explore the electroweak interactions, since the leptons carry no color charge, while proton-proton collisions can probe the strong interactions.

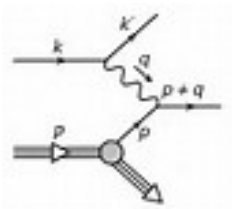

Figure 2.2: Typical deep inelastic scattering Feynman diagram with kinematic variables.

In DIS, the four-momentum of the incoming lepton ($\mathbf{k}$) on the proton target is known, and is compared to the outgoing four-momentum of the lepton ($\mathbf{k'}$), which is detected, see Figure 2.2. The difference in four-momentum ($\mathbf{q} = \mathbf{k'} - \mathbf{k}$) yields the energy transfer $Q^2 = -q^2$ of the photon, or Z boson, between the lepton and a quark from the proton. The proton's initial four-momentum is denoted as $\mathbf{p}$. Other pertinent kinematic variables are:

$$x = \frac{Q^2}{2\mathbf{p}\cdot\mathbf{q}} = \frac{Q^2}{2M\nu} \qquad\qquad \nu = \frac{\mathbf{p}\cdot\mathbf{q}}{M} \tag{2.11}$$

where x, or Bjorken(x_{Bj}), is the fraction of a proton's momentum carried by a quark. Semi-Inclusive Deep Inelastic Scattering (SIDIS) involves a similar experimental procedure to DIS, but in addition, the produced hadrons are detected.

The differential cross section for DIS is approximated by

$$d\sigma \sim L^e_{\mu\nu} W^{\mu\nu} \tag{2.12}$$

where $L^e_{\mu\nu}$ is the lepton tensor which is written as

$$L^{\mu\nu} = \frac{1}{2}\mathrm{Tr}((\not{k}' + m)\gamma^\mu(\not{k} + m)\gamma^\nu). \tag{2.13}$$

This considers the summation of electron spins, and the hadronic tensor $W^{\mu\nu}$ serves to parameterize the ignorance of the form of the hadronic current at the other end of the propagator. As the cross section is already summed and averaged over spins, the full form of $W^{\mu\nu}$, for $ep \to eX$ where the proton breaks up into N particles in the final hadronic state, can be formally written as

$$\begin{aligned} W_{\mu\nu} =& \frac{1}{4\pi M}\sum_N \left(\frac{1}{2}\sum_s\right)\int\prod_{n=1}^{N}\left(\frac{d^3p'_n}{2E'_n(2\pi)^3}\right)\sum_{s_n}\langle p,s|\tilde{J^\dagger_\mu}|X\rangle \\ & \times\langle X|\tilde{J}_\nu|p,s\rangle(2\pi)^4\delta^4(p+q-\sum_n p'_n). \end{aligned} \tag{2.14}$$

The differential cross section is then approximated to

$$(L^e)^{\mu\nu}W_{\mu\nu} = 4EE'\left\{\cos^2\frac{\theta}{2}W_2(\nu,q^2) + \sin^2\frac{\theta}{2}2W_1(\nu,q^2)\right\} \tag{2.15}$$

where $v = k/E$, and θ is the angle through which the electron is scattered.

Including the flux factor and the phase space factor for the outgoing electron, the inclusive differential cross section in the laboratory frame becomes [17]

$$\left.\frac{d\sigma}{dE'd\Omega}\right|_{lab} = \frac{\alpha^2}{4e^2\sin^4\frac{\theta}{2}}\left\{W_2(\nu,q^2)\cos^2\frac{\theta}{2} + 2W_1(\nu,q^2)\sin^2\frac{\theta}{2}\right\}. \tag{2.16}$$

At very high energy scattering, $Q^2 \to \infty$, the $W_i(x,Q^2)$ factors can be related to the unpolarized proton structure functions, $F_1(x)$ and $F_2(x)$, as $\nu W_2(x,Q^2) = F_2(x)$ and $MW_1(x,Q^2) = F_1(x)$, with $2xF_1(x) = F_2(x)$ (the Callan Gross Sum Rule)[26, 27, 28], which is a consequence of the spin$-\frac{1}{2}$ nature of the quarks. The relationship between the W_i and F_i at high energy is called the "scaling" of the structure functions with respect to x_{Bj}. Just as measurements of inelastic form factors yield information of the size of the proton, the measurements of the inelastic structure functions at large

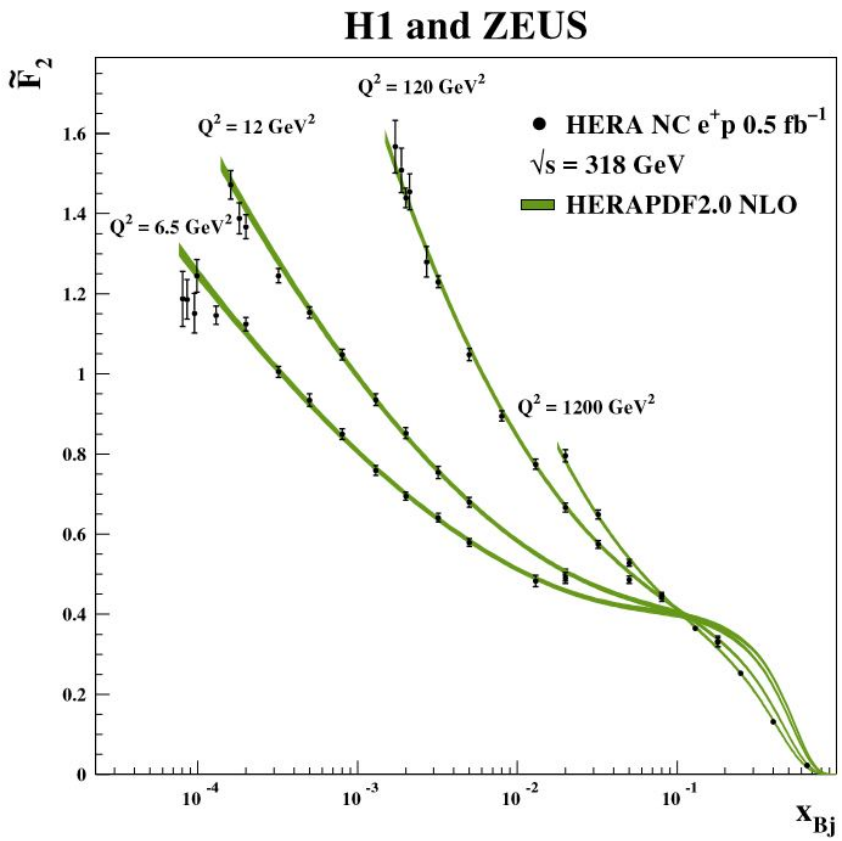

Figure 2.3: The proton structure functions as extracted from the HERA combined reduced neutral current cross sections for four values of Q^2 together with predictions using HERAPDF2.0 NLO. The measurement was completed by the ZEUS and H1 collaborations[24, 25].

Q^2 reveal the quark structure of the proton in combination with Bjorken scaling[17]. As a result of this, the structure function $F_1(x)$ can be expressed as

$$F_1(x) = \frac{1}{2}\sum_m \left[\frac{4}{9}(u_m(x) + \bar{u}_m(x)) + \frac{1}{9}(d_m(x) + \bar{d}_m(x)) + \frac{1}{9}(s_m(x) + \bar{s}_m(x))\right] \quad (2.17)$$

in terms of parton distribution functions, which means that the structure functions directly determine the parton distribution functions. A parton distribution function gives the probability of finding an up-type (u_m, $\bar{u}_m$), down-type (d_m, $\bar{d}_m$), or strange-type (s_m, $\bar{s}_m$) parton (or anti-parton) of generation m with momentum fraction x

inside the proton probed with momentum transfer Q^2. The gluon PDFs (g) account for most of the particles, and about half of the momentum, of the proton and are determined by hadron-hadron collisions[29, 30, 31, 32].

In the 1960s, the pioneering deep inelastic scattering experiments performed by J. Friedman, H. Kendall, and R. Taylor[33, 34, 35] gave evidence for the point-like constituents of the proton, and thus quarks, giving life to the parton model. Since these early days, DIS experiments from SLAC[36], the LHC[37] and HERA[24] have provided numerous measurements of parton distribution functions, see Figure 2.4, the proton structure functions, see Figure 2.3, and the total DIS cross sections, see Figure 2.5.

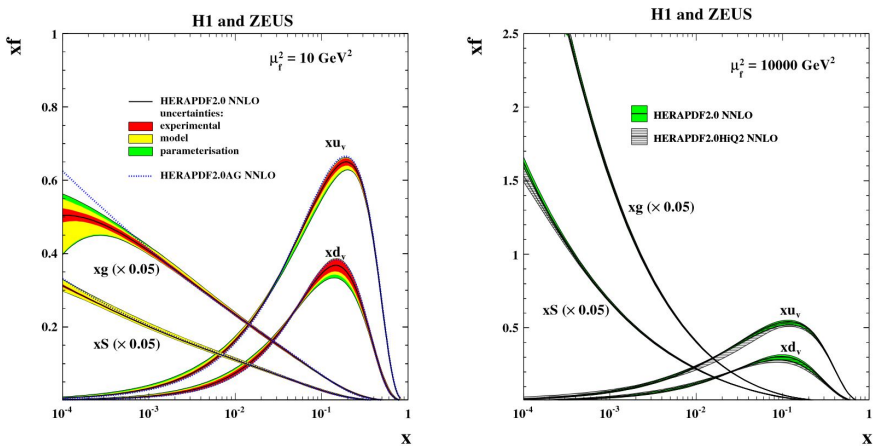

Figure 2.4: The parton distribution functions multiplied by Bjorken$-x$. The gluon and sea distributions are scaled down by a factor of 20. The NNLO distributions at $\mu^2 = 10\text{GeV}^2$ (left) and the NNLO distributions at $\mu^2 = 10000\text{GeV}^2$ (right) were measured at HERA by the ZEUS and H1 collaborations[24][25].

2.3.3 Fragmentation Functions and Factorization

Deep inelastic scattering is followed by the process of hadronization. The quark escapes from the parent hadron into another newly created, faster hadron. In proton-

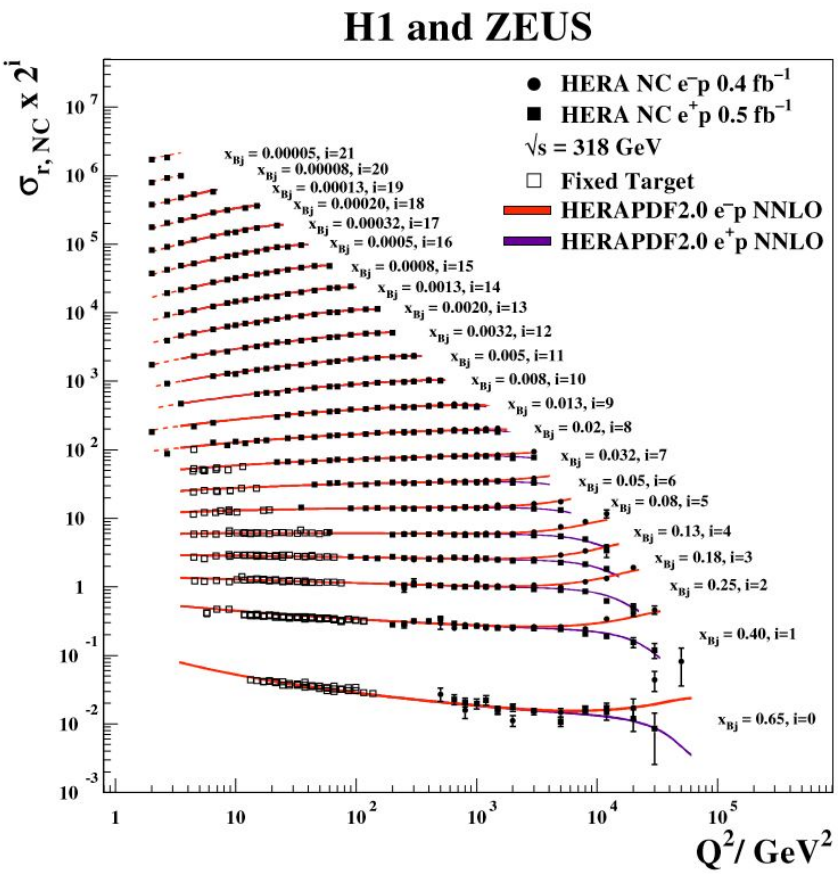

Figure 2.5: The combined HERA data for the inclusive neutral current e^+p and e^-p cross sections as measured at HERA by the ZEUS and H1 collaborations[24, 25].

proton collisions, after a parton, c, has been ejected of the proton, the conversion of the high momentum parton into a hadron, C, is assumed to be independent of how the parton was produced[22].

The soft process of hadronization, step 3 in Figure 2.1, is described by the fragmentation function, which must be measured by conducting e^+e^- collision experiments and examining the production of charmed mesons. Fragmentation functions of the form $D_c^C(z)$ describe the conversion of a specific parton into a certain hadron, where z in the fragmentation function is the fraction of quark momentum carried off

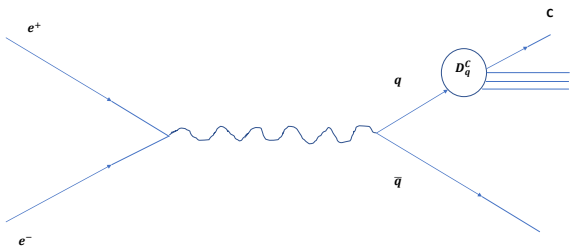

Figure 2.6: Determination of the fragmentation function $D_q^C(z)$, from $e^+e^- \to CX$. Hadron C has fraction z of the quark's momentum[22].

by the hadron and given by $z \equiv p_C/q_q \simeq p_C/E$, and E gives the electron's center of mass energy, since the $q\bar{q}$ pair must initially carry the full e^+e^- energy, see Figure 2.6. In the parton model, the e^+e^- collision cross section is given by [22]

$$\frac{d\sigma}{dz}(e^+e^- \to CX) = \sum_q \sigma(e^+e^- \to q\bar{q}) \left[D_q^C(z) + D_{\bar{q}}^C(z)\right] \tag{2.18}$$

$$= \left(\frac{4\pi\alpha^2}{3s}\right) 3 \sum_q e_q^2 [D_q^C(z) + D_{\bar{q}}^C(z)]. \tag{2.19}$$

During $p+p$ collisions, there are both hard (short time scale) and soft (long time scale) processes that occur. The hard processes are the partonic interactions σ, see Figure 2.1, and are calculable in the regime of perturbative QCD (pQCD). The soft processes must be measured experimentally and these include the parton distribution functions $f_{1,2}(x_{1,2}, \mu^2)$, where μ is an energy scale usually chosen to be Q^2, and the fragmentation function $D_c^h(z, \mu_f^2)$, where μ_f is an energy scale for the final state hadron. One assumption made is that the initial and final state parton distribution functions and fragmentation functions are process independent, or universal. This means that they can therefore be used in calculations of processes other than those from which they were derived. The second assumption is the collinear framework

of pQCD. The collinear framework assumes that the partons inside the hadrons do not have any transverse momentum with respect to the momentum of the original hadron. This also applies to the final state hadron. It is with universality and the collinear framework of perturbative QCD that the high momentum transfer p-p cross section can be factorized as a convolution of the parton distribution functions, fragmentation functions and the partonic cross section[38, 39] as

$$\sigma(pp \to hx) = \sum_{1,2,c} f_1(x_1, \mu^2) \otimes f_2(x_2, \mu^2) \otimes \hat{\sigma}(q_1 q_2 \to q_3 X) \otimes D_3^h(z, \mu_f^2). \quad (2.20)$$

Fragmentation of the J/ψ is not well understood,. Three theoretical models for production mechanisms of the J/ψ are presented in the next section. Theoretical models, with complimentary measurements, help clarify the process of J/ψ production.

2.4 The J/ψ Meson

Charmonium refers to a bound state of a charm and an anti-charm quark. The J/ψ meson is the most abundantly produced charmonium state with $n^{2S+1}L_J = 1^3S_1$ and $J^{PC} = 1^{--}$. The J/ψ was discovered independently and simultaneously in 1974 at Brookhaven National Laboratory by Samuel Ting of MIT[40, 41], and at the Stanford Linear Accelerator (SLAC) by Burton Richter[42] and was the first charmonium state to be observed. Ting had given the newly discovered particle the name "J," while Richter named it the "ψ". They realized they found the same particle and both announced their discoveries on November 11, 1974. A composite name of J/ψ was used for further publications. Ting and Richter were awarded the Nobel Prize in Physics in 1976 for their discovery[43].

The J/ψ meson has a mass of 3.0969 GeV/c^2, with a peak width of only 92.9 keV. A state decaying predominantly to hadrons via strong interactions would have

an expected width measured in MeV. Even though the J/ψ has no open charm, the narrow width of the peak leaves no other explanation for the composition of the J/ψ in terms of u, d, or s flavor quarks, so the J/ψ must be a charmonium state[16]. The narrow width of the J/ψ peak is attributed to the OZI rule[44], discussed in the next section, and the fact that the $m_{J/\psi} < 2m_D$, where D is the lightest charmed meson. The J/ψ is therefore kinematically forbidden from decaying into D mesons. The OZI rule suppresses strong decay modes of the J/ψ meson, resulting in an increased lifetime, but requires annihilation of the $c\bar{c}$ pair for hadronic decays, resulting in a narrow peak[17, 12]. The J/ψ primarily decays into hadrons (Branching ratio $B_{hadrons} = 87.7 \pm 0.5\%$), but also decays into charged leptons ($B_{e^+e^-} = 5.971 \pm 0.032\%$ and $B_{\mu^+\mu^-} = 5.961 \pm 0.033\%$)[45], which are easier to detect in experiments, as leptons are not subject to strong interactions while passing through detector materials, making their momentum reconstruction simpler. Muon detection capitalizes on muons' unique penetrating power in matter[16]. The dimuon decay channel is examined in this thesis for the cross section measurement. In collider experiments, observed J/ψ's are not always directly produced. According to studies of heavy quarkonium production cross sections at RHIC energies using the Color Singlet Model (CSM), indirect production of J/ψ's, feed-down from the χ_c, accounts for $30 \pm 10\%$ of the total J/ψ yield, while direct production accounts for $59 \pm 12\%$ of the J/ψ yield[46].

2.4.1 The OZI Rule

The OZI Rule was developed independently by S. Okubo[47, 44], G. Zweig[48] and J. Iizuka[49] in the 1960s. In a Feynman diagram for strong interactions, if the gluon lines are removed and the initial and final state particles can be separated into two distinct diagrams, with one diagram representing the initial state, and one representing the final state, then the OZI rule asserts that process is suppressed,

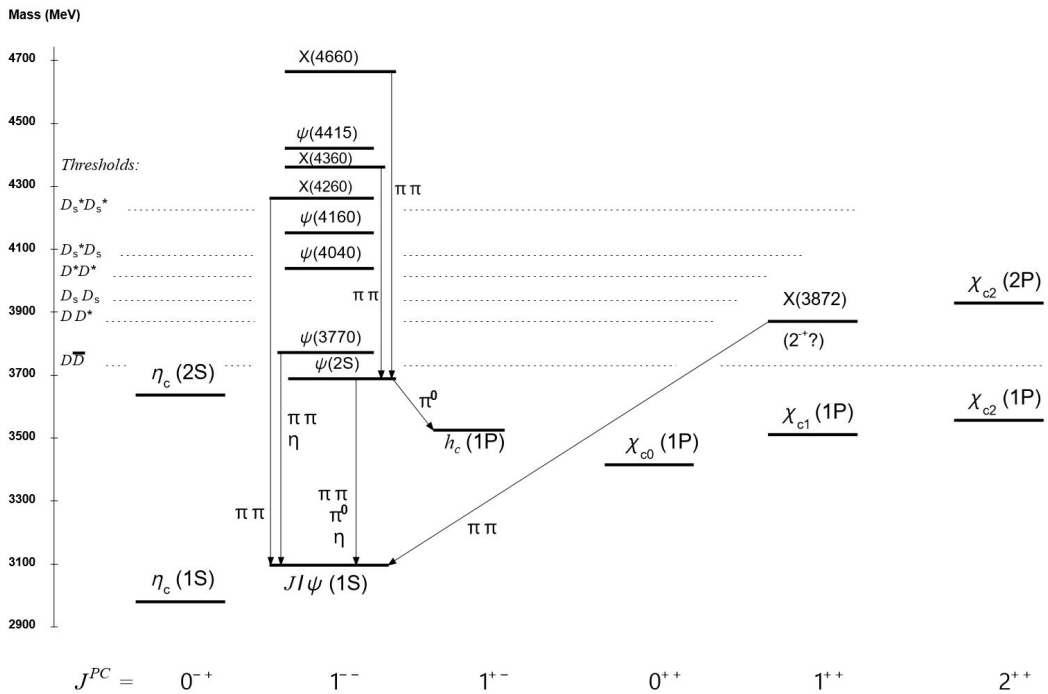

Figure 2.7: The charmonium system from [45]. In addition to direct production, the J/ψ can be produced from decays from higher order charmonium (and beauty) states.

see Figure 2.8. The decay of the J/ψ into a pair of charmed mesons is forbidden by energy conservation ($M_{J/\psi} < 2M_D$), where $M_D = D(1870)$ is the mass of the lightest charmed meson. The charm threshold is considered to be $2M_D$ and therefore the only hadronic decays allowed are by similar mechanisms in Figure 2.8, where initial and final quark lines are disconnected and the gluons are high energy gluons[16]. The reason for this in QCD is that since both the decaying particle and the three pions in the final state are color singlets, they can only be connected by the exchange of a combination of gluons that is also in a color singlet, meaning not one, but three gluons. Moreover, the J/ψ has charge conjugation $C = -1$ due to its production in e^+e^- annihilation via photon exchange, requiring a minimum exchange of three gluons[16].

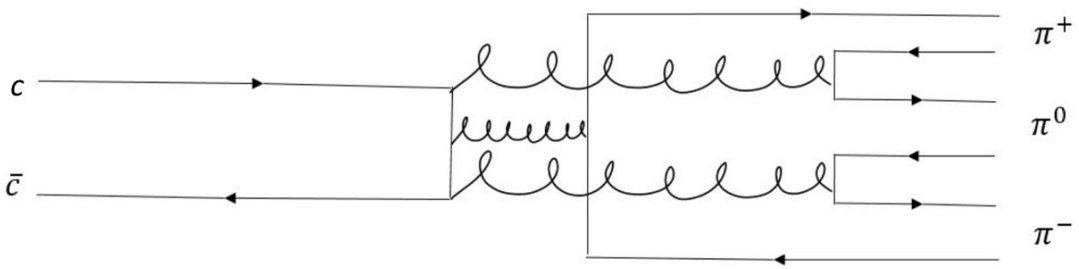

Figure 2.8: Charmonium state to an OZI suppressed decay into pions below the $D\bar{D}$ threshold.

2.4.2 Production Mechanisms

Several theoretical models of J/ψ production mechanisms have been created and compared to previous J/ψ cross section measurements and experimental data. These models include the Color Singlet Model (CSM)[50, 51], Color Evaporation Model (CEM)[52, 53], and non-relativistic QCD(NRQCD)[54]. Feed-down from higher mass charmonium states is not discussed here. The cross section measured in this thesis will also be compared to predictions from these models. Several examples of Feynman diagrams of J/ψ production at RHIC energies can be seen in Figure 2.9.

Non-Relativistic QCD

Non-Relativistic QCD (NRQCD)[54], also called the Color Octet Model (COM), is an effective field theory where the c and $\bar{c}$ quarks are assumed to have a small $v << c$ in

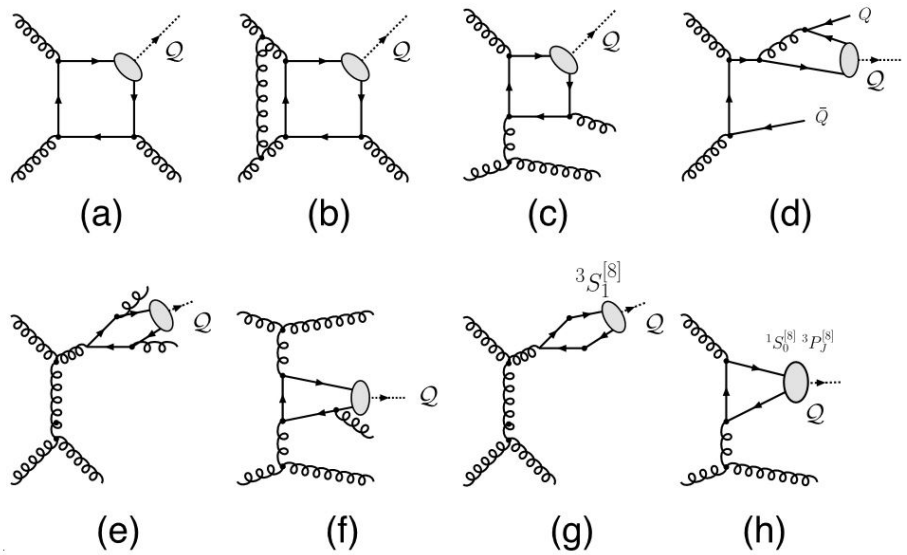

Figure 2.9: Representative Feynman diagrams of interactions that contribute to the hadroproduction of ${}^3S_1$ quarkonium states via color-singlet channels at orders α_s^3 (a), α_s^4 (b,c,d), and α_s^5 (e,f), and via color-octet channels at order α_s^3 (g,h)[55].

the $c\bar{c}$ rest frame, and thus treated non-relativistically. In this model, both the color singlet and color octet states are included, see section 2.2.1[55]. NRQCD assumes the universality of the matrix elements so they can be factorized, and thus the total production amplitude is a double expansion in terms of v and the strong coupling α_s and written as

$$d\sigma[J/\psi] = \sum_i d\sigma[c\bar{c}(n)]\langle O_n^{J/\psi}\rangle$$

where n are the color, spin, and angular momentum states of the $c\bar{c}$ pair, $d\sigma[c\bar{c}(n)]$ is the production cross section of the $c\bar{c}$ pair in state n, and the $\langle O_n^{J/\psi}\rangle$ are the NRQCD matrix elements for the transition probability from the $c\bar{c}$ pair in state n to a J/ψ meson. NRQCD is able to replicate the charmonium cross section data, but fails upon comparison to other parameters such as the angular decay coefficients[56].

Color Singlet Model

In the Color Singlet Model (CSM)[50, 51], it is assumed that the $c\bar{c}$ pair that evolves into the charmonium is in a color singlet state, and the produced J/ψ is in the same quantum state as the $c\bar{c}$ pair. It is also assumed that the charmonium pair creation and the J/ψ hadronization can be factorized. The cross section is then written as

$$d\sigma[J/\psi] = \int_0^{\inf} dm \frac{d\sigma_{c\bar{c}}[^3S_1]}{dm} \psi_{J/\psi}(r=0),$$

where $\psi_{J/\psi}(r=0)$ is the non-relativistic J/ψ wavefunction evaluated at the origin.

The CSM accurately predicts the charmonium polarization, but the leading order (LO) term underpredicts the experimental cross section by a factor of ~ 50 at 1.8 TeV[57, 58]. At high energies, the next-to-leading order (NLO) and next-to-next-to-leading order (NNLO) corrections in α_s are quite large and may compromise the convergence of the CSM.

Color Evaporation Model

In the Color Evaporation Model (CEM)[52, 53], it is assumed that every produced $q\bar{q}$ pair evolves into a quarkonium state if it has an invariant mass that is less than the threshold for producing a pair of open-flavor heavy mesons, $2m_D$, but larger than that of two charm quarks. An assumption in the model is that the color state of the produced $c\bar{c}$ is random, with there being a probability of 1/9 for the state to be a color singlet state. The cross section is then written as

$$d\sigma[J/\psi] = \frac{F}{9} \int_{2mc}^{2mD} dm \frac{d\sigma_{c\bar{c}}}{dm}$$

where the nonperturbative probability for the $q\bar{q}$ pair to evolve into a quarkonium state is F, determined by experiments, that is energy and momentum independent, and universal[55]. Charmonium states then become colorless through soft gluon

emission, a non-perturbative phenomenon. The J/ψ cross section is well predicted by the model, see Figure 2.10, for the recent data from PHENIX at 200 GeV[4], but does not have the power to make predictions about charmonium polarization.

2.4.3 Previous Cross Section Measurements

The J/ψ production cross section has been extensively measured at RHIC at $\sqrt{s} =$ 200 GeV for various beam species. The most recent cross section measurement[4] for $p+p$ collisions, seen in Figures 2.10 and 2.11, have yielded a total J/ψ cross section of $180 \pm 2.0_{stat} \pm 11_{syst}$nb. Run 13 at RHIC has an enormous dataset of 510 GeV $p+p$ collisions, which should provide for an excellent measurement of the J/ψ cross section at that energy.

2.4.4 Predictions

One of the most recent prediction for the differential J/ψ cross sections at 510 GeV is presented by Leonard Kisslinger and Debasish Das[64], see Figure 2.12. The prediction is based upon hybrid meson state theories described in [65], based on the COM and adapted for RHIC energies. Unfortunately, this prediction is only useful for central rapidity ranges and does not cover the kinematic region analyzed in this thesis.

Another prediction is made based upon color glass condensate (CGC) and NRQCD predictions at low transverse momentum[6] and next to leading order NRQCD at high transverse momentum[7]. This prediction is compared to the measured J/ψ production cross section in Chapter 4.

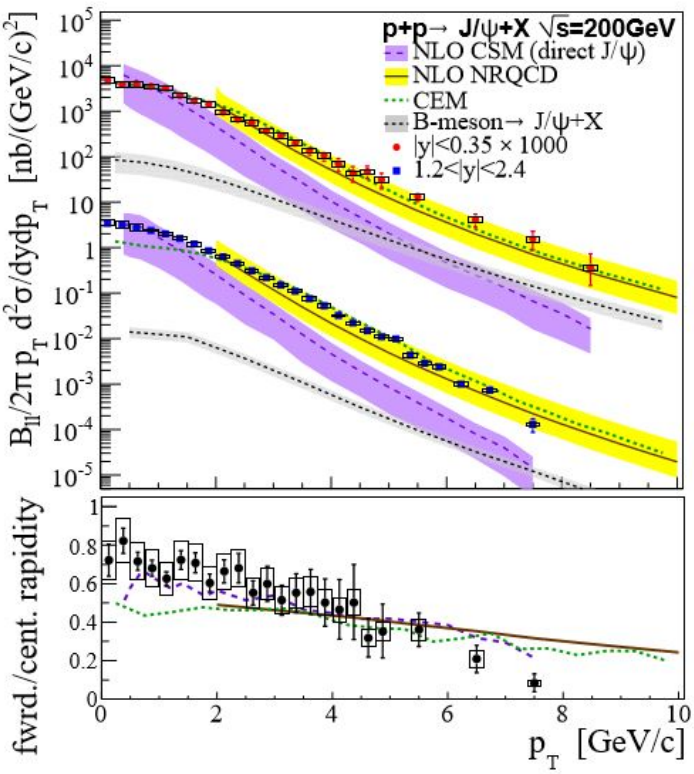

Figure 2.10: The transverse momentum dependent J/ψ yield at 200 GeV as measured at PHENIX at forward and central rapidities [4] in comparison to predictions from the CSM[59], CEM[60], NRQCD[61], and FONLL calculations of B-meson decays[62], which are not discussed in this thesis.

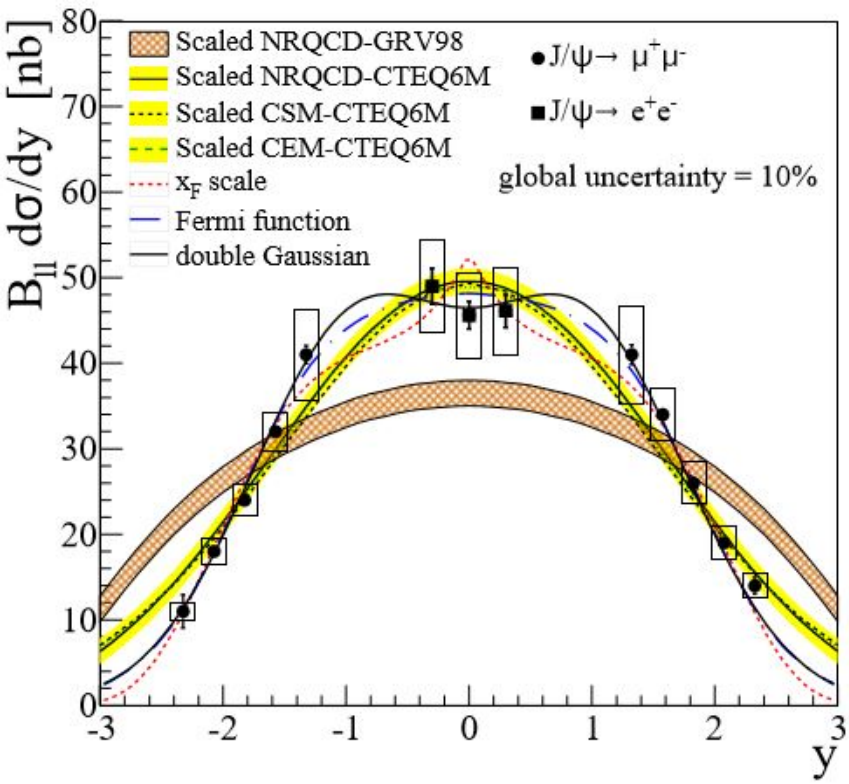

Figure 2.11: Rapidity dependence of the J/ψ differential cross section at central rapidity ($|y| < 0.35$) for the dielectron decay channel; and at forward rapidity $1.2 < |y| < 2.4$ for the dimuon decay channel, along with fits to estimate the total cross section at 200 GeV. The arbitrarily normalized NRQCD[63], CEM[60], and CSM[59] predictions are shown.[4]

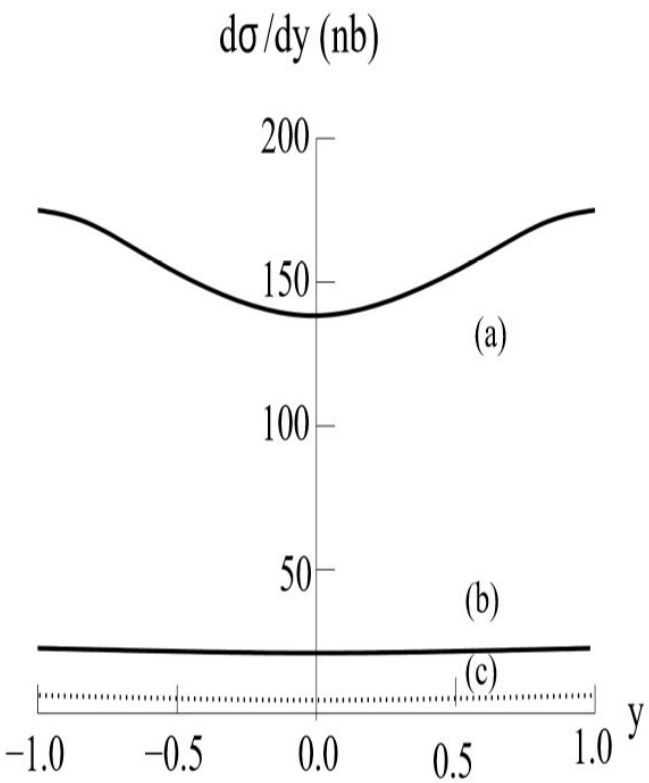

Figure 2.12: The rapidity dependent differential cross section for $\sqrt{s} = 510$ GeV $p-p$ collisions producing (a)J/ψ, (b) ψ(2S) with mixed hybrid theory, and (c) ψ(2S) with standard $c\bar{c}$ model.[64]

Chapter 3

RHIC and PHENIX

3.1 Relativistic Heavy Ion Collider

The Relativistic Heavy Ion Collider (RHIC)[1, 2] began operation in 2000 at Brookhaven National Laboratory, in Upton, New York. At the time, four experiments, at four of the six beam interaction regions, began taking data as well. Two of the experiments, the Broad RAnge Hadron Magnetic Spectrometers Experiment (BRAHMS) and PHOBOS, have since completed data taking and were decommissioned in 2006. Two other larger experiments continued, the Pioneering High Energy Nuclear Interaction eXperiment (PHENIX), decommissioned in 2016 in preparation for an upgrade, and the Solenoidal Tracker At RHIC (STAR). The primary purposes of RHIC are to study the Quark-Gluon Plasma (QGP) and proton spin physics.

The accelerator is capable of colliding various beam species, from polarized protons, to heavy ions resulting in p-Au, p-Al, d-Au, Au-Au, Cu-Au, and U-U. For proton-proton collisions, the ion beams start as individual ion bunches in an optically pumped polarized H^- source and are then accelerated through the Linear

Accelerator (LINAC) to 200 MeV[66], stripped of any remaining electrons, and then transferred to the Booster[67]. Proton bunches are then accelerated through the Booster to energies of 2.3 GeV and then into the Alternate Gradient Synchrotron (AGS) where protons are accelerated further to 24.3 GeV[68]. The protons are subsequently injected into one of two 3.8 km accelerator rings of RHIC and accelerated up to beam energies of 255 GeV[69, 70]. A photograph of the accelerator complex can be seen in Figure 3.1.

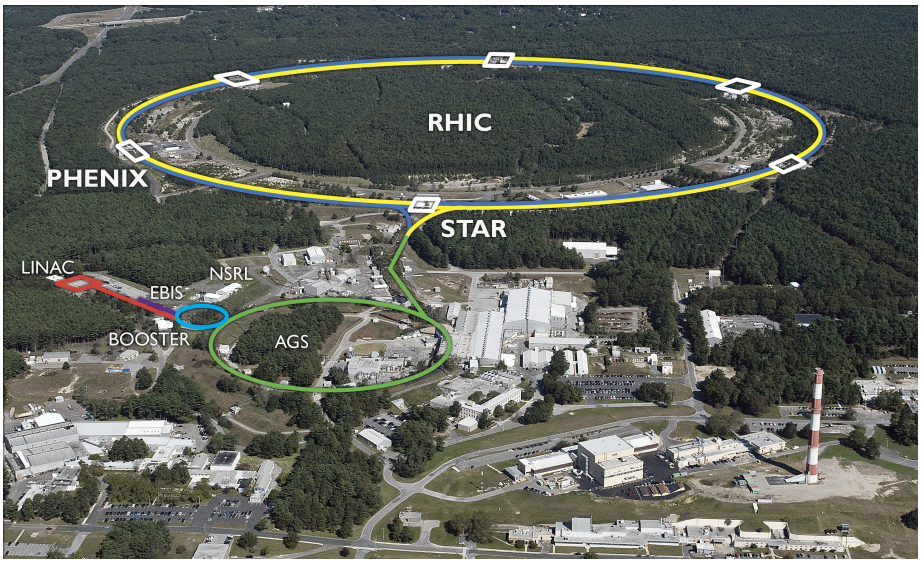

Figure 3.1: RHIC accelerator complex in Upton, NY[1]

Each of the two ion beams consists of up to 120 ion bunches of $\approx 3 \times 10^{11}$ protons with programmed polarization directions. The bunches collide every 106 ns. For the purposes of this analysis, the polarization of the bunches has been integrated over to make this an unpolarized cross-section measurement.

The two beams, labeled blue and yellow, are steered and focused by a system of magnets along the beam pipes. Specialized kicker magnets also dump the beam at the end of a store or when the beam is deemed to be unstable. At each experimental hall, there are four quadrupole magnets that focus the colliding beams to a small

cross-sectional area in an hourglass shape longitudinally to maximize the number of collisions that can take place in a bunch crossing at the nominal interaction point. Additionally, there are DX [71] dipole magnets that steer the beams into collision. This collision point is nominally defined to be $z = 0$, and $\sim 85\%$ of all collisions at PHENIX take place within ± 30 cm of the center of PHENIX.

Along with the complex instrumentation of the accelerator, there are several other detectors that monitor beam position and current including the Wall Current Monitor (WCM) [72], Beam Position Monitors (BPM)[73], and Direct Current Current Transformers (DCCT)[74]. These detectors aid in the Vernier scan analysis for bunch intensity information and monitoring the steps of the Vernier Scan, see Chapter 5.

3.2 PHENIX

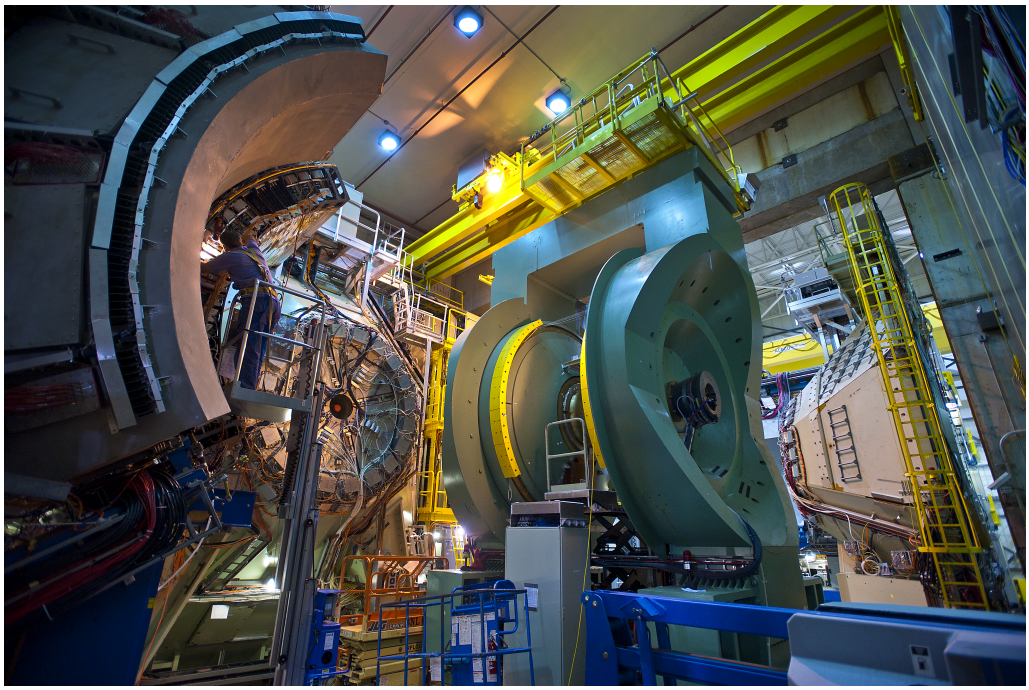

Figure 3.2: PHENIX detector shown in a disassembled condition during maintenance in 2010.

PHENIX [75] is specialized for rare decays, sacrificing geometric acceptance for fast data acquisition and timing, and precision resolution. The experiment consists of four spectrometers around the central interaction point that serve different purposes. A photo of PHENIX, with the East carriage and South Muon Arm displaced from their data taking positions is seen in Figure 3.2. A schematic of the PHENIX detector as configured in Runs 12 and 13 can be seen in Figure 3.3.

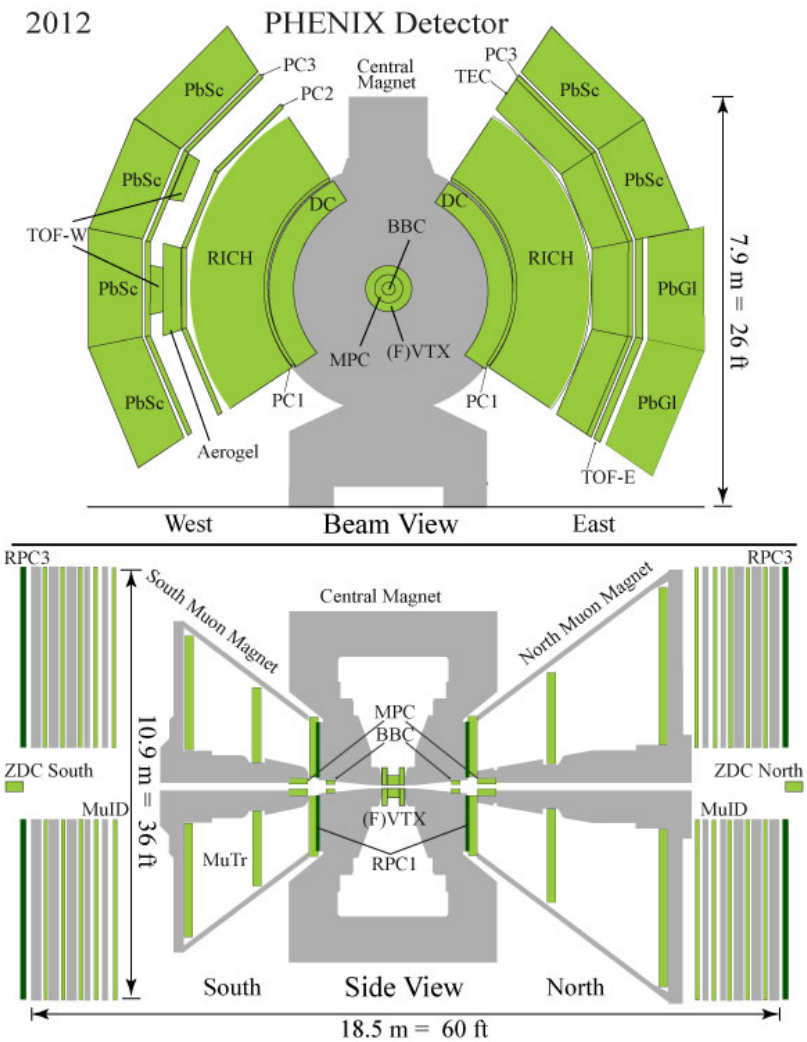

Figure 3.3: PHENIX Central Arm Spectrometers (top) and Muon Arm Spectrometers (bottom) for the 2012 and 2013 run periods.

The global coordinate system defined in PHENIX is a right-handed coordinate system with the beam line along the z-axis, with the North Muon Arm in the positive z-direction. The positive x-axis points to the West Central Arm, and the positive y-direction is therefore defined to be upwards. The polar angle θ is defined as the angle measured counterclockwise from the positive z-axis. The azimuthal angle ϕ is defined by moving counterclockwise from the positive x-axis. The geometric center of the PHENIX detector and the interaction region defines the origin of the coordinate system, see Figure 3.4.

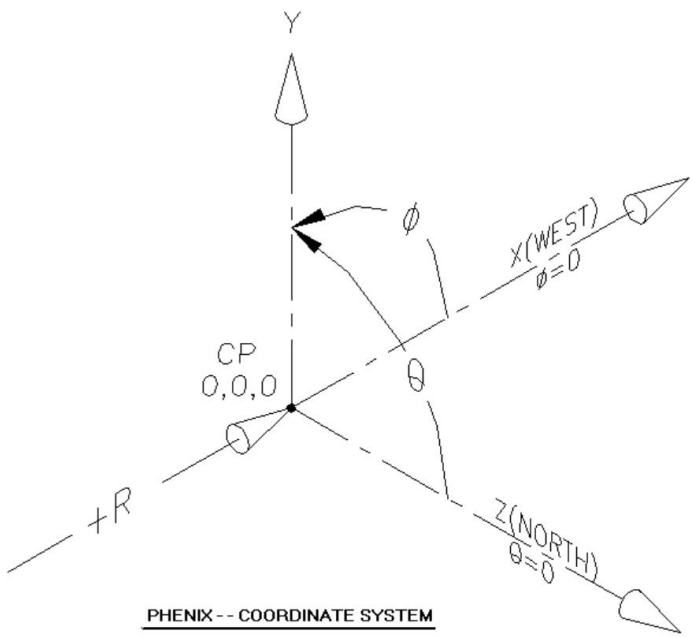

Figure 3.4: PHENIX coordinate system. The beam line is along the z-axis, with the North Arm pointing to the positive z-direction. The West Arm of the Central arm spectrometers points along the positive x-axis. The upward direction defines the positive y-axis.

Figure 3.5: One beam-beam counter (left) comprised of 64 PMTs mounted on quartz crystals (right).

3.2.1 Global Counters

For global event characterization and luminosity counting[76], two detectors along the beam axis are used. They are the Beam-Beam Counters (BBCs) and the Zero Degree Calorimeters (ZDCs). Both detectors are used for fast triggering on events of interest and for the Vernier Scan analysis, used to determine recorded luminosity, as well as physics analyses conducted using the muon arms, and collision geometries.

The BBCs are used to measure event time, vertex positioning, and event-plane characteristics. They are also used as luminosity counters for cross section measurements and relative luminosity counters for asymmetry measurements. Each BBC is constructed of two cylindrical configurations of 64 photomultiplier tubes (PMTs) each with a 3 cm thick quartz radiator mounted onto the photocathode, having an inner radius of 10 cm and an outer radius of 30 cm, see Figure 3.5. Both BBCs are then mounted around the beam pipe at ± 144 cm from the interaction point (IP) of PHENIX. The pseudo-rapidity range of coverage is $3.0 \leq |\eta| \leq 3.9$. The precision timing, with a sensitivity of 52 ± 4 ps, is fast enough to be able to characterize the z vertex within 1.5 cm, but does not measure the transverse distance from the beam axis. This is helpful for analyses which depend on bunch polarization, and the

bunch-by bunch event rate as part of the Vernier Scan analysis. The vertex position is measured by a time-of-flight calculation based on the arrival times of leading charged particles to both BBCs:

$$t_0 = (T_S + T_N)/2 \tag{3.1}$$

$$z_{vtx} = c(T_S - T_N)/2 \tag{3.2}$$

with c being the speed of light, and $T_{N(S)}$ being the average time of arrival of particles measured by the PMTs in one side of the BBC[76]. The BBC is not able to distinguish multiple collisions in the same crossing, so the z-vertex position can be determined improperly, and luminosity can be undercounted. Also, the BBC has a z-vertex dependent trigger efficiency. This will be discussed in Chapter 5.

The ZDC is designed to detect hadrons, such as protons and neutrons with very low transverse momenta. It is used for vertex calculation, timing and event triggering, as well as a local polarimeter, taking advantage of a left-right asymmetry in the production of neutrons in polarized proton collisions [76]. The two identical detectors of the ZDC are placed at $\pm$18m from the IP and outside the DX steering magnets. Charged particles with momenta along the beamline are swept away from the ZDC into the beam lines, leaving only particles created from collisions to be detected by the ZDC. The geometric coverage is a 2mrad cone with pseudo-rapidity range $|\eta| \geq 6$. The ZDC is constructed of alternating layers of tungsten absorbing material to generate the showers, and sampling material, carbon-based optical fiber, to measure the energy from the showers. The timing resolution of the ZDC is approximately 200ps and thus the z-vertex resolution is approximately 30cm. The ZDC records much fewer events and is therefore less likely to undercount events in the presence of multiple collisions. The physical placement of the ZDC in the experimental hall provides for z-vertex detection efficiencies that have a negligible z-vertex dependence. Identical pairs of ZDCs are located at all of the RHIC experiments for a common luminosity measurement.

For any absolute cross section measurement, triggers from the ZDC and BBC are used in coincidence to calculate the z-dependence of triggered events and σ_{BBC}, the luminosity normalization constant, a process described in more detail in Chapter 5.

3.2.2 Magnetic Fields in PHENIX

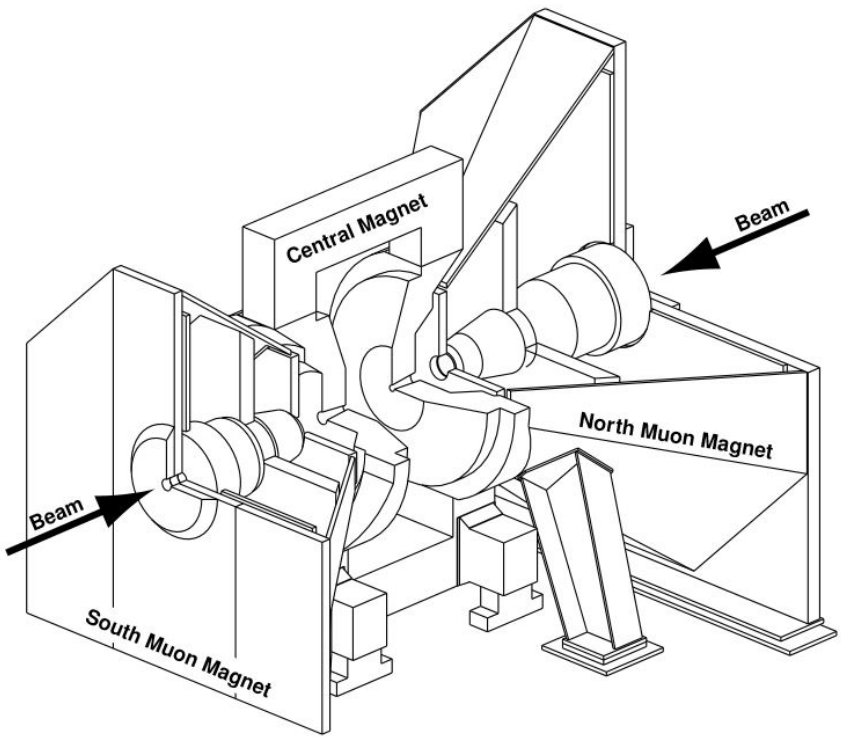

Figure 3.6: Drawing of the PHENIX magnets with a quarter cutout to show the interior structure. Arrows indicate the beam line and direction of colliding beams in RHIC.

An essential part of any collider experiment is momentum tracking of charged particles and this requires large magnetic field volumes. The Central Magnet was designed with the requirements that there be no mass inside the apertures of the poles to minimize interactions and multiple scattering, as well as dense material in the apertures of the North and South Muon Spectrometers to serve as hadron absorbers. The Cen-

tral magnet poles tips comprise 60 cm of low-carbon steel and 20 cm of brass. The yoke of the Central Magnet was formed from low-carbon steel forgings and hot rolled plate. The outer coils for the Central Magnet are each comprised of 6 bifilar wound double pancakes, coils that contain two parallel wound coils, made with 20.3 mm x 20.3 mm copper conductor insulated with fiberglass reinforced epoxy. The outer coils consist of two assemblies each having 144 turns [77]. The Central Magnet has an integrated field that can range from 0.43 T·m to 1.15 T·m with an average of 0.78 T·m at $\theta = 90°$. Current in the coils can be run in the opposite direction to change the field orientation, see Figure 3.7.

Throughout the central region, in between the Drift Chambers and the beam pipe (Figure 3.3), there is an axial magnetic field provided by the Central Magnet. The magnetic field lines are illustrated in Figure 3.7.

The Muon Magnets were designed to have a wide acceptance to maximize the acceptance for muon pair events with full azimuthal coverage and minimum polar angle as close as possible to the beam direction. Additionally, there must be a reasonably uniform magnetic field that does not significantly affect the circulating beams of RHIC. The Muon Magnets are each comprised of a central iron piston that is surrounded at its base with a coil and defines the minimum polar angle of the spectrometer. The rest of the iron yoke consists of an 8-sided lampshade, which defines the maximum polar angle and a back plate that connects the piston and lampshade [77]. The Muon Magnet South is approximately 1.5m shorter than the Muon Magnet North. This is to allow for movement of the PHENIX South Muon Arm for maintenance and access to other PHENIX components. The Muon Magnet North and Muon Magnet South each have an integrated field strength of 0.72 T·m at $\theta = 15°$.

The Muon Magnets produce radial magnetic fields which give charged particles helix-like trajectories [77], see Figure 3.7. The direction and degree of curvature

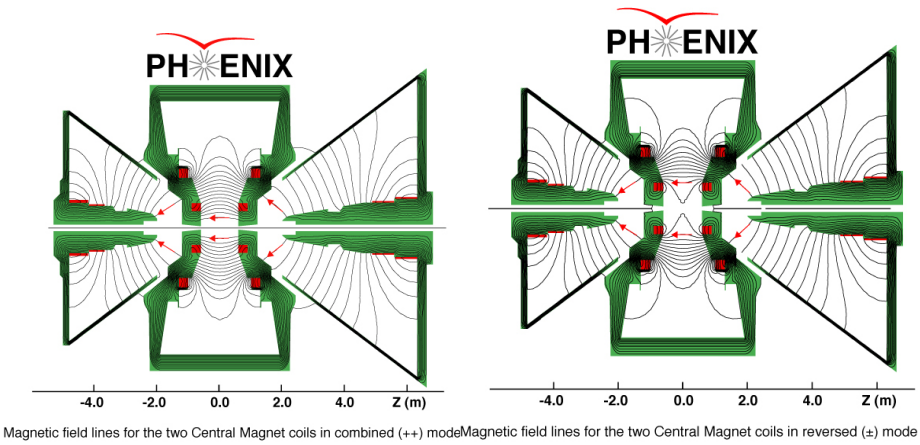

Figure 3.7: Magnetic field lines for the Central and Muon Arm Spectrometers in the ++ (left) and the +− (right) configurations. During Run 13, the ++ configuration was used.

are used to measure the momenta and charges of the particles passing through the MuTr.

3.2.3 Central Arm Spectrometers

The Central Arm Spectrometers are specialized for electron and photon detection, but also can identify charged mesons and baryons through their time-of-flight capabilities.

There are two Central Arm spectrometers, East and West, covering pseudo-rapidity $|\eta| \leq 0.35$ and 2π in ϕ. As this analysis focuses on the dimuon decay channel of the J/ψ and does not utilize the Central Arm Spectrometers, the description of the detector components will be brief. For vertex tracking around the collision region, the silicon Vertex detector (VTX), positioned nearest to the beam pipe with two layers of pixels inside two layers of silicon strips, is the main subsystem for precision tracking of collision vertices. In the 2013 run period, the VTX

was not functioning properly and cannot be used for vertex tracking in conjunction with muon arm vertex tracking. The Electromagnetic Calorimeter (EMCAL) provides calorimetry with either Pb-scintillator (PbSc) sampling, or Pb-glass (PbGl) Cherenkov components of the calorimeter[78]. The Drift Chamber (DC) and Pad Chambers (PC) allow for momentum tracking[79]. The Time of Flight (TOFEast and TOFWest) detectors allow for time of flight information from the collision and are used in coincidence with the BBC for start timing. The RICH detector provides particle identification and discrimination between electrons and pions[80].

3.2.4 Muon Arm Spectrometers

The Muon Arm Spectrometers, or Forward Arm Spectrometers, are specifically designed to detect muons with good hadron rejection. There are two muon detectors, north and south covering pseudo-rapidity range -2.25 $\leq \eta \leq$ -1.15 for the south arm and 1.15 $\leq \eta \leq$ 2.44 for the north arm. The south arm is slightly smaller to allow the detector arms to move for maintenance purposes. Both arms have Forward silicon Vertex Detectors (FVTX) in front of the central absorber, Muon Tracker detectors (MuTr), steel absorbers, Muon IDentifiers (MuID), and Resistive Plate Chambers (RPC)[81].

The Muon Tracker (MuTr) is designed for precision momentum tracking of charged particles. It consists of three stations of cathode strip readouts, divided into segmented octants, inside a conical shaped radial magnetic field in each arm. See Figure 3.8 for the internal structure of the MuTr. The radial magnetic field, see Figure 3.7, bends particles in azimuth and the MuTr can then track particle momenta and charge, depending on the direction of the bend in ϕ.

The mechanical construction for stations 1 and 3 is honeycomb technology with laminated copper-clad fiberglass epoxy material(FR-4) cathode strips. Station 1

consists of three chamber gaps, each containing a pair of cathode strip planes on either side of the anode wire plane. Station 3 has the same structure with two chamber gaps. Due to the multiple scattering limitation at Station 2 being more strict, it is made of etched aluminum clad mylar foils as the cathode strips. Station 2 has 6 cathode foils layered with three anode wire planes. The anode planes for each station are alternating structures of 20 μm gold-plated tungsten-sense wires and 75 μm gold-plated Cu-Be field wires with a sense wire spacing of 10 mm. Half of the cathode planes have strips perpendicular to the anode wires in approximately the radial direction and the other half have strips at stereo angles between 0° and $\pm$11.25° from the normal to the anode wires. A gas mixture of 50% Ar + 30% CO_2 + 20% CF_4 is circulated through the detector. Position resolution is $\sim$100μm per plane. The charge deposited by a minimum ionizing particle in the cathode strip chambers is calculated to be $\sim$100 electrons, which, after avalanche at the cathode wire, results in an average total cathode charge of 80 fC [81]. Particles passing through the MuTr then pass through a steel absorber which is the backplate of the muon magnet before passing through the MuID.

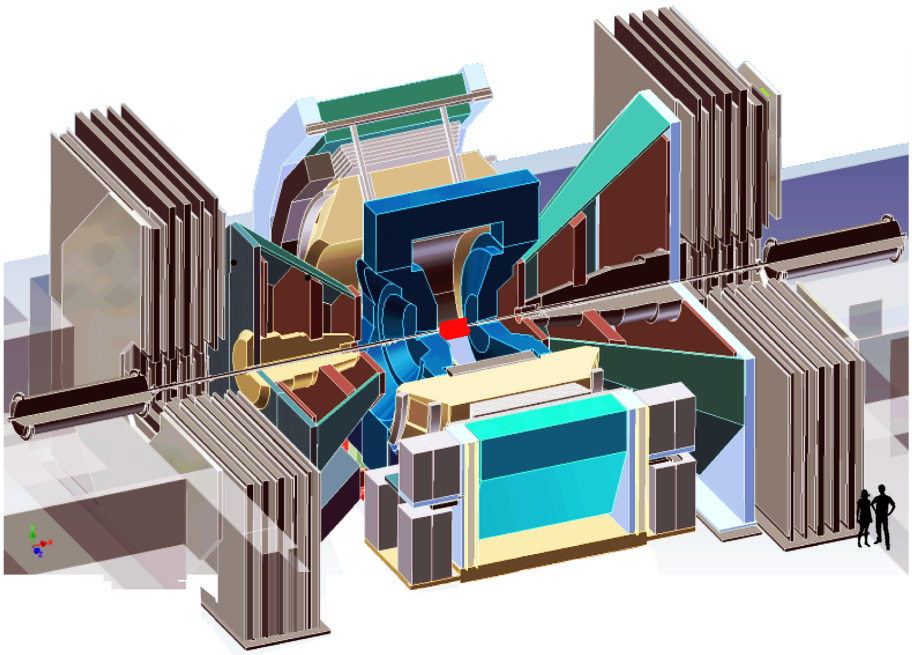

Figure 3.8: Quarter cutout of PHENIX showing internal structure of the Central and Muon Arm Subsystems. The FVTX is located in the area highlighted in red.

The Muon IDentifier (MuID) provides background rejection of pions for muon identification and the muon trigger. The MuID is constructed of 4 layers of steel absorbers of thicknesses 10 cm, 10 cm, 20 cm, and 20 cm, in between 5 gaps (including the MuTr backplate) of MuID panels of Iarocci tubes. See Figure 3.8 for a picture of the layering of the absorbers and gaps of the MuID. The layering of steel between gaps provides pion rejection, including those that decay into muons in flight. Iarocci tubes are 8.4 cm square planar drift tubes consisting of 100-μm gold-coated CuBe anode wires at the center of long channels of a graphite-coated plastic cathode. Within the tubes of the MuID, a gas mixture of CO_2 and up to 25% C_4H_{10} is circulated. Within the aluminum case of each gap, N_2 is circulated to keep the chamber electronics dry and clean, and to expel any flammable gas from leakage from the tubes. A muon at the vertex must have an energy of at least 1.9 GeV to reach the MuID system. The mean minimum original energy for a muon to penetrate completely through the

MuID is 2.7 GeV. A track is considered to be a muon candidate if it reaches the fourth gap in the MuID and then triggers the MuID muon trigger for that event. The charge candidate requires two separate signals from 3 out of 5 gaps, one in either the first or second gap and the other in either the fourth or fifth gap. Resistive plate chambers (RPCs) provide further muon identification and a fast muon trigger [81].

3.2.5 Data Acquisition and Triggering

Bunch crossings in RHIC happen every 106ns. For the high collision rate and the rare event physics goals of PHENIX, the data acquisition (DAQ) was designed to collect event data for several colliding beam species, from p-p to Au-Au. As a consequence, the DAQ must be flexible enough to accommodate event rates from a few kHz for central Au-Au collisions to approximately 500 kHz for minimum bias p-p collisions.

Triggering

The PHENIX online triggering system[82] consists of the Level-1 and Level-2 triggers. The Level-1 (LVL1) trigger is responsible for choosing events of interest. Fully pipelined, LVL1 is free of deadtime and is clock-driven from the 9.4 MHz RHIC clock.

Collision events which pass the LVL1 trigger are read out and passed to the LVL2 trigger. The results of the LVL2 trigger are data-driven to higher levels of data processing.

The most basic example of a LVL1 trigger, the Minimum Bias trigger, is fired when there are hits in at least one tube in both the North and South BBC during a beam crossing. This trigger is used to collect data with a minimum of trigger bias, and in coincidence with other triggers for selection of certain types of events. For example, the MUID1D trigger requires a minimum bias trigger together with

one track that penetrates into the fourth panel of the MuID. The MUID2D trigger requires two tracks that penetrate into the fourth layer of the MuID in coincidence with the minimum bias trigger, etc.

Due to the high luminosity of Run 13, multiple collisions during one bunch crossing happen more frequently than in previous run years. The efficiency of the MuID in turn decreases when there is a greater flux of charged particles passing through the Iarocci tubes. The tubes cannot return to their nominal voltage quickly enough for a track that passes through the tube to then meet the threshold voltage requirement for a muon trigger. Another effect of the multiple collisions is that there is a decrease in efficiency of the sending of the signals of the MUID1D and MUID2D triggers from the MuID FEMs to the GL1, resulting in missed muon candidates in event reconstruction. A full discussion of the effect of multiple collisions on the MUID2D trigger efficiency can be found in Section 4.6.

Data Flow

Data acquisition at PHENIX is a multi-step process which requires time synchronization for all subsystems, fast triggering, and synchronized event building for a bunch crossing with an appropriate event trigger. All detectors are timed in for proper synchronization before the start of a run period.

For PHENIX to record data, the 9.4 MHz RHIC beam clock is sent to the Master Timing Module (MTM) and then to the Global Level 1 Trigger (GL1) and the Granule Timing Module (GTM) where the RHIC beam clock is copied and distributed with appropriate delays to all subsystem Front End Modules (FEMs). The subsystems record analog signals that are then converted to digital ones through analog-to-digital converters (ADCs) and timing signals are processed by timing-to-digital converters (TDCs). Information from multiple beam clocks is stored in the

FEMs' multi-event buffering system.

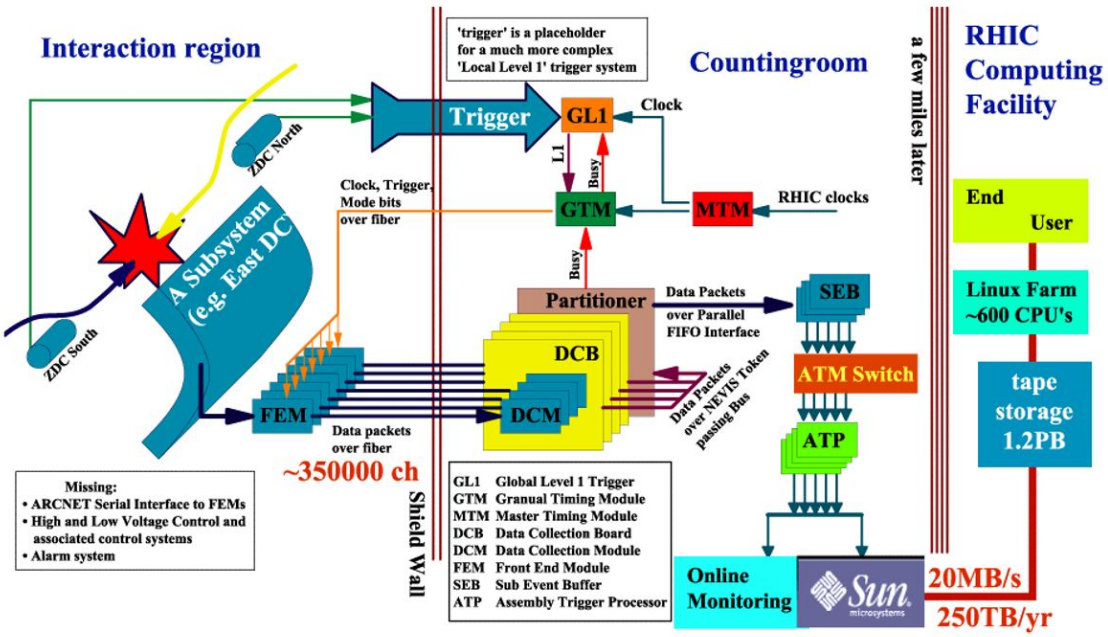

Figure 3.9: Schematic of PHENIX data flow

Subsystems, like the BBC and ZDC that are involved in triggering, send their data to the Local Level 1 trigger (LL1) FPGA to discern if the criteria for a trigger have been satisfied. If so, then the trigger signal is sent to the GL1, which sends a level 1 trigger signal to the GTM. The GTM, if not busy, sends the trigger signal for a specific beam clock to the FEMs of each subsystem. The FEMs send the digitized data signals for that beam clock event to the Data Collection Modules (DCMs). The signals are processed and inspected for quality before being organized into data packets and sent out in parallel to the Sub Event Builder (SEB) and then to the Assembly Trigger Processor (ATP) and subsequently sent on to short term storage on disk. Data packets are then processed by the PHENIX Online Control System (ONCS) and inspected by the shift crew for further quality assurance and subsequently sent to long-term storage at RCF[83]. A schematic of PHENIX data

flow can be seen in Figure 3.9.

3.2.6 FVTX

Before a particle passes through the MuTr, it must pass through a 30 cm absorber attached to the front of the nosecone of the Central Magnet. While this is good for hadron absorption, it causes scattering and uncorrelated background from hadron decays. Subsequently, this can distort tracking from the MuTr to the primary vertex. In order to improve vertex tracking before the Central Magnet, the Forward Silicon Vertex Tracker (FVTX) was implemented into PHENIX.

The FVTX[84], see Figure 3.10, was installed in 2012 at PHENIX and commissioned for the 2013 run period. The FVTX is composed of two annular endcaps to the four layer barrel silicon vertex (VTX) detector, each with four stations of silicon mini-strip sensors. Together they cover a rapidity range of $1.2 \leq |\eta| \leq 2.2$, for an event at z=0, that closely matches the two existing PHENIX muon arms with full azimuthal coverage.

Each station consists of 48 individual wedge-shaped 320μm n-type silicon sensors, each containing two columns of mini-strips with 75μm pitch in the radial direction and lengths in the ϕ direction varying from 3.4mm at the inner radius to 11.5mm at the outer radius. The two columns are mirror images about the completely active center line. Each sensor covers 7.5 degrees in ϕ. The strips are AC-coupled and biased through individual 1.5MΩ polysilicon resistors to a typical operating voltage of +70V. On the outer edges of the sensors are FPHX chips which are 128-channel front-end readout ASICs that are wire bonded to the sensors. The silicon sensors and FPHX chips are assembled on a High Density Interconnect (HDI) flex circuit which provides the slow control, power, calibration, and bias input lines, as well as the slow control and data output lines, see Figure 3.11. A total of 24 + 24 wedges

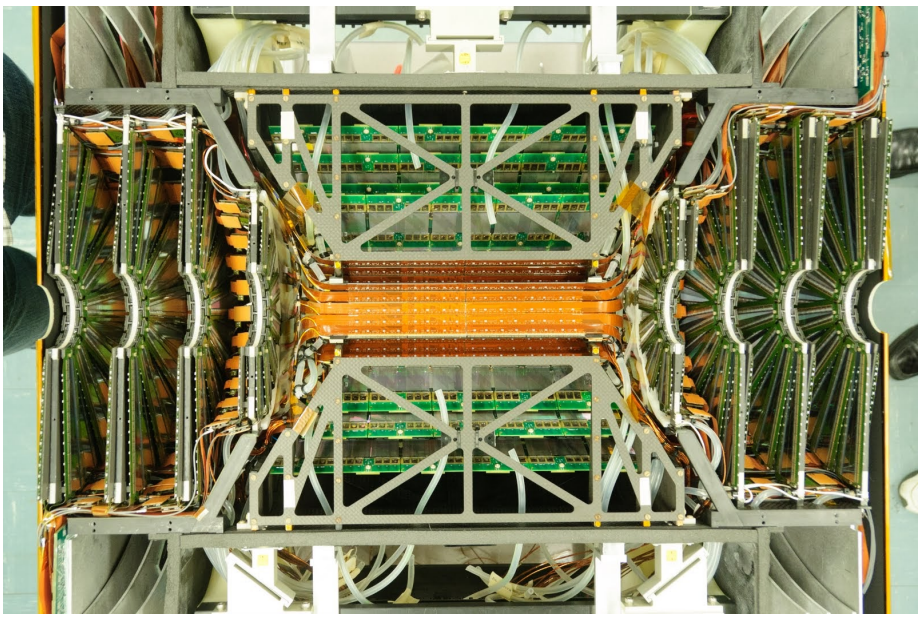

Figure 3.10: Photograph of half of the FVTX. There are four disks of silicon wedges for the north and south halves of the detector[85].

are mounted onto a disk, alternating in z to allow for full azimuthal coverage and fitted with extension cables. The disks are mounted into cages and the extension cables are connected to the Read Out Card (ROC) boards loaded directly in front of the central magnet nosecone. The cage and ROC board assembly is fitted to the carbon composite frame with the VTX, as shown in Figure 3.10.

With precision tracking in front of the absorber, the opening angle of muon pairs can be measured before any additional scattering occurs, giving a more precise dimuon mass and enabling the separation of the Ψ(2S) peak from the larger J/ψ peak in the dimuon mass spectrum. Additionally, the identification of tracks which originate away from the primary vertex enables rejection of muons from long-lived particles [84].

However, the FVTX is not used in this analysis as it requires muon tracks to have a reconstructed vertex of $|z| \leq 10$cm, which reduces statistics of $N_{J/\psi}$ detected in the

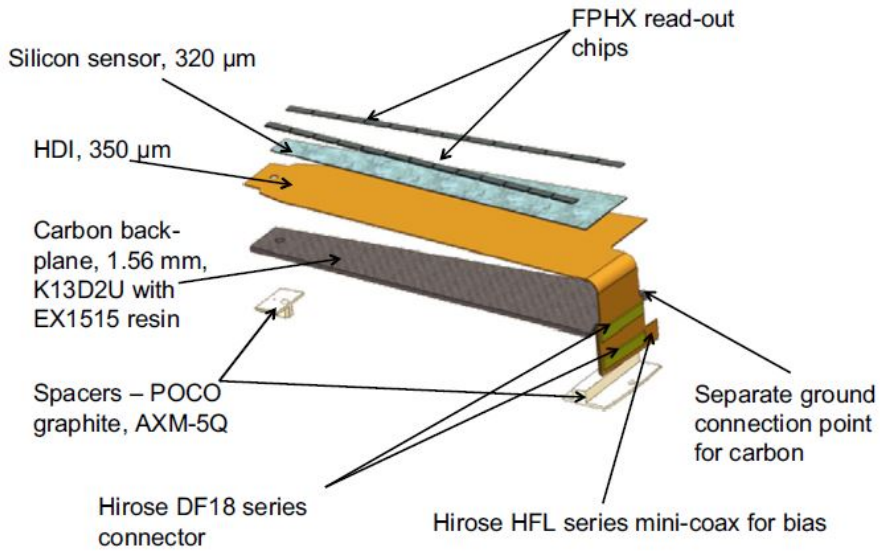

Figure 3.11: Exploded view of FVTX wedge assembly.

muon arms by a factor of three and adds unwanted systematic uncertainty through necessary track matching and between the FVTX and the MuTr. In p-p collisions, the J/ψ peak is quite prominent in comparison to the background, so therefore, the J/ψ analysis can be completed without the better resolution using the FVTX track reconstruction on the dimuon mass spectrum. This is not the case in heavy ion collisions where the backgrounds are much larger, and require the precision tracking and peak narrowing effects to adequately extract resonance peaks.

Radiological Studies of the Sensors

Silicon detectors, operated in collider environments where radiation exposure is high, can suffer radiation damage to the bulk silicon resulting in increased leakage currents and noise [86, 87, 88]. Wedge sensors of the FVTX were tested for radiation damage and longevity at Los Alamos National Laboratory by direct exposure to the 800 MeV proton beam at LANSCE [89]. Measurements of the radiation environment at RHIC

[90] were made to calculate the radiation dose delivered to the silicon sensors for the Run 12 p-p 510 GeV beam with integrated lumonosity of 30 pb^{-1}, and found to be $1.7 \times 10^{10} \frac{N_{eq}}{cm^2}$, where N_{eq} is the equivalent flux of 1 MeV neutrons. The equivalent flux of the proton beam at LANSCE is $2.5 \times 10^{10} \frac{p}{cm^2}$, which means the eight silicon sensors were exposed to 1, 5, 10 and 20 times the estimated annual dose at PHENIX without any applied bias. Immediately after testing, leakage currents were measured in-situ and found to increase proportionally with radiation dose, see Figure 3.12. To examine the effects of radiation on the bias voltage required for full depletion, the voltage at which the leakage current is 90% of the plateau value is compared to the operating bias voltage. Although there may be a small increase in the most irradiated sample, this is well below the typical operating bias voltage of 70V[84].

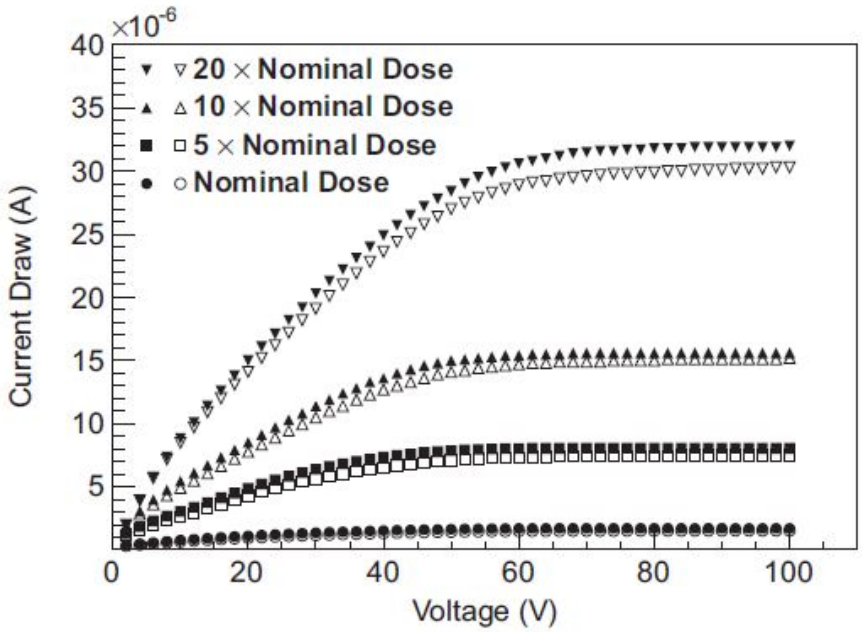

Figure 3.12: Leakage current as a function of bias voltage for the sensors after exposure to the LANSCE proton beam. The filled and open symbols differentiate the two different wedges exposed to a particular radiation dose.

Increases in leakage current[91] will decrease the effective applied bias voltage to the sensor, causing the silicon to not be fully depleted; and increase the sensor

noise, which, in turn, decreases sensor resolution. While the FVTX silicon sensors do show the expected increase in leakage current with the received radiation dose, the magnitude of the increases will not require any changes in the cooling system or bias voltage equipment over the expected life of the experiment. For more information on radiological studies on the FVTX sensors, please see [84].

FVTX Construction and Assembly

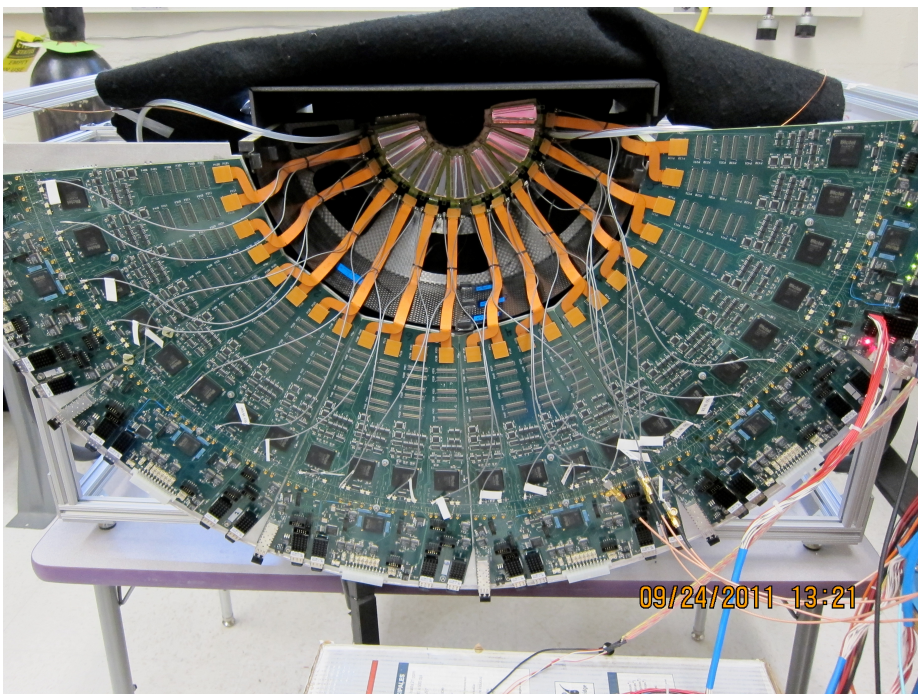

Figure 3.13: Photograph of assembled disk with attached, bent extension cables and ROC mounted on assembly cage.

The construction of the FVTX began in 2010, and the assembly of wedges into disks, and mounting of the disks into cages with the ROCs, see Figure 3.13, began in 2011. All completed wedges were subjected to testing with a β source prior to the High-Density Interfaces (HDIs) being bent in order to fit into the allowed detector geometry. In a metal bending jig, designed and built at UNM, the HDIs were bent at

100°C to the desired angle for the disk, typically around 90°. The angle of the bent HDIs did relax by about 10°, but the angle relaxation did not affect the detector assembly. The wedges were then tested again with the β source to ensure no damage occurred to the wedge sensor during bending. Once a disk of wedges was assembled, it was sent to Hexagon Metrology for surveys of positioning of the sensors.

Extension cables of different lengths and shape for each wedge position and disk, were also bent to fit the detector geometry to accommodate the VTX. A metal assembly frame was constructed to support the cages of disks with the metal cooling plates and attached ROCs and extension cables for assembly and transport. Thermal cooling pads were cut to shape and affixed to the metal cooling plates and ROCs.

FVTX Performance

During Run 13, the FVTX performed quite well in terms of efficiency and live area. The FVTX had an overall live area of greater than 95% and single particle hit efficiencies peaked at over 95%. Additionally, position resolution for each of the 8 stations was between 24μm and 28μm, and noise levels were between 350 and 380 electrons indicating that the FVTX functioned well within the design parameters during Run 13. The FVTX was found to be capable of multiplicity triggering, which was not planned in the design, and this triggering system was implemented during Run 15.

Chapter 4

Production Cross Section Measurement of the J/ψ

The inclusive production cross section of the unpolarized J/ψ meson is measured for the RHIC Run 13 dataset of p-p collisions at $\sqrt{s} = 510$ GeV. The total particle cross section is defined as the number of J/ψ's produced divided by the integrated luminosity of the proton beams

$$\sigma(pp \to J/\psi \to \mu^+\mu^-) = \frac{N_{J/\psi}^{\text{produced}\to\mu^+\mu^-}}{\mathcal{L}_{\text{integrated}}} \tag{4.1}$$

where the integrated luminosity is determined by the number of minimum bias events, N_{MB}, and the minimum bias trigger cross section, σ_{BBC}, and is written as

$$\mathcal{L}_{integrated} = \frac{N_{MB}}{\sigma_{BBC}}. \tag{4.2}$$

Alternatively, the integrated luminosity can be directly calculated from the beam and run parameters. From section 2.4.1, the invariant cross section is measured experimentally as

$$\frac{d^2\sigma}{dydp_T} = \frac{N_{J/\psi}^{\text{det}}}{\Delta p_T \Delta y A \epsilon_{reco} \epsilon_{trig} B_{\mu\mu}} \frac{1}{\epsilon_{hard} \mathcal{L}_{int}} \tag{4.3}$$

where

$$N_{J/\psi}^{\rm det} = A\epsilon_{reco} \cdot \epsilon_{trig} \cdot B_{\mu\mu} \cdot N_{J/\psi}^{\rm produced} \tag{4.4}$$

is the number of detected J/ψ particles, A is the detector acceptance, $\epsilon_{\rm reco}$ is the reconstruction efficiency, ϵ_{trig} is the trigger efficiency, ϵ_{hard} is the efficiency of the minimum bias trigger for events containing hard scattering, and $B_{\mu\mu}$ is the branching ratio for dimuon decay channel of the J/ψ.

The minimum bias cross section, σ_{BBC}, is discussed in detail in the next chapter.

4.1 Quality Analysis

4.1.1 Run Quality Analysis

To verify the stability of the detector during Run 13, a quality analysis of the data is conducted, and runs with poor detector performance are removed from analysis. Quality analysis aims to remove runs with detector malfunctions during the middle of a run. Additionally, stable detectors throughout the run period enable simulations to be better matched to data. To test this, the number of dimuon tracks per event is taken for each run with triggers from the ((MUIDLL1 N2D||S2D)||(N1D& S1D))& BBCLL1(noVtx) triggered data set. A dimuon track must pass through the MuTr and the fourth panel of the MuID. The opening angle of low transverse momentum dimuons must be large enough to pass through separate octants of the MuTr. The track must also match between the MuTr and MuID within a 30cm transverse separation and have an angular difference of less than 40°. The number of dimuon tracks per event with pertinent J/ψ candidate selections are used as a quality indicator on a run-by-run basis and any run that falls outside of 3σ of the mean is excluded from the analysis. The quality analysis found 983 good North Arm Runs and 995 good

South Arm runs. Please see Appendix C for a list of all runs used in this analysis.

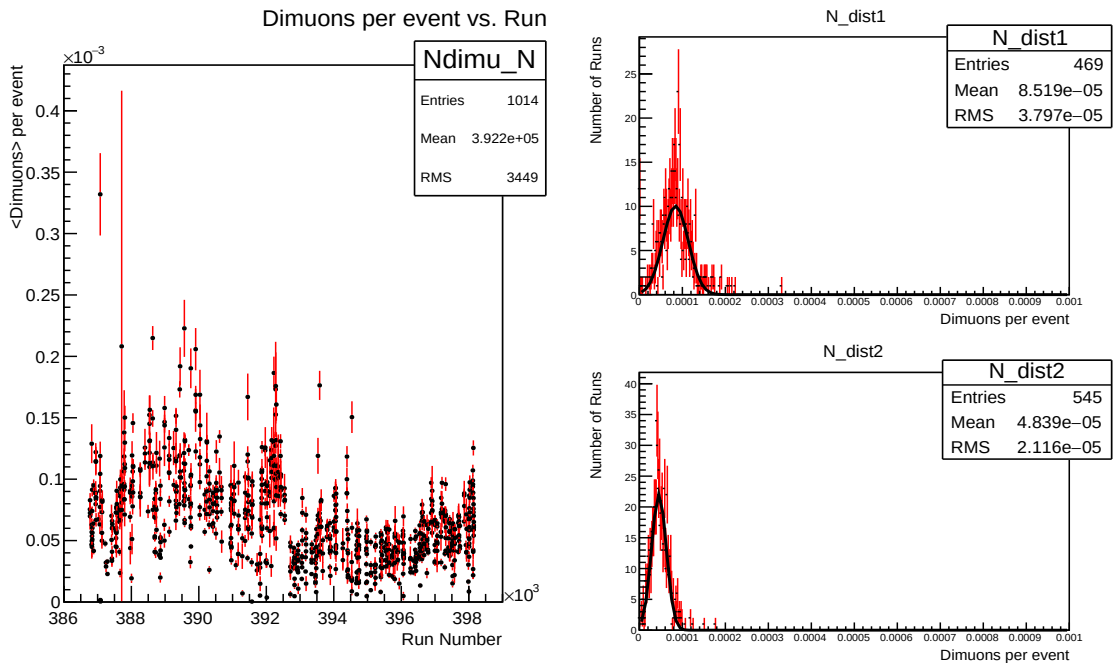

Figure 4.1: Quality analysis for the North Arm. The average number of dimuons per event is calculated for each run (left). The number of dimuons per event for all runs prior to run 392600 (top right). The number of dimuons per event for all runs after run 392600 (bottom right). Both distributions for dimuons per event were fitted with Gaussians, and any run outside 3σ from the mean was excluded.

Run 13 saw a shift in overall muon spectrometer performance around run 392600. This is evident in the dimuons per event vs. run number plots for both the North and South Arms, see Figure 4.1 and Figure 4.2, as the average number of dimuons per event for the second half of the run period decreased. The run quality analysis was subsequently split to reflect the average detector performance from each half of the run period. If the number of dimuons per event for a particular run was outside the 3σ cutoff for that run half, it was excluded from analysis.

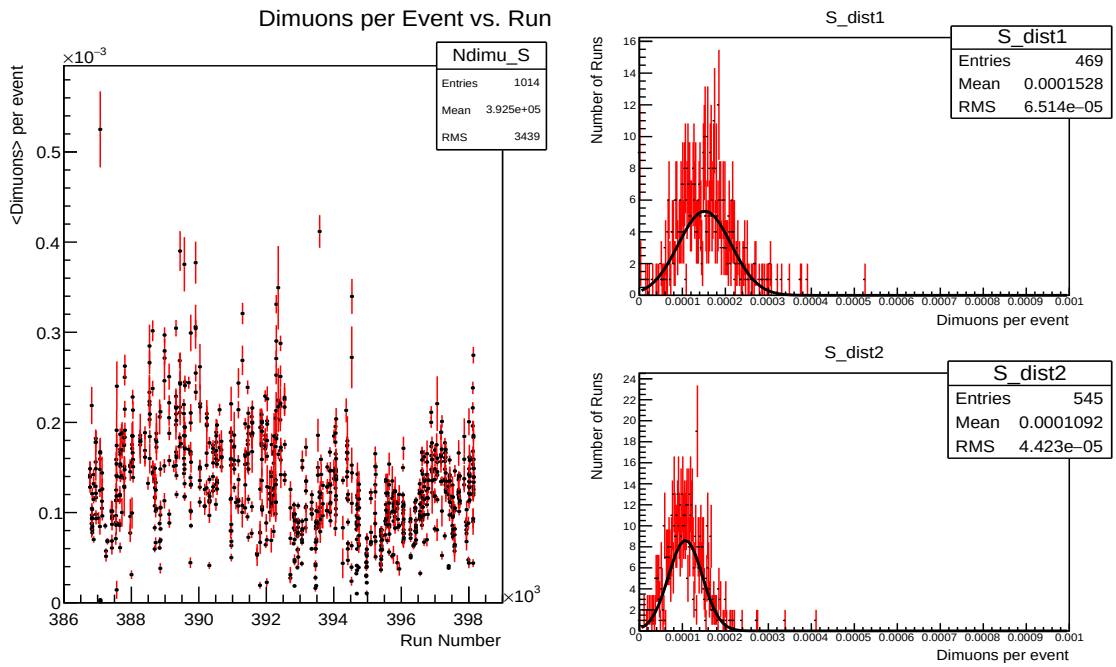

Figure 4.2: Quality analysis for the South Arm. The average number of dimuons per event is calculated for each run (left). The number of dimuons per event for all runs prior to run 392600 (top right). The number of dimuons per event for all runs after run 392600 (bottom right). Both distributions for dimuons per event were fitted with Gaussians, and any run outside 3σ from the mean was excluded.

4.1.2 Event Quality

After the runs have been sorted to include only good runs, i.e., those during which the detector is stable and did not experience a malfunction, the events themselves need to be evaluated for quality. An event of interest is an event that triggers both the Minimum Bias BBC trigger and the ((MUIDLL1 N2D||S2D)||(N1D& S1D))& BBCLL1(noVtx) trigger. All events that have a vertex outside of $|z| \leq 30$cm are rejected from the analysis. The χ^2 of the event vertex, *Evt_vtxchi2*, is also limited to ensure accurate vertex resolution.

Individual muon tracks are evaluated for quality and proper continuity through

the different detector subsystems. A muon track candidate creates tracks through the MuTr and roads while passing through the MuID. The tracking algorithm in reconstruction matches MuTr tracks with MuID roads. This is accomplished by projecting a track from the third station of the MuTr to the first panel of the MuID within a specific angle and distance. Muon scattering through the absorbers in the detector is inversely dependent on the muon total momentum. This requires that the tracking variables DG0 and DDG0 scale with momentum when applying track quality selections. The distance between the track and the road in the transverse plane is specified by the parameter $DG0$ in reconstruction, while the angle between the track and the road is represented by $DDG0$. Hard cuts on these momentum-independent variables can needlessly throw out some of the J/ψ signal, so momentum dependent quantities are introduced that provide more efficient selections on muon tracks. The selections for these variables are listed in Table 4.1.

A muon candidate must have a MuTr track of suitable quality to be used for analysis. The fit of hits to a track, the $\chi^2/d.o.f$ of a MuTr track, must be sufficiently small to be a proper muon candidate. Similarly, the $\chi^2/d.o.f$ of a reconstructed road in the MuID must be sufficiently small to be considered a muon candidate.

For a specific track to be considered a muon candidate, the road must pass through 4 layers of the MuID. The 35cm steel absorber outside of the volume of the central arm magnet reduces hadronic background by $\sim 10^{-3}$, and the steel plates between the gaps of the MuID provide further rejection. This rejects most hadronic background as hadrons cannot penetrate through the layers of steel absorbers between each MuID gap. This is represented by the parameter *lastgap* in reconstruction.

For a particle to pass through the absorber in front of the MuTr and through the MuTr to the fourth panel of the MuID, a particle must have a minimum longitudinal momentum, p_z, as determined by previous simulations. Any track that has a longi-

tudinal momentum less than 2 GeV is considered to be noise, or other background, and is rejected from analysis. Accordingly, to consider the transverse momentum and limited detector acceptance at low p_{T}, a total momentum cut is placed on the muon track.

Cut	Description
lastgap = 4	A muon candidate must pass through the fourth gap of the MuID
$id\chi^2 < 3$	The χ^2 fit of a MuID road must be less than 3
$tr\chi^2 < 30$	The χ^2 of a MuTr track must be less than 30
$ntrhits \geq 11$	The number of hits detected in the MuTr must be greater than 11
$nidhits > 6$	The number of hits detected in the MuID must be greater than 6
$DG0 \times p < 80$ S (< 60) N	$DG0$ is the distance between a track being matched from the MuTr to a road in the MuID. This quantity is dependent upon track momentum
$DDG0 \times p < 40$S/N	$DDG0$ is the angle between a track from the MuTr that is being matched with a road from the MuID. It is also dependent upon track momentum
$\|p_z\| > 2$ GeV	In order for a muon candidate to pass through the detector to the fourth gap of the MuID, the longitudinal momentum must be greater than 2 GeV
$p > 2$ GeV	A muon candidate's total momentum must be greater than 2 GeV in order to pass through the detector to the fourth gap of the MuID
charge = 0	assures that the dimuon is made up of one μ^+ and one μ^-

Table 4.1: Muon and dimuon track selection criteria.

The charge of the dimuon is required to be zero and both tracks must come from the same Minimum Bias event.

To constrain tracks to the fiducial geometry of the muon spectrometers, rapidity cuts are placed on reconstructed muon candidate tracks.

$\|Evt\_bbcZ\| < 30$	Places a 30cm z-vertex cut on the dimuon
$Evt\_vtxchi2 < 8$ N (< 6) S	Places a limit on the χ^2 of the event vertex reconstruction
$same\_event = 1$	Two muons in a dimuon must come from the same BBC triggered event
$-2.2 \leq y \leq -1.2$	South Arm rapidity cut. Assures muon candidates in the South Arm pass properly through the geometry of the spectrometer
$1.2 \leq y \leq 2.4$	North Arm rapidity cut. Assures muon candidates in the North Arm pass properly through the geometry of the spectrometer

Table 4.2: Muon track quality cuts used on muon candidates in Run 13 J/ψ analysis.

4.2 Background Subtraction

Even though the signal-to-background ratio of the J/ψ meson is quite large, to measure the correct yield all background contributions to the dimuon mass spectrum must be accounted for, and subtracted out. There are two main types of background that are present in particle colliders. Correlated background and uncorrelated background.

Uncorrelated background comes from combinatorial associations between muon tracks in the reconstruction algorithm where one or both muon tracks comes from a particle that is not a J/ψ, with all tracks passing the above event cuts. Uncorrelated background can include punch-through hadrons, and muons from hadronic decays in the absorber or MuTr. Two methods are considered to determine the uncorrelated background contribution to the dimuon mass spectrum. They are the like-sign method and the mixed event method.

The mixed-event method is applied to count uncorrelated background events and uses unlike-sign muon tracks from different events. The event mixing algorithm at PHENIX takes unlike-sign muons from up to five different events and mixes the tracks to form uncorrelated $\mu^+\mu^-$ dimuons. The resulting invariant mass is not physical and does not contribute to particle resonance[92]. The contribution from mixed-event pairs can be seen in Figures 4.5a and 4.5b. The mixed-event normalization factor is

$$N_{\text{mixed}} = \frac{2\sqrt{N_{++}N_{--}}}{N_{+-}^{\text{mixed}}} \tag{4.5}$$

where N_{+-}^{mixed} is the number of mixed-event unlike-sign pairs.

An important effect of using the mixed event method of background subtraction is the reduction in statistical uncertainty. The total statistical uncertainty for the signal, S, and background, BG, is written as

$$\sigma = \sqrt{\sigma_S^2 + \sigma_{BG}^2} \tag{4.6}$$

where $\sigma_S = \sqrt{S}$ and $\sigma_{BG} = \sqrt{BG}$. Thus,

$$\sigma = \sqrt{S + BG}. \tag{4.7}$$

When the background is normalized by N, from the mixed-event or like-sign method, the uncertainty from the background becomes

$$\sigma_{BG} = \frac{\sqrt{NBG}}{N} \tag{4.8}$$

and the total uncertainty from a source of background becomes

$$\sigma = \sqrt{S + \frac{BG}{N}} \tag{4.9}$$

The like-sign method utilizes like-sign dimuons, e.g., $\mu^-\mu^-$ and $\mu^+\mu^+$ of the same event to determine part of the uncorrelated combinatorial background contribution.

The invariant mass of like-sign dimuons is plotted using the same event quality cuts as unlike-sign pairs. The like-sign spectrum is normalized by [92]

$$N_{\rm ls} = \frac{2\sqrt{N_{++}N_{--}}}{N_{++} + N_{--}} \tag{4.10}$$

where N_{++} and N_{--} represent the number of like-sign pairs of their type, before these quantities are subtracted from the spectrum of unlike-sign pairs from the same event. The like-sign method does not take into account all sources of like-sign background. Some correlated pairs from other charmonium decays yield like-sign decay products. Therefore, the like-sign method is not used for yield extraction purposes, but as a cross-check on the mixed-event background. The results from the like-sign and mixed-event backgrounds should be similar.

Correlated background comes from sources of other processes that have muonic decays. Correlated muon pairs come from open-charm and open-bottom decays, as well as Drell-Yan events, and quarkonia decays. Background from these processes remains after subtracting background from the mixed-event method. Correlated background from these processes forms the background continuum and is fit with an exponential above and below the J/ψ mass peak, see Figures 4.5a and 4.5b.

4.3 Yield of Detected J/ψ's

Dimuon mass spectra are fit in different transverse momentum and rapidity bins for each Muon Arm after passing through the event selections discussed in section 4.1.2, in order to extract the invariant yield. The invariant mass of a dimuon is calculated by using the reconstructed momentum through the MuTr. The invariant mass of the dimuon, also referred to as rest mass, is the same in all reference frames and is measured using conservation of energy and momentum of the muons, and gives the invariant mass of the parent particle, the J/ψ meson. The total fit function

accounts for the normalized combinatorial background, an exponential function to fit the correlated dimuon background, and a Crystal Ball function is fit to the J/ψ and ψ' mass peaks. This fit is applied to each transverse momentum and rapidity bin, see Figures 4.5a and 4.5b. A Crystal Ball function is a Gaussian with a power-law tail on the low-mass side. They are used to model energy loss of the J/ψ due to radiative decay, which causes a longer tail on the low-mass side of the J/ψ peak[93, 94, 95, 96]. The Crystal Ball function is of the form

$$f(x;\alpha,n,\bar{x},\sigma) = N \begin{cases} \exp\left(-\frac{(x-\bar{x})^2}{2\sigma^2}\right) & \text{for} \frac{x-\bar{x}}{\sigma} > -\alpha \\ A \cdot \left(B - \frac{x-\bar{x}}{\sigma}\right) & \text{for} \frac{x-\bar{x}}{\sigma} \leq -\alpha \end{cases}$$

where

$$A = \left(\frac{n}{|\alpha|}\right)^n \cdot \exp\left(-\frac{|\alpha|^2}{2}\right),$$
$$B = \frac{n}{|\alpha|} - |\alpha|,$$

N is a normalization factor, and α, n, and σ are fit parameters. The parameters α and n are fixed from fits to the simulated dimuon mass spectrum from generated J/ψ signals, and the simulation is discussed in the following section. For fitting the data, the shapes of the J/ψ and ψ' resonance peaks are expected to be the same shape as they are both subject to energy loss in the absorber; therefore both resonances are fit with the same Crystal Ball parameters α and n from the fits to the J/ψ simulation. The width of the $\psi\prime$ peak is expected to be greater than that of the J/ψ peak, as it is heavier, and the decay products have higher momentum, which in turn decreases the momentum resolution of the MuTr and ultimately the mass resolution of the peak.

The ratio of widths of the $\psi\prime$ to the J/ψ is set to be 1.15, in accordance with simulations conducted in the Run 13 $\psi' \to \mu^+\mu^-$ analysis [97].

The mixed-event data is normalized according to the procedure in the next section and fit with an exponential function that represents the shape of the mixed event

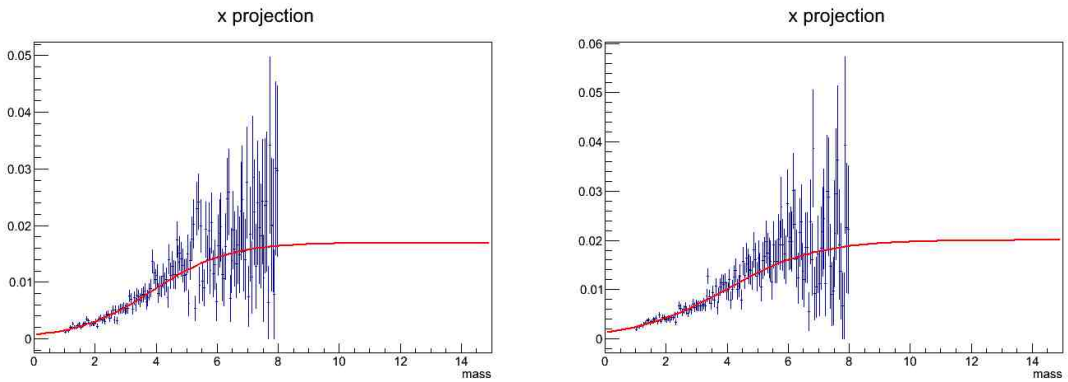

Figure 4.3: The acceptance × reconstruction efficiency vs. mass for North (left) and South (right) for $9 \leq p_T < 12$ GeV. The distributions are fit with Equation 4.12.

data well for all kinematic bins and is of the form

$$f_{\text{mixed}} = \frac{N_{\text{mixed}}}{\left(\exp\left(-A_m x - B_m x^2\right) + x/C_m\right)^{D_m}} \tag{4.11}$$

where N_{mixed}, A_m, B_m, C_m, and D_m are fit parameters. This form is based off of the shape of the transverse momentum spectrum of hadron decays that generate combinatorial background.

The background exponential needs to take into account the shape of the acceptance × reconstruction efficiency for that specific kinematic bin to correctly model the shape of the background. The shape of the acceptance × reconstruction efficiency is fit as

$$f_{A\epsilon_{reco}} = \frac{N_{sim}}{\left(\exp\left(\frac{(A_{sim}-x)}{B_{sim}}\right)+1\right)} \tag{4.12}$$

and the fit parameters A_{sim} and B_{sim} are taken from the fit function and applied to the background exponential. The background exponential is of the form

$$BG_{exp} = N_{BG} \times \frac{\exp(-xN_{BG} + A_{BG})}{\left(\exp\left(\frac{(A_{sim}-x)}{B_{sim}}\right)+1\right)}. \tag{4.13}$$

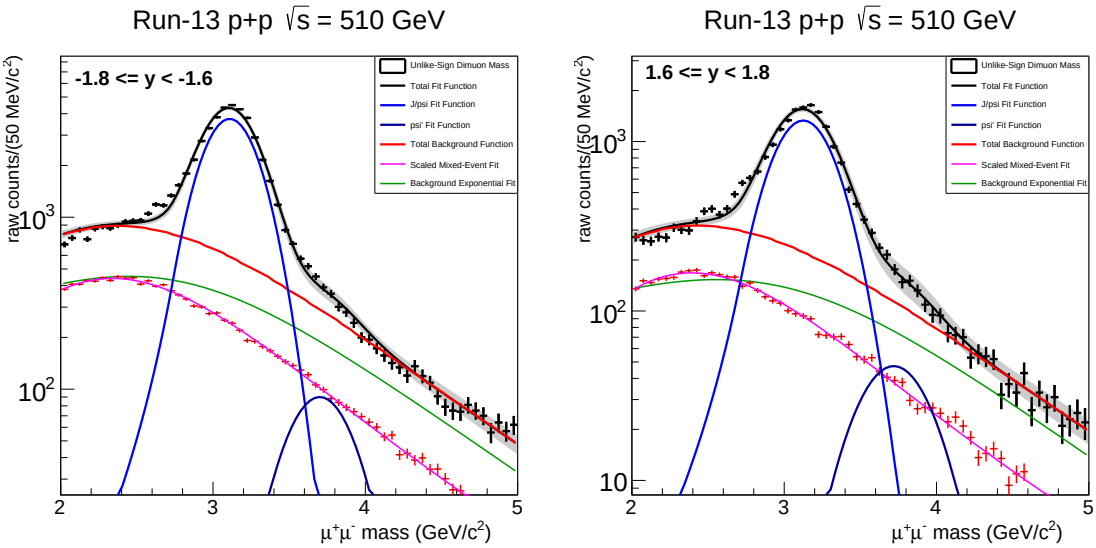

Figure 4.4: Dimuon mass spectra of South Arm dimuons (left) with $-2.0 \leq y < -1.8$ and North Arm dimuons (right) with $1.4 \leq y < 1.6$, fitted with a Gaussian and Crystal Ball function for the J/ψ and $\psi\prime$ mass peaks. The red curve is the exponential fitted to the correlated background that forms the continuum. The blue curve represents the mixed-event data.

The total background function is the sum of the mixed-event fit and the background exponential

$$BG_{tot} = BG_{exp} + f_{\text{mixed}}. \tag{4.14}$$

The total fit function for the dimuon mass spectrum is a sum of the Crystal Ball functions for the J/ψ and ψ' and the total background function, and is expressed as

$$f_{tot} = f_{J/\psi}(m; \alpha, n, \bar{m}, \sigma_{J/\psi}) + f_{\psi\prime}(m; \alpha, n, \bar{m}, \sigma\psi\prime) + BG_{tot}. \tag{4.15}$$

The invariant yield is extracted by integrating the J/ψ Crystal Ball fit function over the mass range and then subtracting the total background over the same range.

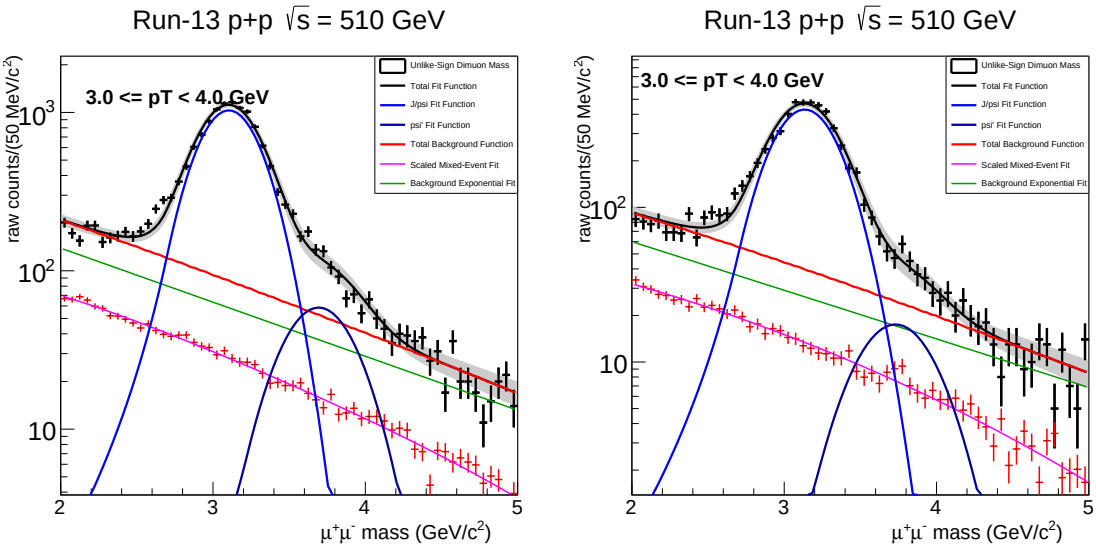

Figure 4.5: Dimuon mass spectra of South Arm dimuons (left) and North Arm (right) with $2 \leq p_T < 3$ GeV, fitted with a Gaussian and Crystal Ball function for the J/ψ and ψ' mass peaks. The red curve is the exponential fitted to the correlated background that forms the continuum. The blue curve represents the mixed-event data.

4.4 Simulations

Not all of the produced J/ψ muons in PHENIX are detected by the PHENIX Muon Arms. The geometric acceptance of the detector must be considered, as well as the efficiency of the detectors and reconstruction algorithms. These parameters serve as correction factors to the raw invariant yield. In order to determine the product of the acceptance and the reconstruction efficiency, it is necessary to know exactly how many J/ψ mesons were produced and compare it to how many were reconstructed. This can be accomplished by running a simulation of generated J/ψ signal propagated through the PHENIX detector and processed with the PHENIX event reconstruction framework.

4.4.1 PYTHIA Event Generation

The event generator used for J/ψ simulations in this analysis is PYTHIA 6[98]. PYTHIA processes can include parton distributions, both initial- and final-state parton showers, hard and soft interactions, fragmentation, particle decays, etc. Proton collisions are generated for a beam collision energy of 510 GeV, representing the 2013 RHIC dataset, to generate J/ψ meson signals. The dimuon decay channel is selected as the preferred decay process, see Appenxix A. To represent 829 runs of the 2013 dataset, 25,000 J/ψ's were thrown from a random Gaussian distribution with the collision vertex was set to be $z = 0$ cm with $\sigma = 30$ cm for each run.

4.4.2 PISA

Simulated muons generated by PYTHIA have initial momenta that are then propagated through the detector geometry, magnetic fields, and materials through a GEANT3[99] simulation. The GEANT3 configuration for PHENIX is the PHENIX Integrated Simulation Application (PISA). PISA returns raw hit information from the detectors and triggers that represent simulated particles interacting with the detector, had they been real particles. This accounts for energy loss while a muon passes through detector material, and trajectory bending while passing through magnetic fields. The data files of the raw hit and trigger information are referred to as PHENIX raw data files (PRDFs) and are $\sim 50 - 100$ MB and the structure is not trivial to navigate for analyses.

4.4.3 Reconstruction

The PRDFs are then converted to Data Summary tapes (DSTs) through a process called reconstruction using the PHENIX Fun4All framework that is also used in

collision data reconstruction. Reconstruction takes the raw detector hit information from PRDFs and translates it into more easily analyzable quantities. The DSTs are much more user friendly and store data in a compressed form of ROOT files in a data architecture called TTrees.

For each simulation, detector information was applied to the reconstruction phase to represent detector deadmaps. The MuTr high voltage information was iterated through actual run high voltage information of Run 13 for a data-driven simulation. MuTr disabled, dead, and attenuated channel information was studied for Run 13 by the PHENIX W-analysis group[100, 101, 102], and selected for reference run 393888 that represents a good average deadmap for the 2013 dataset. Additionally, the MuTr and MuID tube efficiencies are applied to the track reconstruction algorithim. The MuID tube efficiency was significantly affected by multiple collisions per bunch crossing, discussed in section 4.8[103]. The MuID tube efficiency information used in simulation accounts for the changes in tube efficiency with changing event rate based upon multiple collisions.

One reliable way to determine the the accuracy of the simulations' ability to replicate the data is to compare the azimuthal ϕ distributions from the third station of the MuTr from the simulation to the data. If the two distributions match, then the simulation represents the detector deadmaps and performance well over the course of the run. If the distributions do not match well, see Figure 4.6, then that is a good indication that detector performance was not accurately modeled, and the reconstruction phase should be reexamined for any oversights in detector performance. When the correction factors to the yield, the acceptance, reconstruction efficiency, and trigger efficiency, were calculated from this simulation and applied to the yield, there was a 20-30% difference in the differential cross section as a function of transverse momentum between the North and South arms. This led to the study of effects of multiple collisions in the MuTr.

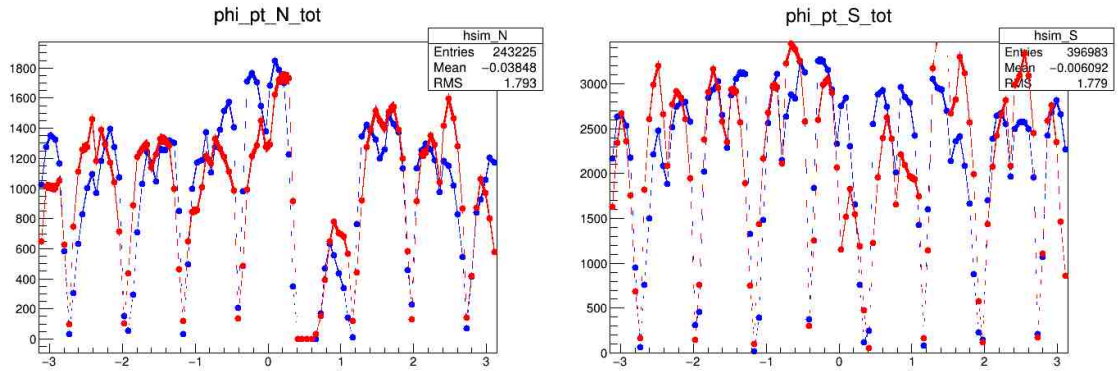

Figure 4.6: ϕ distributions of the simulation (blue) and data (red) for the North (left) and South (right) arms. The ϕ distribution should be similar for simulation and data to make sure all dead areas are accounted for, and that the simulation is as close to the collision data as possible. As the azimuthal distributions of simulation and data do not match well, this indicates that the simulation needs further tuning.

4.5 MuTr Hit Efficiencies and Pile-up

After several iterations of simulations using various reference runs, and even detector deadmap information for a run-by-run basis, it was clear that the simulation would not match the data with the available detector efficiency information, see Figure 4.6. This was a recurring issue with the 2013 dataset for muon analyses. The suspected cause of this inconsistency between simulation and data was that the MuTr hit efficiencies were lower than reported. This is due to pile-up in the detector due to higher luminosity that the detector was not designed to accommodate. In order to accurately quantify the MuTr hit efficiencies, a few steps had to be taken. First, real data was examined without any bias from any other detector with suspected luminosity dependent efficiencies. This required the use of Minimum Bias data, that does not require any triggering from any other detector in the North and South Arms. This data had to then be taken from its raw PRDF format and run through a special reconstruction algorithm that removed the MuID from triggering and track

reconstruction. The MuID has a luminosity dependence on its muon triggers and tube efficiencies, see Section 4.6.

The next step was to plot the number of hits per plane and hits per half octant. A Mutr plane was then isolated and a high quality muon track was reconstructed from the filtered data without MuID dependence. The track was then projected into the plane and half octant of interest. If the projection point was near a dead wire or cathode as defined from the Run 13 W analysis[100, 101, 102], the track was rejected. The MuTr hit efficiency is defined as the ratio of MuTr plane hits, in a cluster, that match track projection from the FVTX and satisfies the requirement to be a good quality track.

Hit efficiency was measured for each arm, station, gap, panel, plane, and half octant, see Figure 4.7. This was completed for every available run in a fill that had several runs from high luminosity to low luminosity. It was found that there is a linear dependence of the hit efficiency on the event rate, which is a proxy for luminosity. An average hit efficiency for each arm, station, gap, panel, plane and half octant was found for each run in the 2013 dataset.

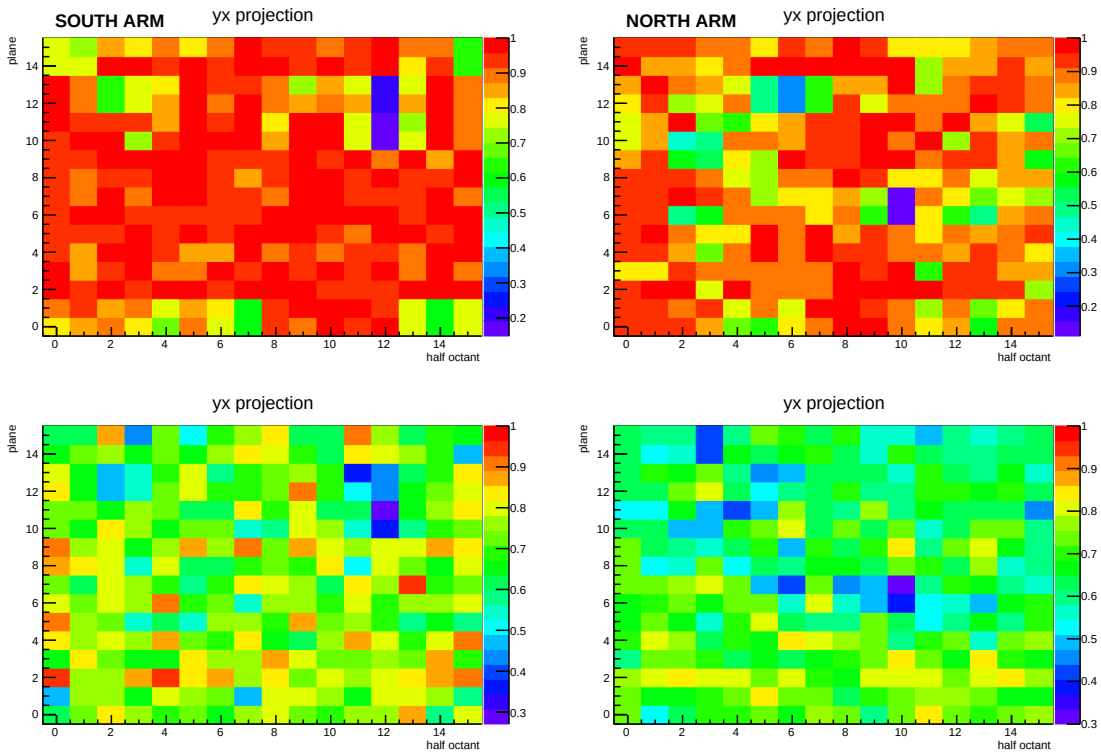

Figure 4.7: Hit Efficiencies for the South arm (left) and North arm (right) for low luminosity (top) and high luminosity from data. The y-axes are planes, and the x-axes are half-octants. The hit efficiencies at high luminosity were found to be $\sim 70\%$, much lower than the expected 99%. The blue areas represent dead areas.

This same process was then completed for single muon simulations, with complete removal of the MuID from track reconstruction. Prior to making changes to the simulation framework, it was verified that the MuTr hit efficiency did not decrease from low beam luminosity to high luminosity, see Figure 4.8. This provided confirmation that the simulation did not account for pile-up effects in the MuTr.

Correction factors for the hit efficiencies of each plane and half octant in the simulation were then calculated by taking the ratio of the average hit efficiencies for each run in real data and then dividing them by the hit efficiencies in the uncorrected simulation reconstruction framework. These correction factors were then

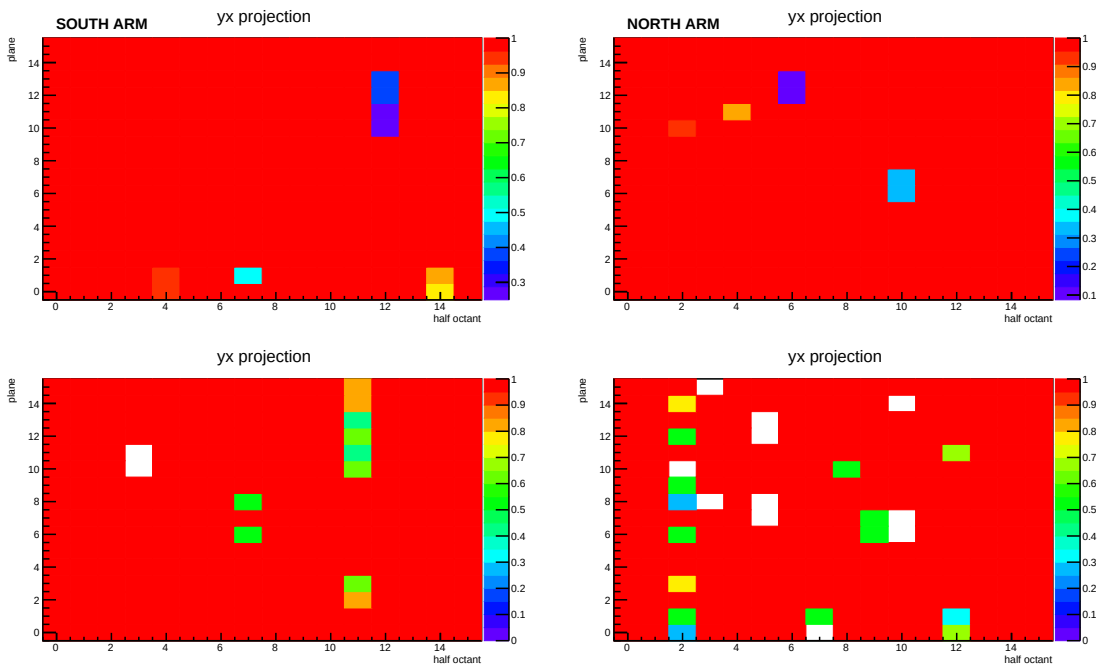

Figure 4.8: Hit Efficiencies for the South arm (left) and North arm (right) for low luminosity (top) and high luminosity from simulation. The y-axes are planes, and the x-axes are half-octants. The hit efficiencies at high luminosity were similar to the hit effciencies at low luminosity. The blue areas represent dead areas, and the green and white areas indicate dead or poorly performing planes or half octants.

implemented into the PHENIX simulation reconstruction framework for Run 13 by multiplying them by the original simulation MuTr hit efficiencies for each panel and half octant of the MuTr.

Verification that the correction factors were being implemented was performed, and the process of finding the hit efficiency was performed again for the simulation for runs representing low and high luminosity of the 2013 dataset, see Figure 4.9. Although the hit efficiencies from low to high luminosity do not decrease exactly as is the trend with the data, see Figure 4.10, the new high luminosity hit efficiencies in the simulations better represent the data, see Figures 4.9 and 4.11.

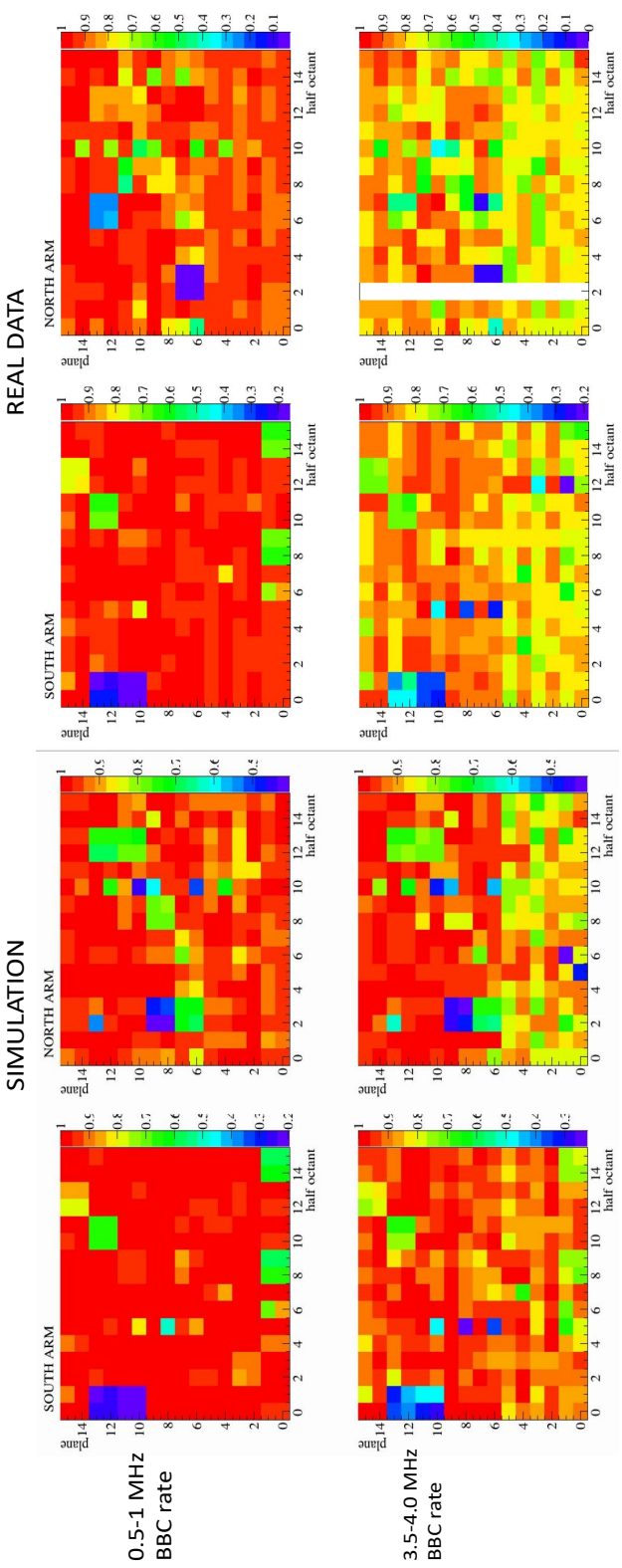

Figure 4.9: Hit Efficiencies for the South arm (left) and North arm (right) for low luminosity (top) and high luminosity from simulation (left) and data (right). The y-axes are planes, and the x-axes are half-octants. The blue areas represent dead areas, and the green and white areas indicate dead or poorly performing planes or half octants for that run. After the implementation of the luminosity dependent MuTr efficiencies, the hit efficiency better represents the effects of pile-up in the MuTr.

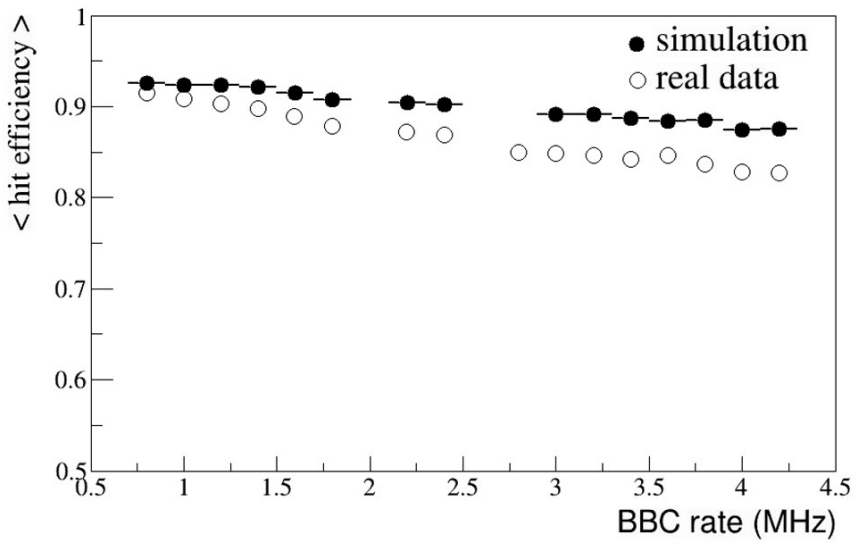

Figure 4.10: Hit efficiency for simulation (filled circles) and real data (open circles) as a function of BBC rate, after the luminosity dependent hit efficiencies were applied. The simulation now shows a change in MuTr hit efficiency as the event rate increases. Differences between simulation and data after the application of the hit efficiency correction indicates that corrections were not calculated or applied perfectly.

The simulation was then run through the new reconstruction framework and then a new ϕ distribution was produced representing the hits in station three of the MuTr as a function of ϕ around the beamline, see Figure 4.11. The simulated ϕ distribution is a much better match to the data than the distribution made prior to correcting for pile-up in the MuTr, see Figure 4.6. There were a couple of half octants where the MuTr hit efficiencies were not correctly implemented, and those half octants show poor matching between simulation and data. In the North arm, in simulation and data, a fiducial selection was made to remove the dead half octant from calculation of all cross section parameters.

As discussed previously, muon analyses in PHENIX utilizing simulations for the 2013 dataset have been compromised by the inability to match simulation and data,

which has led to very large systematic errors in preliminary analyses. This study of the luminosity dependence of the MuTr efficiency now provides the necessary corrections to all muon simulations for the 2013 dataset. The methodology of this study will also be applied to later datasets which also have issues with detector pile-up and decreased efficiency caused by multiple collisions.

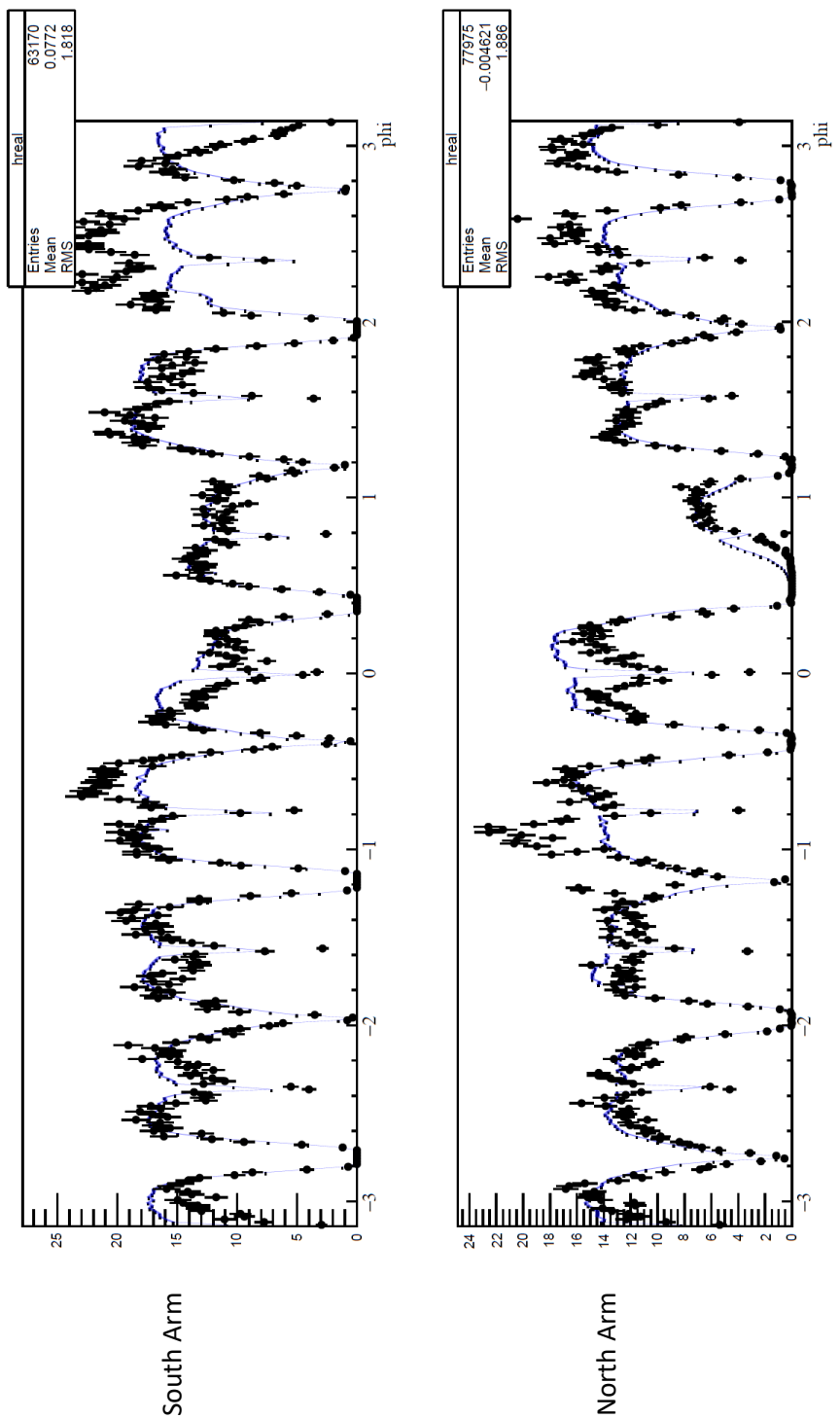

Figure 4.11: ϕ distribution for South (top) and North (bottom) arms comparing data (black) to simulation (blue). After applying the MuTr luminosity dependent hit efficiencies, the distributions are much better matched. Some octants did not have the MuTr efficiencies properly applied, so they are more poorly matched between simulation and data. A fiducial selection was made in the North Arm for $0.3 < \phi < 1.2$ in both the data and and simulation for calculation of cross section parameters.

4.5.1 Acceptance Times Reconstruction Efficiency

After the confirmation of the matching between simulation and data, the simulation can then be used to calculate the detector acceptance times the reconstruction efficiency, and the muon trigger efficiency. All muon track candidates must satisfy the event quality cuts discussed in section 4.1.2 to be considered.

The detector acceptance is defined as the number of J/ψ's that were accepted into either the North arm or South arm rapidity regions, divided by the number thrown into that region. Examples of detector acceptance are seen in Figures 4.12 through 4.17.

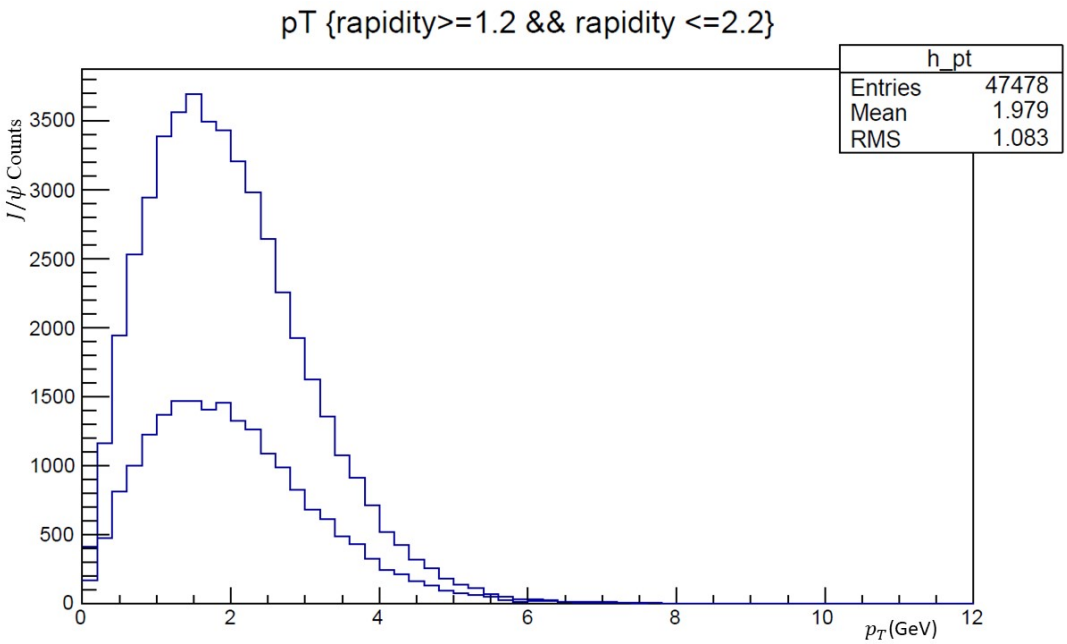

Figure 4.12: Thrown J/ψ's in the North arm as a function of transverse momentum (top curve), and accepted J/ψ's (bottom curve).

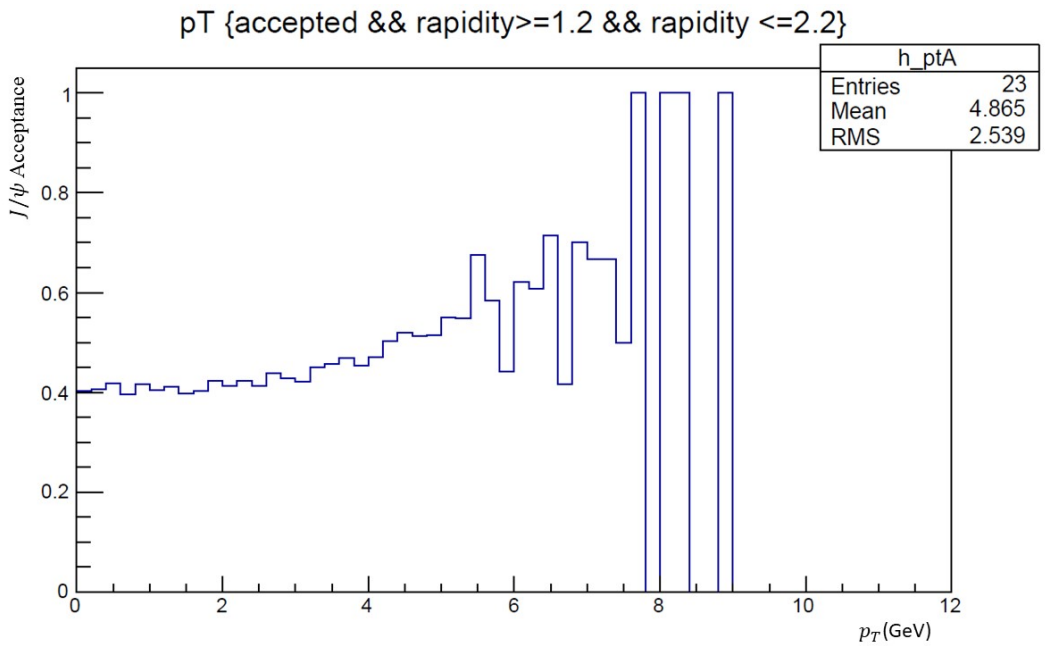

Figure 4.13: The ratio of accepted J/ψ's into the North Muon arm to the thrown J/ψ's as a function of transverse momentum.

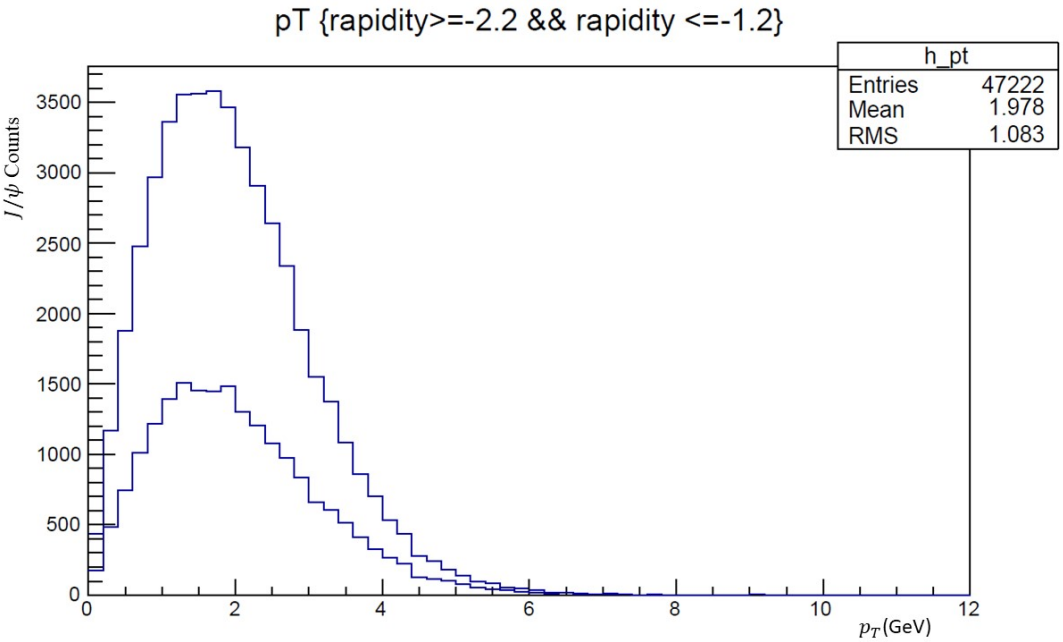

Figure 4.14: Thrown J/ψ's in the South arm as a function of transverse momentum (top curve), and accepted J/ψ's (bottom curve).

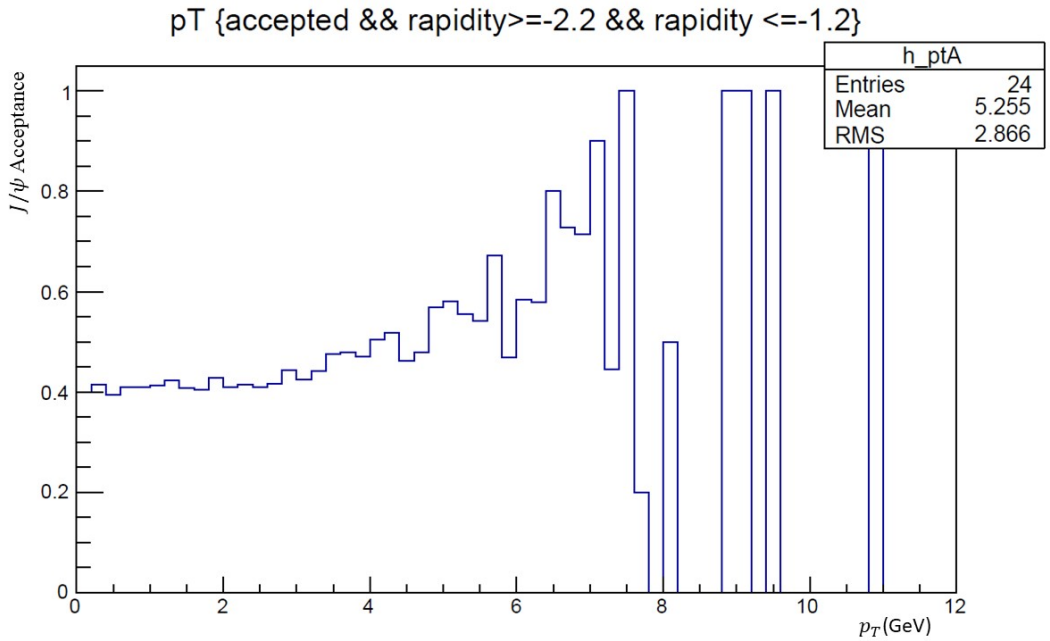

Figure 4.15: The ratio of accepted J/ψ's into the South Muon arm to the thrown J/ψ's as a function of transverse momentum.

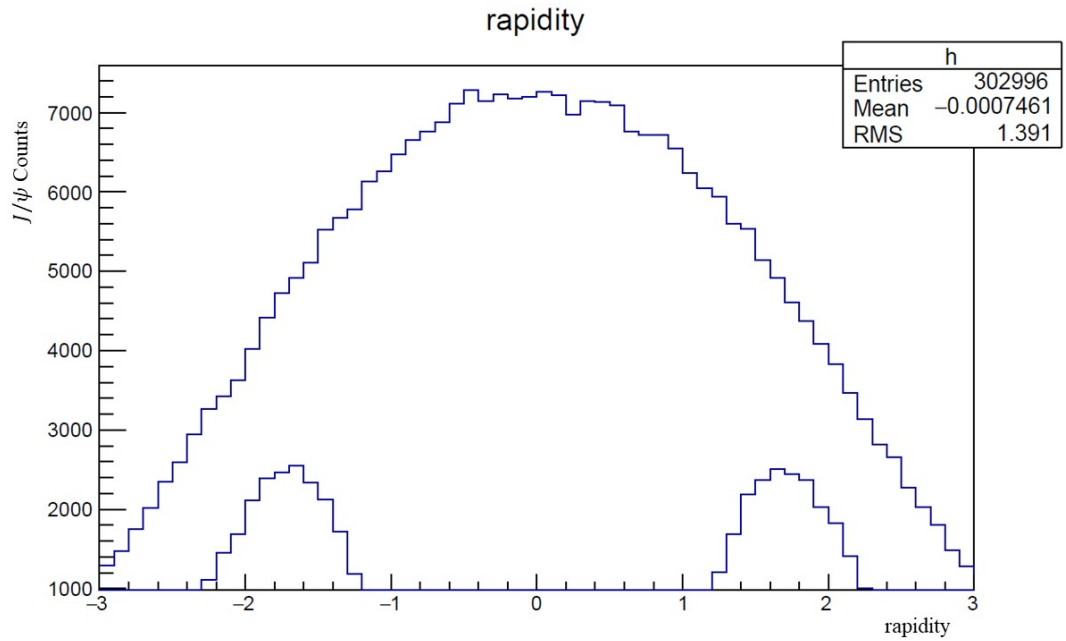

Figure 4.16: Thrown J/ψ's in the North and South Muon arm as a function of rapidity (top curve), and accepted J/ψ's (bottom curve).

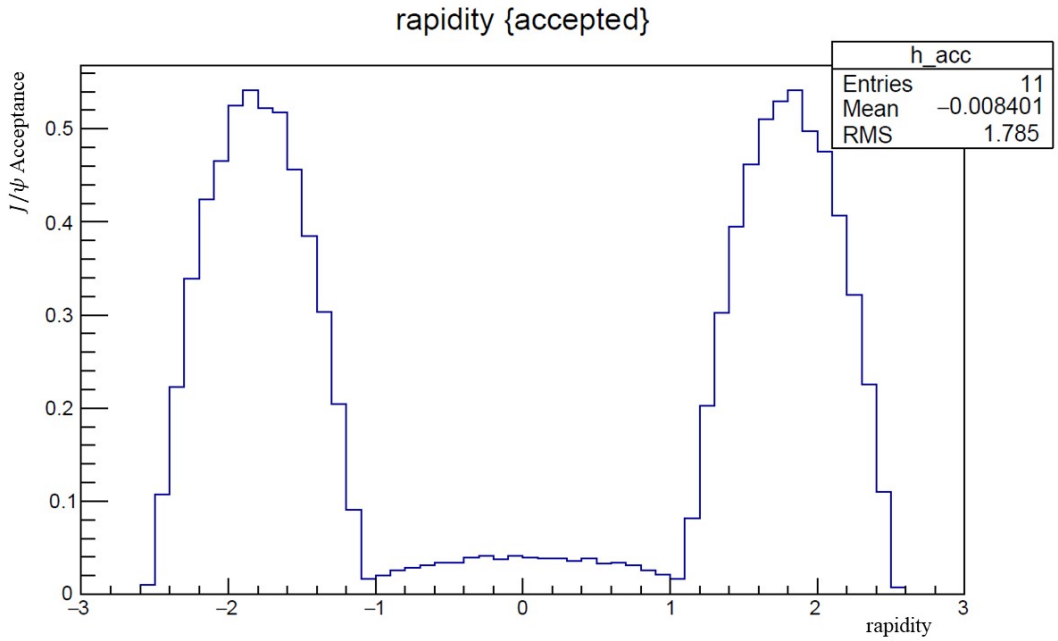

Figure 4.17: The ratio of accepted J/ψ's into the North and South Muon arm to the thrown J/ψ's as a function of rapidity. The accepted J/ψ's at central rapidity indicate one muon of the J/ψ was accepted to the North Arm, and one muon was accepted by the South arm.

The reconstruction efficiency is defined to be the number of J/ψ's that were reconstructed in a particular kinematic bin versus the number that were thrown and accepted by the detector in that kinematic bin. Therefore, $A\epsilon_{reco}$ is defined as the number of J/ψ's detected divided by the number of J/ψ's thrown in that kinematic bin[104]. The acceptance times the reconstruction efficiency is calculated from simulation as:

$$A\epsilon_{reco} = \frac{N_{det}^{J/\psi}(y, p_T)}{N_{prod}^{J/\psi}(y, p_T)}. \tag{4.16}$$

Acceptance and reconstruction efficiency is calculated for all transverse momentum and rapidity bins used for data processing, see Figures 4.18, 4.19, and 4.20. The values are listed in Table 4.3. These values are corrected for each kinematic bin for the track quality cut on the event vertex. The selection criteria for $|z| \leq 30$ cm only

selects from 64% of the J/ψ's thrown, so this percentage is applied as a correction by dividing each value by this percentage.

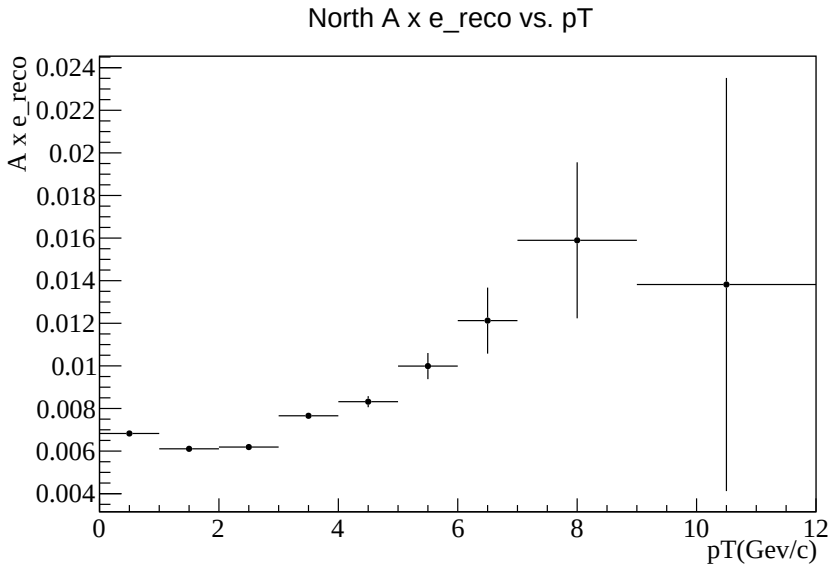

Figure 4.18: $A\epsilon_{reco}$ as a function of transverse momentum for the North arm.

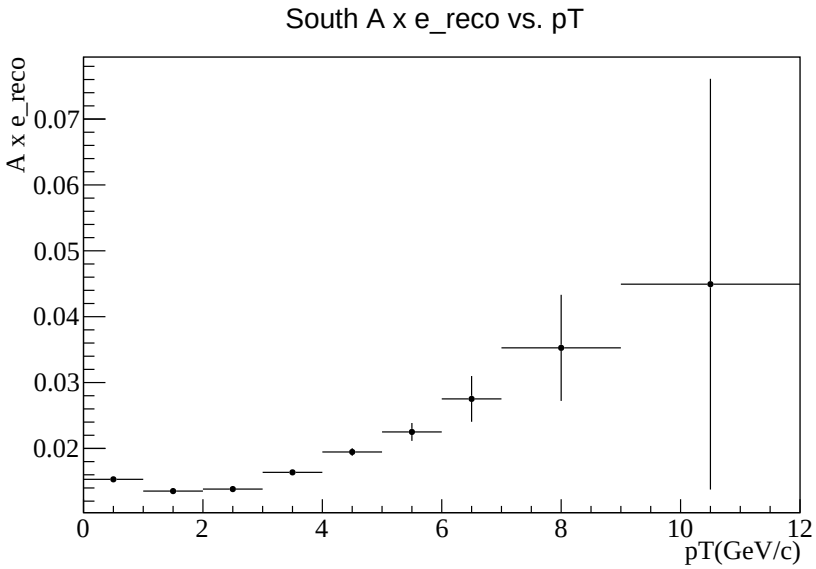

Figure 4.19: $A\epsilon_{reco}$ as a function of transverse momentum for the South arm.

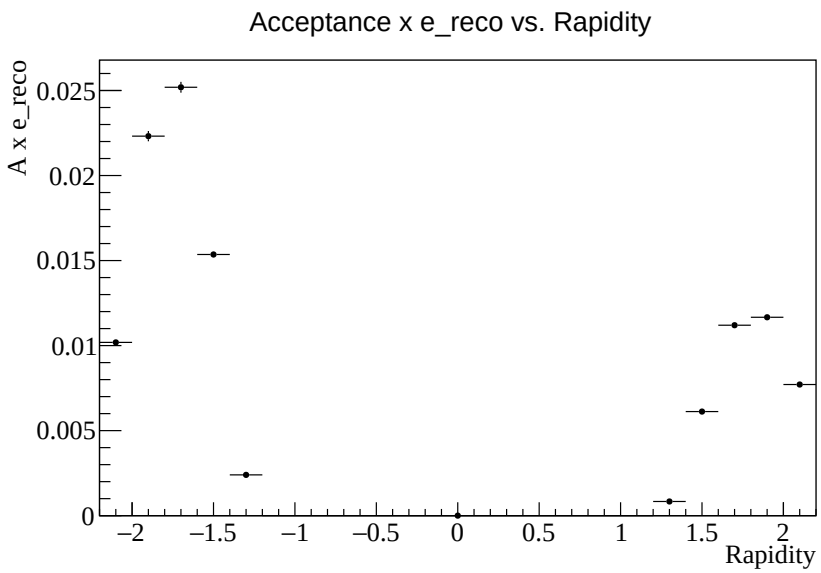

Figure 4.20: $A\epsilon_{reco}$ as a function of rapidity. The South arm values are from $-2.2 \leq y \leq -1.2$ and the North arm values are from $1.2 \leq y \leq 2.2$.

4.6 Muon Trigger Efficiency

The invariant yield of J/ψ mesons includes a correction for the efficiency of the trigger used during data acquisition. The trigger used in the muon arms to indicate a possible J/ψ candidate is the ((MUIDLL1 N2D||S2D)||(N1D& S1D))& BBCLL1(noVtx) or MuID2D trigger, which means that there must be two track candidates that pass through four panels of the MuID in one arm from the same event and also trigger the BBC wide trigger. A track that passes through the fourth panel of the MuID is a muon track candidate, as the steel absorbers after the central magnet and in between the panels of the MuID serve to absorb and thus reject hadronic background. The trigger efficiency is defined as the ratio of dimuons that satisfy the MuID2D trigger bits to all dimuons that satisfy the Minimum Bias trigger. For this analysis the trigger efficiency is extracted from the trigger emulator in simulation, which represents the data well, and has the same requirements on tracks for triggering. The same event

quality cuts are placed on simulated tracks as collision data tracks for this calculation.

The trigger efficiency is calculated for the North and South arms by counting the number of MuID2D triggered events, then dividing the sum by the total number of Monte Carlo generated events in that particular kinematic bin and is defined as

$$\epsilon_{trig} = \frac{\#\text{MuID2D}}{\#\text{MC}}. \tag{4.17}$$

This ratio is then plotted as distributions in transverse momentum, see Figure 4.22 and rapidity, see Figure 4.21. The trigger efficiency distributions are then fit to exponential functions of the form

$$\epsilon_{\text{trig}} = \frac{A}{1 + \exp^{\frac{(x-B)}{C}}} \tag{4.18}$$

where A, B, and C are free fit parameters. The fit values are then extracted for the particular kinematic bin. The trigger requires a minimum slope of a road in the MuID, so for low transverse momentum, muon tracks will not trigger the MuID 2D trigger, due to the trigger logic and allowable combinations of hit patterns in the trigger lookup table. This explains the lower efficiency of the trigger at low transverse momentum and the shape of the curve.

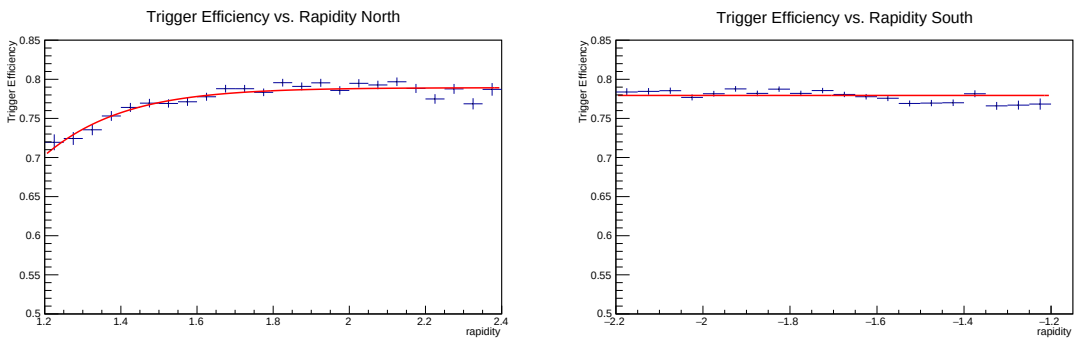

Figure 4.21: Trigger efficiency vs. rapidity for North (left) and South (right) Arms.

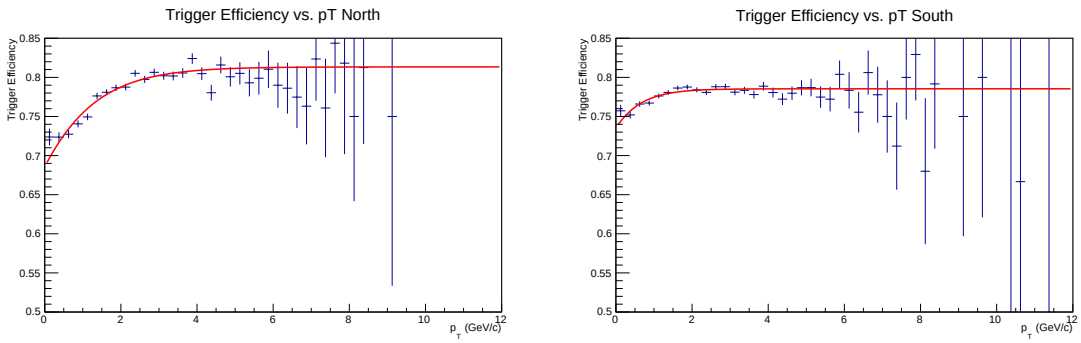

Figure 4.22: Trigger efficiency vs. transverse momentum for North (left) and South (right) Arms.

4.7 Luminosity Normalization

As a normalization to the invariant yield for the cross section measurement, the integrated luminosity is measured including corrections for bunch crossings with multiple collisions and detector pile-up. The luminosity measurement with the pile-up correction has been completed for the W analysis[100, 101, 102] and follows a similar procedure.

The BBCs are the luminosity monitors for PHENIX. When a collision happens between the North and South BBCs in a single beam clock cycle, there are four possible outcomes. Both the North and South BBCs can register hit, only the North or South BBC can register hit, or neither BBC can be hit. If a hit is detected in both the North and South BBCs, the BBC will reconstruct a collision vertex. When there are multiple collisions per bunch crossing, and both BBCs read hits, the BBCs can either under or over count the number of collisions for that bunch crossing. If both collisions produce particle tracks that hit both BBCs, the BBCs will reconstruct only one vertex, so the number of events will be undercounted. If two collisions happen in between the North and South BBCs, and one collision produces

a track that hits only the North Arm, and the other collision produces a track that only hits the South arm, the BBC will overcount the number of interactions producing measurable vertices. These situations signify that the North and South BBCs operate at efficiencies $\leq 100\%$, k_N and k_S, and as a consequence contribute to the miscounting of events. Run 13 has a non-negligible effect from multiple collisions, see Figure 4.24.

Rather than calculating the efficiencies for each possible number of collisions per bunch crossing, the probability for not counting any collision is calculated. An iterative process is used to find the North and South efficiencies based upon the true number of collisions per bunch crossing μ.

$$R_{BBC} = 1 - e^{-\mu\epsilon_{BBC}(1+k_N)} - e^{-\mu\epsilon_{BBC}(1+k_S)} + e^{-\mu\epsilon_{BBC}(1+k_N+k_S)} \tag{4.19}$$

where R_{BBC} is the observed number of collisions per bunch crossing, and ϵ_{BBC} is the BBC efficiency, or the ratio of how many events trigger the BBC to the number of events that occur. For the 2013 data set, ϵ_{BBC} was measured to be 0.53.

Further discussion on the effects of multiple collisions is in the next section. The total integrated luminosity is measured as

$$\mathcal{L}_{int} = \sum_{run} \left(t_{run} \times \mu \times f_{coll}\right) / \left(\sigma_{pp,total}\right) \tag{4.20}$$

where t_{run} is the duration of a run, μ is the true (mean) collision rate per bunch crossing and f_{coll} is the collision frequency, which is $1/(106e^{-9})$[69, 70]. The BBC livetime and the effective number of bunches that actually contribute to collision events must be considered. Not all buckets, or possible bunch places, in the beam are filled, as there is a series of unfilled bunches for the abort gap in order to safely dump the beam at the end of a fill. For Run 13, there are 109 filled collision bunches out of a possible 120. These corrections were also included in the μ calculation. Figure 4.23

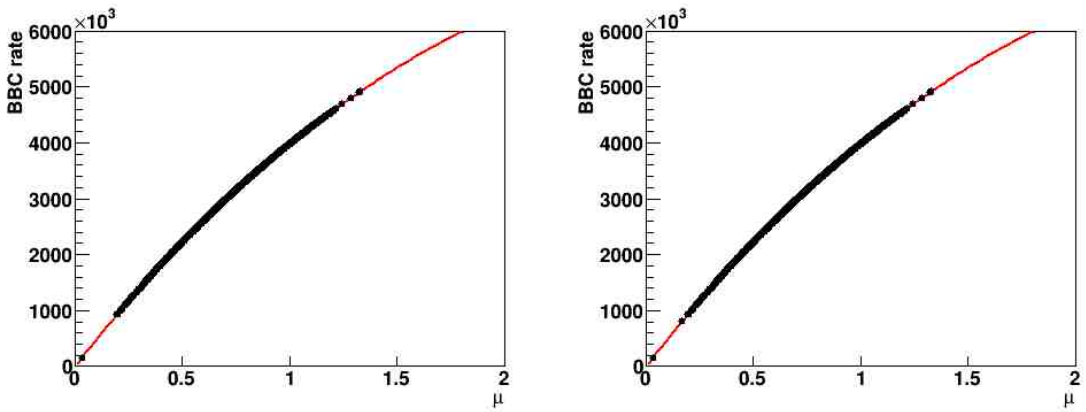

Figure 4.23: BBC rate as a function of the number of collisions per bunch crossing, μ, for the North (left), and South (right) arms.

demonstrates the relationship between the true collision rate and μ with the effective bunch correction. Figure 4.24 shows the number of collisions per minimum bias triggered event as a function of BBC rate, and demonstrates the significance of consideration for multiple collisions in the luminosity calculation. Some runs in the 2013 data set had a scale factor placed on the MuID2D trigger, see Appendix E. This scale factor, SF, divides the number of events processed by the DAQ by $(SF + 1)$. This means that if the scale factor is 1, the DAQ will process every other event. A scaled trigger means that the number of events recorded will be smaller than the number of events that actually occurred. To correct for this, the luminosity for a particular run is scaled by $(SF + 1)$.

With the effective bunch correction, the total integrated luminosity becomes

$$\mathcal{L}_{int} = \sum_{run} \left((SF + 1) \times t_{run} \times \mu_{eff} \times f_{coll} \times (109/120) \times l_{BBC} \right) / \left(\sigma_{pp,total} \right) \quad (4.21)$$

where l_{BBC} is the fraction of time during a run where the BBC is live and not busy.

The total luminosity from Run 13 that was measured by the BBC for the North arm is 257.331pb^{-1} for the total vertex region, and 136.542pb^{-1} for collisions between

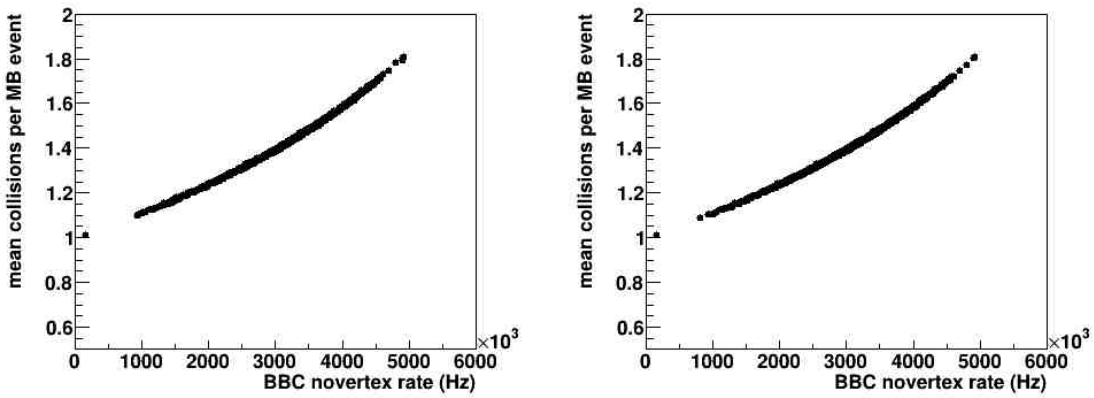

Figure 4.24: The number of collisions per Minimum Bias triggered event for the North (left), and South (right) arms. The BBC novertex trigger is the minimum bias trigger with no on-line vertex cut.

$z = \pm 30$ cm. The total luminosity from Run 13 measured by the BBC for the South arm is 259.591pb^{-1} for the total vertex region, and 137.741pb^{-1} for collisions between $z = \pm 30$ cm. These sampled luminosities take into account the run quality analysis described in Section 4.1.1, and only include runs that passed the run quality cuts,

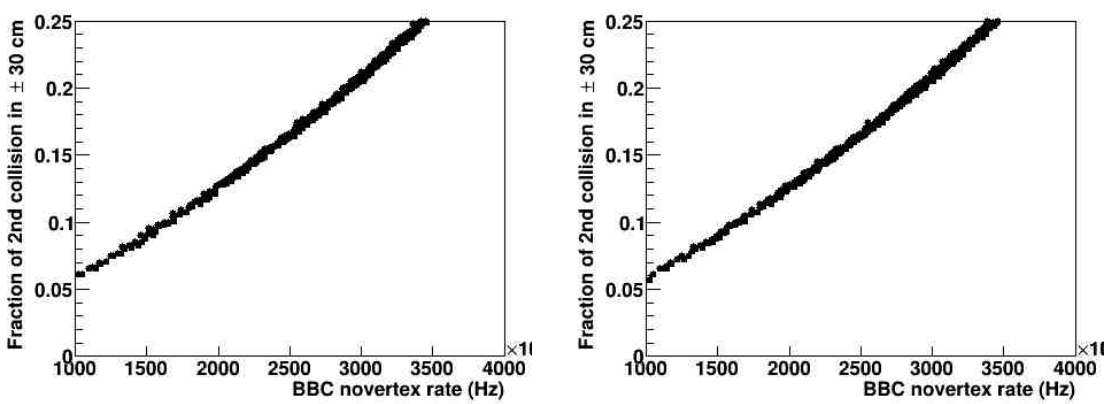

Figure 4.25: The fraction of second collisions within the $z = \pm 30$ cm vertex cut region for the North (left), and South (right) arms.

see Appendix C. Due to the $z = \pm 30$ cm vertex cut placed on the entire data set and simulation, the luminosity used in this analysis is from events that took place within $z = \pm 30$ cm, see Figure 4.25.

4.8 Further Corrections for Multiple Collisions

Typically, the beam luminosity is tuned so that there is an average of one collision per Minimum Bias event. The Run 13 dataset is unique in that the number collisions per Minimum bias event is greater than one, see Figure 4.24. Multiple collisions have a number of consequences for the detectors and Muon trigger used in this analysis.

One effect is the pile-up correction on the BBC, discussed in the previous section, which directly affects the luminosity measurement. The other trigger affected for this measurement is the MuID2D trigger whose rate decreases due to pile-up in the detector. This is true for all types of muon triggers using the MuID. The MuID is constructed of panels of Iarrocci tubes that have an applied bias, and are coupled resistively. When there are multiple collisions in a beam crossing, and more than one muon passes through the same tube of MuID within a beam clock, the current through the tubes becomes too great which causes the bias to sag, which prevents muon candidates from satisfying trigger threshold requirements. Thus, as the number of collisions per bunch crossing increases, the trigger efficiency decreases. The minimum bias event rate is used as a proxy for multiple collisions, see Figure 4.26, the effects of which are examined on the MuID2D trigger efficiency with respect to momentum. Across the range of minimum bias event rates observed in Run 13, about 0.5 to 4.5MHz, the MuID2D trigger efficiency decreases by about 15% in both the North and South Arms.

To correct for the effect from multiple collisions, the luminosity weighted trigger efficiency is compared to the unweighted trigger efficiency. The ratio of the

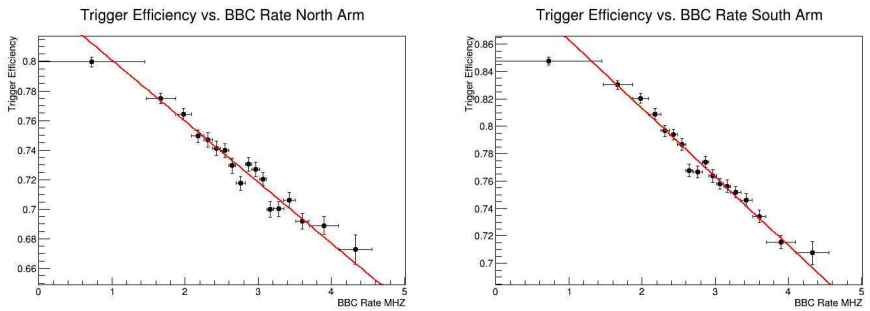

Figure 4.26: MuID2D trigger efficiency as a function of BBC event rate For the North (left) and South (right) muon spectrometers. The BBC event rate is a proxy for the luminosity. The MuID2D trigger efficiency decreases by approximately 15% as the event rate increases.

plateau of the luminosity weighted distribution to the unweighted distribution gives the correction factor. The correction applied by multiplication to the unweighted distributions is 0.885 for the North arm. For the South arm, the correction applied to the unweighted distribution 0.966.

For the simulation, the MuID efficiencies applied to the reconstruction algorithm are averaged over the entire run period. The averaging of the efficiencies then smooths the effects of multiple collisions on the reconstruction, assuming that no other effects have a luminosity dependence, or have otherwise been accounted for. The MuTr efficiency study also applies luminosity dependent hit efficiency information to the tracking algorithm. Therefore, $A\epsilon_{reco}$ does not require further corrections for multiple collisions.

4.9 Error Analysis

In addition to the statistical uncertainties that come from a limited number of dimuons in a particular kinematic bin, there are several sources of systematic un-

certainty in this measurement. In PHENIX analyses, there are three categories of systematic uncertainties. Type A uncertainties are uncorrelated point-to-point variations. Type B uncertainties are correlated between points. Type C uncertainties are global variations which will scale an entire distribution by a fixed percentage. Systematic uncertainties are due to detector limitations, and analysis methodology.

Calculation of systematic errors from the fitting procedure consists of computing the difference between a direct yield count from the background subtracted unlike-sign dimuon mass spectrum, and the yield extracted from the fit. For a fair comparison, the yields are extracted within the J/ψ mass range (2.8-3.4). The difference is then divided by the width of the J/ψ mass range. For the North and South arms, the systematic errors on the fitting procedure for the J/ψ yield are 1.5% for p_T kinematic bins, and 1% for rapidity bins. This is a Type A uncertainty.

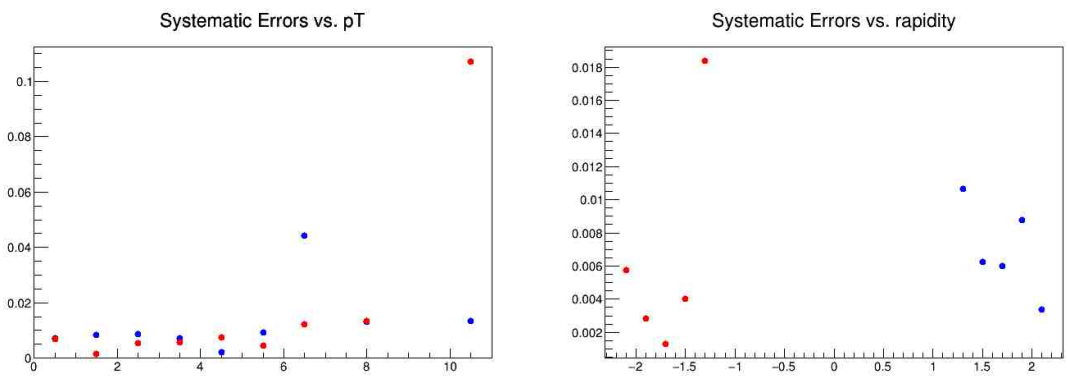

Figure 4.27: The systematic errors from the fitting procedure as a function of p_T (left) and rapidity (right). The North Arm systematic errors are in blue, and the South Arm systematic errors are in red.

Systematic error calculation for the background continuum fitting procedure was performed by examining differences in J/ψ yield between the exponential function and a power-law fit function used in the total fit function. The average difference in yield was 6%, which is a Type A uncertainty.

The systematic uncertainty from changing the normalization of the mixed event background is found by examining the change in yield with changes in the normalization factor. The change in the yield is much smaller than the statistical error, and the difference is random. Mixed-events were normalized from 2-3 GeV mass range for higher statistics. so we assign statistical error of 0% for the mixed-event fitting.

A toy Monte Carlo was performed for the determination of the systematic uncertainty in $A\epsilon_{reco}$ and is based upon differences in the ϕ distribution between simulation and data. A random ϕ range was chosen for the normalization between simulation and real data. Then one hundred pairs of numbers were generated to represent the ϕ of each muon in a muon pair. The probability of each muon to be detected is calculated for the chosen ϕ range. Then the number of how many pairs have both muons accepted is counted using the ϕ distribution for simulation and real data. Ten accepted pairs are accumulated for each random ϕ range. Then the mean and standard deviation acceptance is calculated out of the ten tries. In the North arm, the mean is 5.1% with a RMS error of 0.8%, making the systematic uncertainty 5.9%. In the South arm, where the data is not as well matched to simulation, the average is 7.5% and the RMS uncertainty is 1.7% making the systematic uncertainty 9.2%. It should be noted that the MuTr and MuID efficiency systematic uncertainties are included in this toy Monte Carlo. An additional MuID and MuTr efficiency systematic would essentially double count the systematic uncertainties for these parameters. This represents a Type B uncertainty.

The resulting difference in the North and South arms in invariant yield due to the correction from $A\epsilon_{reco}$ is another source of systematic error. For every kinematic bin, the error is calculated by $\frac{\Delta N^{J/\psi}}{\sqrt{12}}$. For low transverse momentum, this difference is low, and it increases as transverse momentum increases.

The systematic error for the trigger efficiency is calculated by measuring the difference between the fit function and the trigger efficiency value for a particular

kinematic bin. The average systematic uncertainty is 1% for both North and South Arms for all kinematic bins. This is a Type B uncertainty.

The systematic error to the integrated luminosity lies in the limitations of the Vernier Scan analysis, see next chapter. Corrections for the hourglass effect and $\beta*$ focusing parameter are poorly constrained, which results in the minimum bias cross section, σ_{BBC} having a systematic error of 10%. Therefore the integrated luminosity is assigned a systematic error is 10%. This is a Type C error and is applied as a global error on the final value of the cross section.

Type A errors are added in quadrature to statistical errors to account for the quoted statistical error. Type B errors are added in quadrature with each other as systematic uncertainties. Type C error is added as an additional error to the final value.

Type	Source	Error
A	Yield Extraction	1.5% (p_T) 1% (y)
A	Background Fitting	6%
B	$A\epsilon_{reco}$	$5.1\% \pm 0.8\%$(S) $7.5\% \pm 1.7\%$ (N)
B	$\Delta N^{J/\psi}$	1%-10%
B	ϵ_{trig}	1%
C	Luminosity	10%

Table 4.3: Systematic errors and their associated types.

4.10 Results

Results for the fitting procedure and correction factors are given in Tables 4.4 and 4.5 for each kinematic bin in transverse momentum and rapidity. The uncorrected

J/ψ yield used in the cross section calculation is taken from the fit of the J/ψ peak with the Crystal Ball function for the entire range of the spectrum, $2-5$ GeV. The correction factors accounting for the acceptance times the reconstruction efficiency, $A\epsilon_{\rm reco}$, and the trigger efficiency, $\epsilon_{\rm trig}$, are both calculated from the simulation as described previously. The range gives the kinematic bin of interest. For transverse momentum bins, rapidity is integrated for the entirety of the arm range, and vice versa.

$N_{J/\psi}^{\rm uncorr}$	$A\epsilon_{\rm reco}$	$\epsilon_{\rm trig}$	Range
20441±213	0.0153±2.07E-4	0.717	$0 \le p_T < 1$
31202±258	0.0135±1.33E-4	0.734	$1 \le p_T < 2$
19003±199	0.0138±1.57E-4	0.738	$2 \le p_T < 3$
10293±146	0.0164±2.77E-4	0.739	$3 \le p_T < 4$
4614±78	0.0194±5.89E-4	0.739	$4 \le p_T < 5$
1965±51	0.0225±1.36E-3	0.739	$5 \le p_T < 6$
850±34	0.0275±3.47E-3	0.739	$6 \le p_T < 7$
540±28	0.0353±8.05E-3	0.739	$7 \le p_T < 9$
87±13	0.0445±3.12E-2	0.739	$9 \le p_T < 12$
6206±113	0.0102±1.61E-4	0.733	$-2.2 \le y < -2.0$
21671±216	0.0223±3.02E-4	0.733	$-2.0 \le y < -1.8$
33823±273	0.0252±3.18E-4	0.733	$-1.8 \le y < -1.6$
26744±240	0.0153±1.91E-4	0.733	$-1.6 \le y < -1.4$
4976±93	0.00240±4.08E-5	0.733	$-1.4 \le y < -1.2$

Table 4.4: South arm results for the raw yield of J/ψ's from the Crystal Ball fit, the detector acceptance times the reconstruction efficiency, the trigger efficiency and the corrected yield for each p_T and rapidity bin used in this analysis.

$N_{J/\psi}^{\text{uncorr}}$	$A\epsilon_{\text{reco}}$	ϵ_{trig}	Range
7637±136	0.00683±9.61E-5	0.642	$0 \leq p_T < 1$
12882±171	0.00611±6.29E-5	0.685	$1 \leq p_T < 2$
8477±133	0.00619±7.39E-5	0.704	$2 \leq p_T < 3$
4565±93	0.00766±1.34E-4	0.714	$3 \leq p_T < 4$
2035±53	0.00832±2.60E-4	0.717	$4 \leq p_T < 5$
885±35	0.00999±6.14E-4	0.719	$5 \leq p_T < 6$
404±24	0.0121±1.55E-3	0.719	$6 \leq p_T < 7$
257±18	0.0159±3.66E-3	0.720	$7 \leq p_T < 9$
49±9	0.0218±9.70E-3	0.720	$9 \leq p_T < 12$
2062±70	8.33E-4±2.03E-5	0.652	$1.2 \leq y < 1.4$
10512±152	0.00612±8.61E-5	0.682	$1.4 \leq y < 1.6$
13264±168	0.0112±1.51E-4	0.692	$1.6 \leq y < 1.8$
8612±141	0.0117±1.67E-4	0.696	$1.8 \leq y < 2.0$
3291±85	0.00771±1.26E-4	0.698	$2.0 \leq y < 2.2$

Table 4.5: North arm results for the raw yield of J/ψ's from the Crystal Ball fit, the detector acceptance times the reconstruction efficiency, the trigger efficiency and the corrected yield for each p_T and rapidity bin used in this analysis.

The invariant cross section of the J/ψ was measured using Equation 4.3 for different kinematic bins in transverse momentum and rapidity. Table 4.6 displays the invariant cross section for integrated rapidity in different kinematic bins for the North arm, and Table 4.7 for the South arm. The results for the invariant cross section for transverse momentum integrated rapidity bins are displayed in Table 4.8. These results do not include the global Type C error from the luminosity normalization. Results are reported as Cross section ± statistical error ± systematic error.

$\frac{B(J/\psi\to\mu^+\mu^-)}{2\pi}\frac{d^2\sigma}{p_T dy dp_T}(nb/(GeV/c)^2)$	Range
$5.628 \pm 0.367 \pm 0.351$	$0 \le p_T < 1$
$3.316 \pm 0.212 \pm 0.199$	$1 \le p_T < 2$
$1.257 \pm 8.17\text{E-}2 \pm 7.71\text{E-}2$	$2 \le p_T < 3$
$0.386 \pm 2.60\text{E-}2 \pm 2.31\text{E-}2$	$3 \le p_T < 4$
$0.123 \pm 9.07\text{E-}3 \pm 7.68\text{E-}3$	$4 \le p_T < 5$
$3.62E-2 \pm 3.47\text{E-}3 \pm 2.23\text{E-}3$	$5 \le p_T < 6$
$1.15E-2 \pm 1.78\text{E-}3 \pm 7.77\text{E-}4$	$6 \le p_T < 7$
$2.27E-3 \pm 5.64\text{E-}4 \pm 1.47\text{E-}4$	$7 \le p_T < 9$
$1.60E-4 \pm 7.78\text{E-}5 \pm 1.21\text{E-}5$	$9 \le p_T < 12$

Table 4.6: The invariant cross section as a function of transverse momentum of the J/ψ in kinematic bins of the North Arm

$\frac{B(J/\psi\to\mu^+\mu^-)}{2\pi}\frac{d^2\sigma}{p_T dy dp_T}(nb/(GeV/c)^2)$	Range
$5.972 \pm 0.383 \pm 0.561$	$0 \le p_T < 1$
$3.362 \pm 0.212 \pm 0.311$	$1 \le p_T < 2$
$1.196 \pm 7.62\text{E-}2 \pm 0.112$	$2 \le p_T < 3$
$0.387 \pm 2.54\text{E-}2 \pm 3.58\text{E-}2$	$3 \le p_T < 4$
$0.115 \pm 8.13\text{E-}3 \pm 1.08\text{E-}2$	$4 \le p_T < 5$
$3.44E-2 \pm 3.11\text{E-}3 \pm 3.23\text{E-}3$	$5 \le p_T < 6$
$1.03E-2 \pm 1.51\text{E-}3 \pm 1.02\text{E-}3$	$6 \le p_T < 7$
$2.07E-3 \pm 5.00\text{E-}4 \pm 2.00\text{E-}4$	$7 \le p_T < 9$
$1.35E-4 \pm 9.68\text{E-}5 \pm 1.45\text{E-}5$	$9 \le p_T < 12$

Table 4.7: The invariant cross section of the J/ψ as a function of transverse momentum in the South Arm.

$B(J/\psi \to \mu^+\mu^-)\frac{d^2\sigma}{dydp_T}(nb/(GeV/c)^2)$	Range
$41.8 \pm 2.73 \pm 4.84$	$-2.2 \leq y < -2.0$
$66.7 \pm 4.21 \pm 7.22$	$-2.0 \leq y < -1.8$
$92.1 \pm 5.77 \pm 8.65$	$-1.8 \leq y < -1.6$
$120.0 \pm 7.53 \pm 11.3$	$-1.6 \leq y < -1.4$
$142.3 \pm 9.37 \pm 19.5$	$-1.4 \leq y < -1.2$
$193.0 \pm 14.2 \pm 18.5$	$1.2 \leq y < 1.4$
$128.0 \pm 8.20 \pm 7.92$	$1.4 \leq y < 1.6$
$86.8 \pm 5.52 \pm 5.39$	$1.6 \leq y < 1.8$
$53.7 \pm 3.47 \pm 4.94$	$1.8 \leq y < 2.0$
$31.1 \pm 2.11 \pm 3.43$	$2.0 \leq y < 2.2$

Table 4.8: The invariant cross section of the J/ψ as a function of rapidity in the South and North Arms.

Distributions of the invariant differential cross sections are shown as a function of transverse momentum in Figure 4.28 for the North and South arms, representing independent measurements. The average differential cross section between the North and South arms as a function of transverse momentum is shown in Figure 4.29. The differential cross section as a function of rapidity is shown in Figure 4.31.

For wide transverse momentum bins, the mean value of the transverse momentum in not necessarily in the center of the bin. The transverse momentum distribution was then fit with the function

$$f(x) = \frac{A}{(1 + \left(\frac{x}{B}\right)^2)^C},$$

where A, B, and C are fit parameters, to find the mean value of each transverse momentum bin [105]. The position of the invariant cross section values in each bin was then shifted to reflect the mean value. For low transverse momentum bins, the mean value did not deviate significantly from the median of the bin, but for the two highest transverse momentum bins, the transverse momentum data point for the $7 < p_T < 9$ GeV is placed at 7.67 GeV, and the data point for $9 < p_T < 12$ GeV is placed at 9.9 GeV.

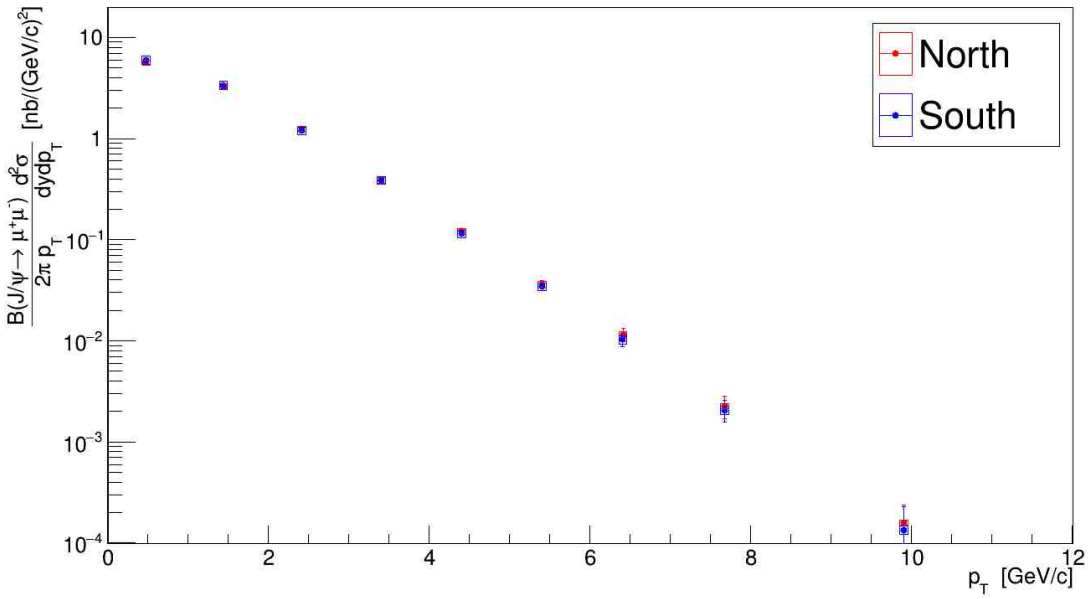

Figure 4.28: Differential J/ψ cross section as a function of transverse momentum for North (red) and South (blue) Arms. The bars on the data points indicate statistical errors, and the boxes indicate systematic errors. Type C errors are not included.

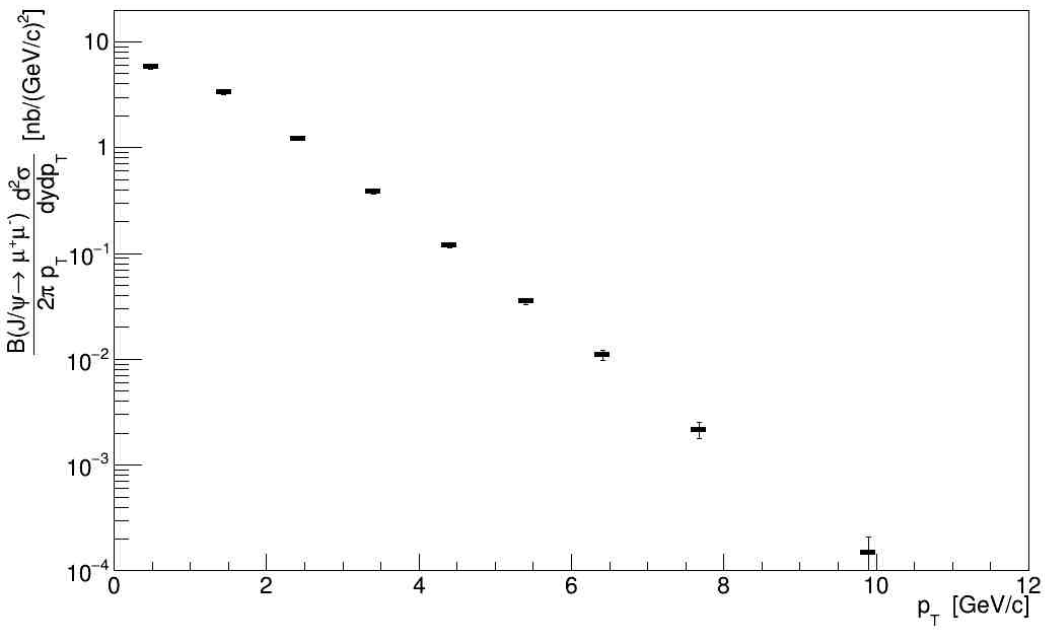

Figure 4.29: Differential J/ψ cross section as a function of transverse momentum for an average of North and South Arms. The bars on the data points indicate statistical errors, and the boxes indicate systematic errors. Type C errors are not included.

The percent difference/100 between the invariant cross sections in the South and North Arms is measured as a comparison of invariant cross section values in each transverse momentum bin in the North and South Arms. The ratio was measured to be less than 0.17 for all transverse momentum bins, see Figure 4.30.

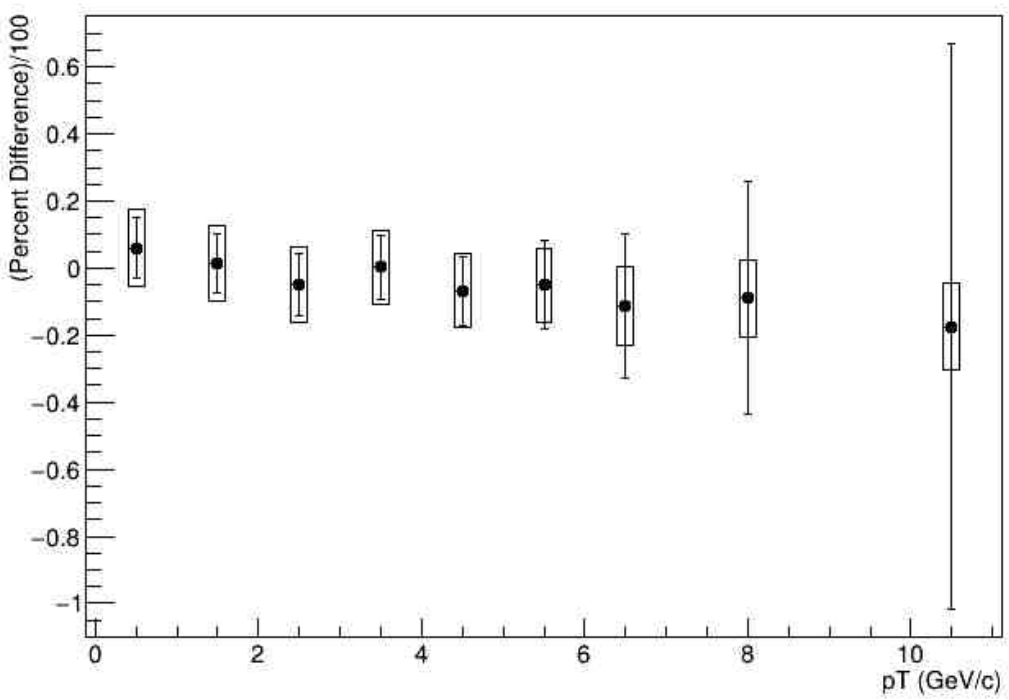

Figure 4.30: Percent difference/100 of the differential cross section between North and South Arms.

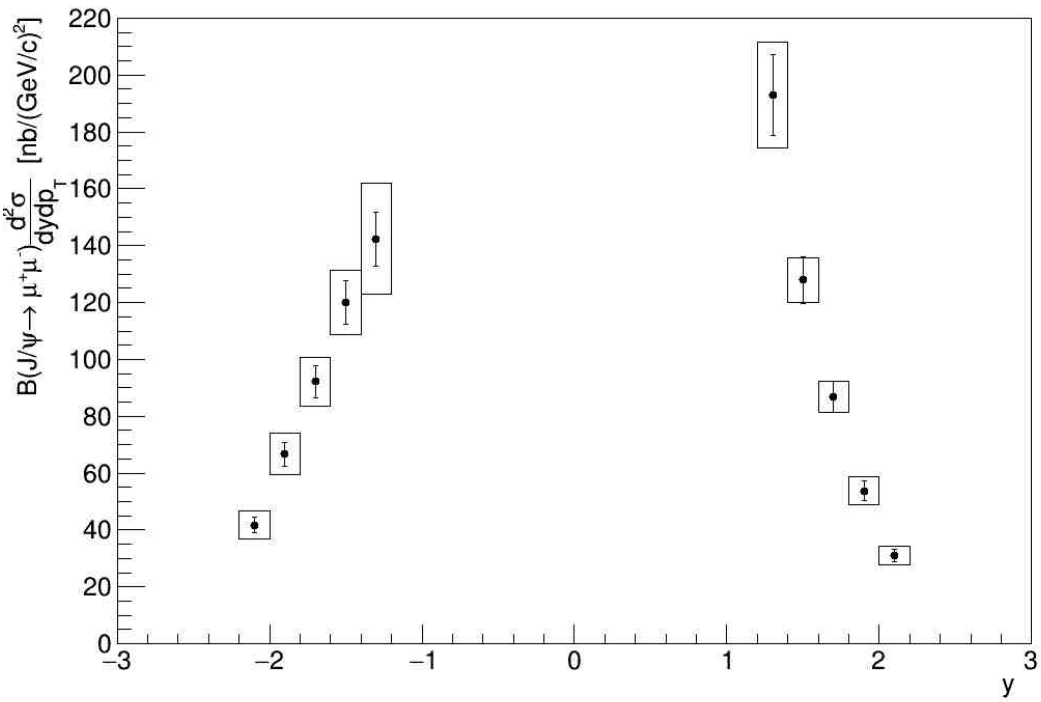

Figure 4.31: Differential J/ψ cross section as a function of rapidity for North and South Arms. The bars on the data points indicate statistical errors, and the boxes indicate systematic errors. Type C errors are not included.

4.11 Comparison to Models

The inclusive differential cross section for the J/ψ as a function of transverse momentum is compared to two separate models, see Figure 4.32. At low transverse momentum, comparison to prompt J/ψ LO+NRQCD coupled to the color glass condensate (CGC) description of gluons with a low momentum fraction of the proton [6] shows good agreement. This prediction was not made for large transverse momentum.

For larger transverse momentum, comparison of the data to NLO+NRQCD cal-

culations [7] shows that the model underpredicts the data. It should be noted that neither model includes non-prompt J/ψ. If the models were to include the non-prompt J/ψ, the cross section predictions would be expected to be higher, and may be expected to flatten the distribution.

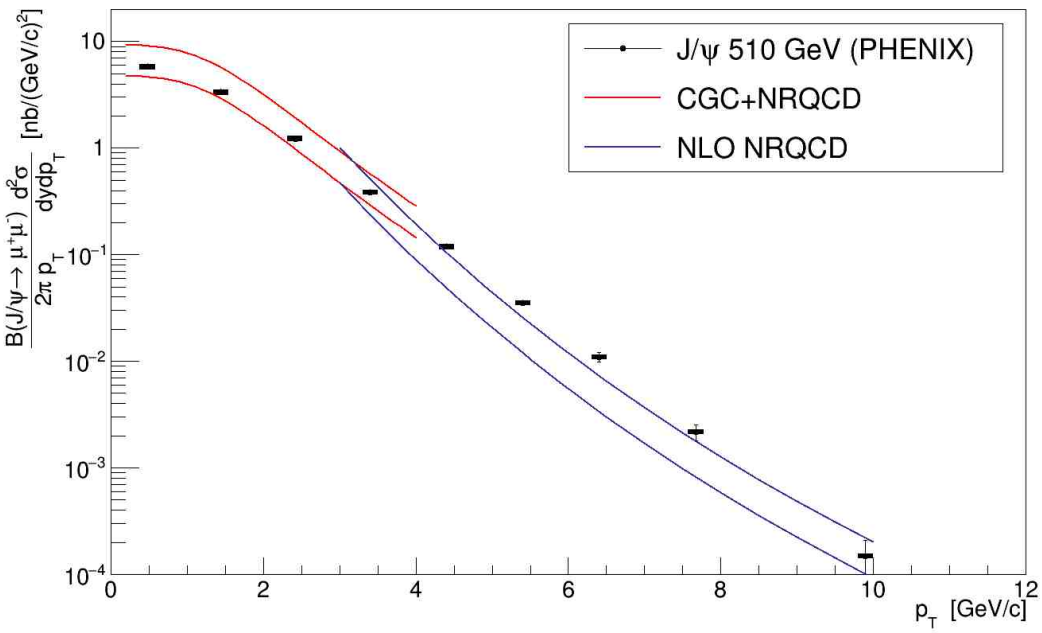

Figure 4.32: Differential J/ψ cross section as a function of transverse momentum for an average of North and South Arms. The average is compared to CGC+NRQCD low transverse momentum predictions (red) [6] and high transverse momentum NLO NRQCD predictions(blue)[7].

Chapter 5

The Vernier Scan

5.1 Luminosity Normalization and Minimum Bias Cross Section

In order to calculate any cross section in a collider experiment, the absolute integrated luminosity during the period for which the events were recorded must be used as a normalization parameter.

This chapter details the Vernier scan technique for determining luminosity, necessary subsystems used for data taking during the Vernier scan, and the steps and considerations for the luminosity calculation. The Vernier Scan Analysis, a collaborative effort[106][107], refers to the Run 15 $p+p$ $\sqrt{s} = 200$GeV data set. The Run 13 analysis used for the cross section calculation in this thesis was completed by Sadeera Bandara of the University of Massachusetts, Amherst. The techniques and analysis methodology of both Run 13 and 15 are similar.

5.2 Overview

The integrated luminosity, L, for a particular process, x, is related to the number of events produced using that process, N_x, and the cross section of that process, σ_x by:

$$N_x = L\sigma_x. \tag{5.1}$$

The Vernier Scan (or Van der Meer Scan) is a technique invented by Simon Van der Meer in 1968[108] to observe the counting rate R in a suitable monitoring system while sweeping the two colliding beams vertically and horizontally through each other. The interaction rate of produced particles observed by such a suitable detector, R_{det}, is defined as the instantaneous luminosity seen by the detector, $\mathcal{L}_{det}$, times cross section σ_{det}[109]:

$$R_{det} = \mathcal{L}_{det}\sigma_{det}. \tag{5.2}$$

For the PHENIX experiment, the beam beam counter (BBC), the minimum bias detector, is used as a luminosity counter. The minimum bias trigger for events occurring within $|z| \approx 30$cm is used for the measurement of σ_{BBC}, the amount of the $p+p$ total cross section as seen by the minimum bias trigger of the BBC. For any physics run at PHENIX, integrated luminosity is then found by the relation,

$$L = \int \mathcal{L}_{det}dt = \frac{N_{MB}}{\sigma_{BBC}} \tag{5.3}$$

where N_{MB} is the number of minimum bias triggered events and σ_{BBC} is the quantity determined by the Vernier Scan technique as

$$\sigma_{BBC} = \frac{R_{BBC}}{\mathcal{L}_{\mathcal{BBC}}}. \tag{5.4}$$

Here, $\mathcal{L}_{BBC}$ is the instantaneous luminosity seen by the minimum bias trigger, and R_{BBC} is the rate of the same BBC trigger. $\mathcal{L}_{BBC}$ is determined by the delivered luminosity, $\mathcal{L}_{delivered}$, and the efficiency of the minimum bias trigger ϵ_{BBC} by

$$\mathcal{L}_{BBC} = \mathcal{L}_{delivered} \times \epsilon_{BBC}. \tag{5.5}$$

The delivered luminosity is calculated from the Vernier Scan analysis as

$$\mathcal{L}_{delivered} = f_0 \sum_{crossings} \frac{N_b N_y}{4\pi\sigma'_x\sigma'_y}, \tag{5.6}$$

where f_0 is the bunch crossing frequency (78kHz), N_b and N_y are the number of protons in the blue and yellow bunches ($\sim 10^{11}$), and σ'_x and σ'_y are the Gaussian widths of the bunches in the transverse dimensions x and y respectively. However, the technique of the Vernier Scan does not allow for the direct values of σ'_x and σ'_y to be measured. Instead, the overlap widths in the vertical and horizontal dimensions are measured, where the overlap width $\sigma_{x(y)} = \sqrt{2} * \sigma'_{x(y)}$. This leads to:

$$\mathcal{L}_{delivered} = f_0 \sum_{crossings} \frac{N_b N_y}{2\pi\sigma_x\sigma_y} \tag{5.7}$$

and the final computed quantity, σ_{BBC},

$$\sigma_{BBC} = \frac{R_{max}}{\mathcal{L}_{BBC}} = \frac{R_{max}}{\epsilon_{BBC}\mathcal{L}_{delivered}} = \frac{R_{max}}{f_0\epsilon_{BBC}} \sum_{crossings} \frac{2\pi\sigma_x\sigma_y}{N_b N_y} \tag{5.8}$$

with R_{max} being the event rate at maximal beam overlap.

5.3 The Vernier Scan Technique

Vernier Scans at PHENIX take place every Run year for the normalization of cross section measurements. The experimental procedure at RHIC for completing a Vernier Scan consists of locally moving one beam across the other in discrete steps of a 100 to 250 microns via changes in the DX magnet currents. Steps are held typically 30-90 seconds with the maximally overlapped steps held for 30 seconds, and the minimally overlapped steps held for 90 seconds. There are 24 steps over the course of a scan. The data taking for the Vernier Scans in Run 15 began with the beams at maximal overlap, then moved them out to minimal overlap before returning them to the maximally overlapped orientation. One beam is moved first horizontally (in x), then

vertically (in y). A summary of all of the Vernier Scans performed for Run 15 $p+p$ data is shown in Table 5.1.

Run	Fill	Comments
424347	18721	Run Control Server Failure
426254	18776	-
431624	18942	Test of Diagonal Scan (Omitted in Analysis)
431723	18943	Diagonal and Horizontal/Vertical Scans
431962	18952	CLOCK Trigger Enabled

Table 5.1: Run 15 $p+p$ Vernier scans and data notes.

The first Vernier Scan in Run 15 experienced a Run Control Server Failure, which resulted from a communication issue between the PHENIX control room and the Collider Accelerator Division (CAD). This server failure happened at the end of the scan and did not affect the data collected for run 424347. A diagonal scan was completed in order to confirm the assumption of a Gaussian bunch distribution in the transverse plane.

A trigger configuration error in the data acquisition occurred in all Vernier scans prior to run 431962. Specifically, these runs did not collect the proper timing information for each bunch crossing in order to calculate the event rate for each step of the Vernier scan. The final scan, Run 431962, had the correct trigger configuration setup, which enabled the event rate calculation necessary to complete a traditional Vernier Scan analysis, and is the only scan used for the final minimum bias trigger cross section.

Vernier scans use a special trigger configuration that is optimized for recording collision data with very low minimum bias event rates, specifically at minimal beam overlap. Additionally, Vernier scans require time dependent data analysis, which is not typically required for other analyses which utilize events characterized by event number. The time dependence is established by the RHIC beam clock via

the PHENIX CLOCK scalars; which increments separate "raw" scalars for all bunch crossings, for each RHIC clock, and for all beam crossings where the data acquitition system is "live." Livetime of the DAQ is then the change in live scalar count over the change in raw scalar count for a certain period of time. Timing information is used in event rate calculation and detector livetime correction. The trigger configuration error did not affect certain aspects of the Vernier Scan analysis, namely the minimum bias trigger efficiency calculation, which does not require timing information.

The bunch intensities, N_b and N_y, are taken from the Wall Current Monitor (WCM) given by induced current readings on an RLC circuit from passing proton bunches. The WCM takes measurements on the order of nanoseconds and can measure the bunch populations for individual bunches and detect debunched protons. The uncertainty of the WCM measurements is approximately 2-3% so the results are normalized to measurements taken from the more accurate Direct Current Current Transformer (DCCT), which has an uncertainty of $\sim 0.02\%$. The DCCT measures induced current in a solenoid around the beam pipe from a time period, t, of approximately 100 seconds before the scan begins. These measurements are completed over a longer period of around a second per measurement and give an average beam intensity. For the i^{th} bunch, the normalized intensity is:

$$N_i = N_{b(y)} \frac{\sum\limits_{t} DCCT}{\sum\limits_{t} \sum\limits_{bunches} WCM}. \tag{5.9}$$

Normalized bunch intensities are typically on the order of 10^{11} protons.

As part of the Vernier Scan data analysis, the efficiency of the minimum bias trigger taken at maximal beam overlap, ϵ_{BBC}, is calculated for every run, as described in section 7.5.1. For Run 15 p+p collisions, BBC efficiencies for the "BBCLL1(>0 tubes)" Minimum Bias trigger range from 0.34 to 0.351.

The Beam Position Monitors (BPMs) are axially split capacitors along the beam pipe about 8m away from the IP and monitor the beam position in the x-y plane. Beam positions plotted as a function of time for Run 424347 are displayed in Figure 5.1. The step position has, in previous years, been taken by using CAD's Beam Position Monitors. The BPMs provide adequate measurements of relative beam positions; however, they are not accurate enough for establishing absolute beam positions [110]. The step positions defined by CAD magnet currents were used instead. Since the step position was not a measured quantity, it had no corrections.

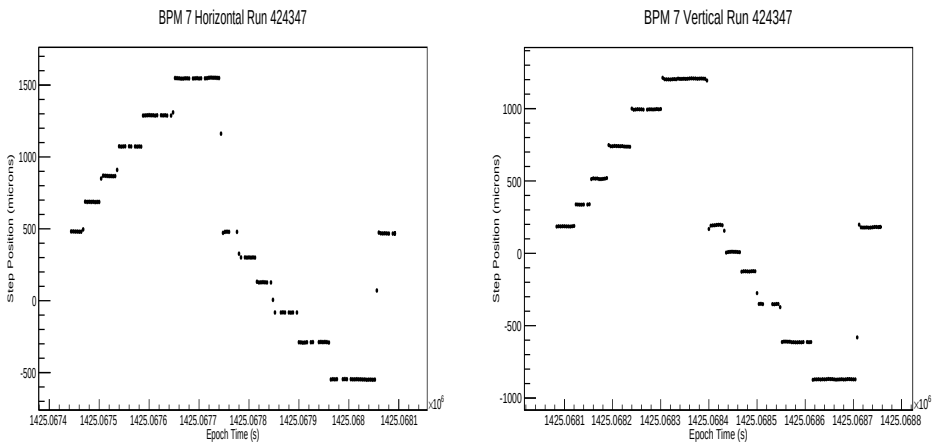

(a) (b)

Figure 5.1: Beam positions in microns for Run 424347 (a) Horizontal (x) (b) Vertical (y) as functions of epoch time. Epoch time starts from January 1st 1970, and is counted in seconds.

Transverse beam profiles, and the overlap widths, σ_x and σ_y, are obtained by fitting the livetime corrected BBC Minimum Bias triggered event rate vs. BPM step positions with a Gaussian function and extracting the fitted widths, see Figures 5.2 and 5.3. This is completed for each bunch crossings for both the horizontal and vertical scans. Two dimensional profiles are fit with the product of two Gaussian functions each in x and in y, see Figure 5.4, where the fit parameters represent the same quantities as in the one dimensional case. The differences in the maximal event

rate and overlap widths between the one dimensional fit and the two dimensional fit are $\sim 1\%$. The two dimensional fit is considered more robust because the beam may not return to the exact same maximal overlap position in later steps during the scan. Overlap widths have nominal values of 250-270 μm. The maximally overlapped event rate R_{max} is extracted from the peak of the Gaussian fit function to the BBC event rate vs. beam position plot. Typical maximally overlapped event rates for each bunch crossing are 4500-7000Hz. A value of σ_{BBC} is computed, using Equation 5.8 for each of the bunch crossing for all the Vernier Scans for Run 15 p+p 200 GeV and bunch averaged, giving the final value and a statistical rms error.

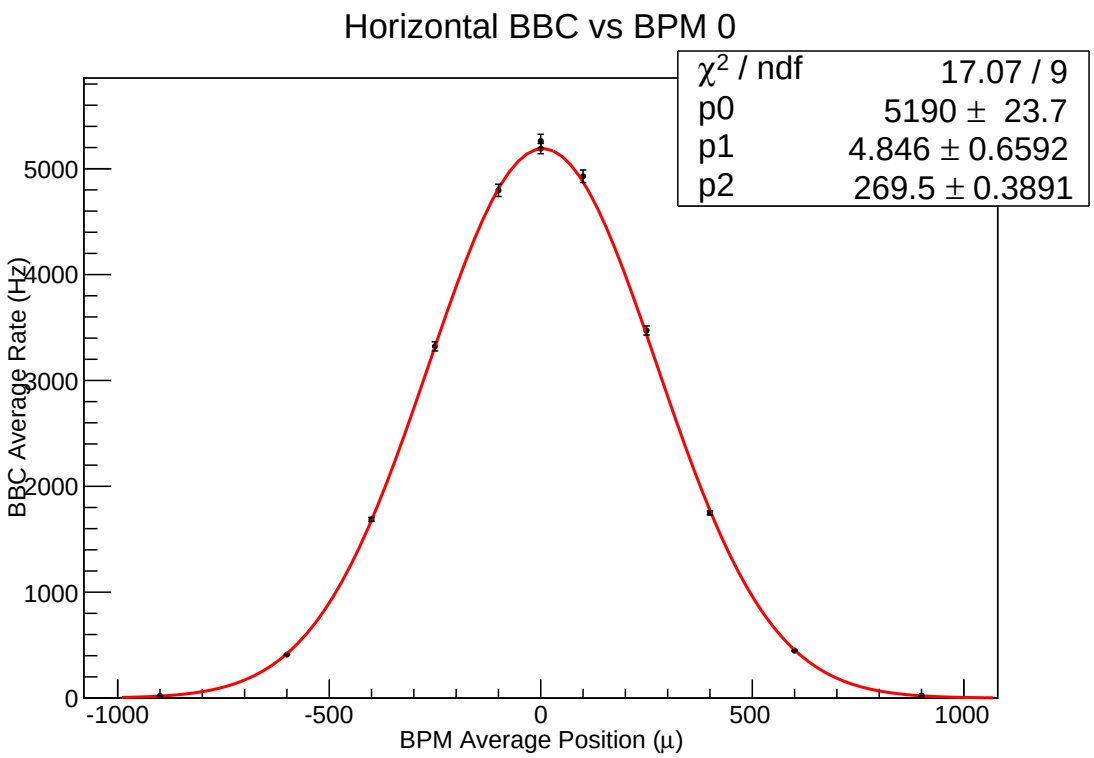

Figure 5.2: Run 431962 Horizontal Profile with livetime correction made by CLOCK Scalar data. The Gaussian fits to Rate vs. Step plots are shown here, along with the fit parameters. p0 corresponds to the maximum rate, p1 is the centroid, and p2 is the Gaussian width of the overlap of the bunches.

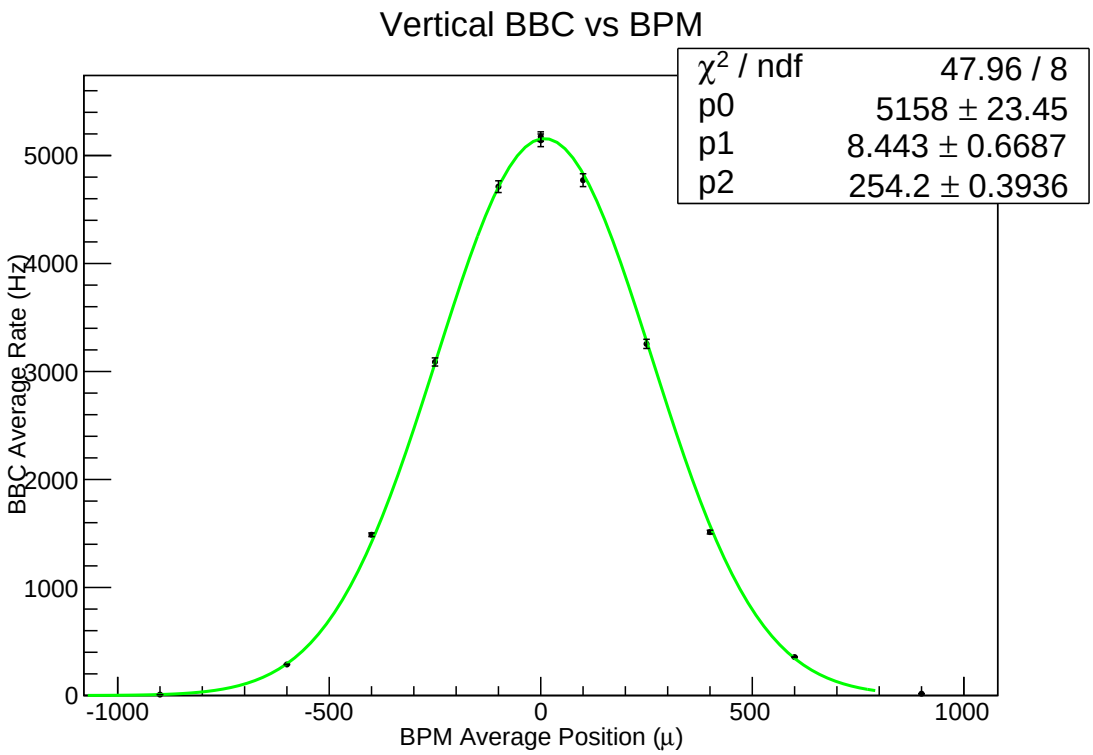

Figure 5.3: Run 431962 Vertical Profile with livetime correction made by CLOCK Scalar data. More Gaussian fits where p0 corresponds to the maximum rate, p1 is the centroid, and p2 is the Gaussian width of the overlap of the bunches.

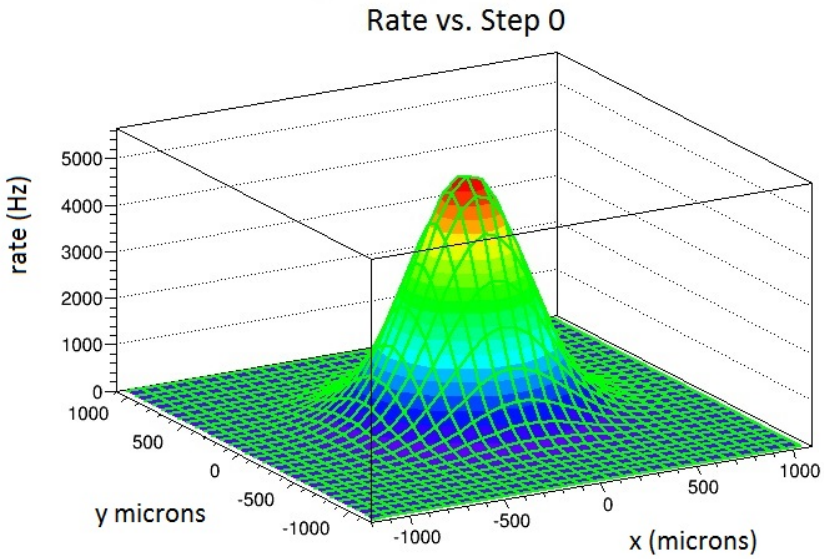

Figure 5.4: Run 431962 2 Dimensional Profile with livetime correction made by CLOCK Scalar data. This is an example of the three dimensional fits which are preferred for extracting the maximum rate.

5.4 PHENIX Raw Data and the Vernier Analysis

There are two main types of data files that are available for analysis at PHENIX. The first is a PHENIX Raw Data File (PRDF) that contains basic scalar data and raw detector hit information. PRDF data is stored in a hierarchy of packets, sorted by event type and packet type. PRDF data packets contain a header, which displays what is contained in the packet, and the epoch timestamp and event number associated with the event. After a first-pass analysis production, a PRDF is converted into a smaller, more easily analyzed and usable Data Summary Tape, or DST.

Due to a trigger configuration setup error, timing information in the form of the CLOCK scalar was not available in the DSTs for runs prior to run 431962. This prevents the bunch-by-bunch livetime correction, and thus inhibits calculation of

the minimum bias maximal event rate using the traditional method of data analysis using DSTs. In theory, correcting for detector livetime and scaling by the number of filled bunches in the rings enables the calculation of the true event rate. For the final run, 431962, CLOCK timing information is available and is used as a cross-check between a new method of data analysis that uses epoch timestamps in PRDFs for timing information, with the traditional method that utilizes DSTs and the CLOCK scalar.

In collaboration with Michael Beaumier from UC Riverside and Martin Purshke from BNL, a new software framework was designed to extract all necessary data packets and headers out of the PRDFs in order to include scans without the CLOCK scaler in the analysis. Contained within the PRDFs are the GL1 packets needed for rate calculation, specifically packets which contains epoch timestamped bunch crossing information and live bunch by bunch scalar count information for a specific numbered event with ATP number. This data is gathered for every timestamp and sorted bunch by bunch, correcting for a slight time offset from the ATPs during data acquisition.

Live event rates for each bunch crossing are calculated for each scalar by adding up the total scalar counts for a particular scalar for a given epoch time period. Event rates for the sum of all bunches are calculated as well for each scalar and are consistent with the Run Summary Log.

The live event rates then are corrected for detector livetime. The livetime of the DAQ is the fraction of time that the DAQ is actively recording data and not busy with trigger processing, recording, etc. Scalar counters record the number of total (raw) triggers, regardless of whether the detector is busy or live, and "live" triggers when the DAQ is not busy. Livetime calculations are computed using another type of PRDF data, the PPG scalar data, which contains an epoch timestamp for each data line as well as cumulative raw and live scaler information for the Minimum Bias

trigger. Livetime is calculated for a step as

$$\text{Livetime} = \frac{\Delta\text{BBC}_{live}}{\Delta\text{BBC}_{raw}}. \tag{5.10}$$

One caveat is that the PPG scaler data comes in approximately every 30 seconds, so the first 3-4 steps in the scan, which are more maximally overlapped, only have one PPG scaler data point. As a result, livetime cannot be calculated for these steps. In order to obtain the livetime at maximal overlap, which is needed to constrain the peak of the Gaussian fit of the event rate vs. step plots, the PPG data at the beginning and/or the end of the Vernier Scan is used, due to maximal beam overlap, and propagated to the maximally overlapped steps in the middle of the scan. Comparison of the measured livetimes at the beginning of a run to those at the end of a run showed that there was a livetime change of $< 5\%$. Another caveat is that the PPG scaler data does not give livetime information for an individual bunch. It only gives the bunch averaged livetime.

Using only the event rate vs. step position data, the results of event rate analysis for Run 431962 using the DST and PRDF methods indicates that the new PRDF method is successful in recovering runs 424347 and 426254 for use in the integrated luminosity calculation. Beam overlap widths are very consistent between the two methods, see Figures 5.5 and 5.6; however, for a few bunch crossings in either the horizontal or vertical directions, the maximal minimum bias event rate for the PRDF method differs by a more than 3σ as indicated by the Gaussian fits, see Figure 5.6. The effect of using coarser timing information naturally yields an increased statistical uncertainty.

Upon completion of the luminosity and σ_{BBC} calculations, a comparison of the final values for the PRDF and DST analysis methods indicates an inconsistency between methods. The naïve assumption for the initial calculation was that the number

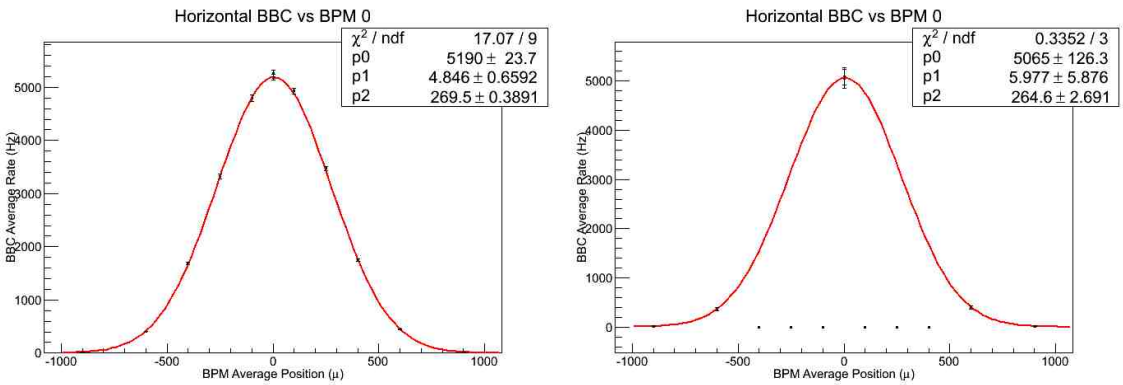

(a) (b)

Figure 5.5: Minimum bias Event rate vs. Beam position in the horizontal direction for one bunch crossing for the (a) DST method and the (b) PRDF method. The results for transverse beam widths and maximal event rate are consistent between methods. For the PRDF method, there is a larger uncertainty for all fit parameters. The data points with a rate of 0 Hz are not included in the fit as they had no available livetime correction.

of protons and densities in each bunch crossing are nearly equal and therefore have similar maximal event rates. All bunch crossings for a specific step were corrected by the same livetime calculation. It was determined that this assumption was incorrect and the number of protons per bunch crossing varied significantly. According to Equation 5.8, for constant (within statistical error) bunch widths, the maximal event rates should increase as the number of particles in each bunch increases, see Figure 5.7; however, with the ppg scaler livetime correction, the event rate tended to fall as the number of protons increased, see Figure 5.8. The livetime correction introduced systematic effects into the analysis that varied by bunch crossing. The ppg scaler data does not provide livetime information for individual bunches.

An important performance characteristic of the BBC is that while the detector is processing an event, the detector becomes "busy" and does not process further events until it is finished. The livetime of the BBC while taking data is nonlinearly

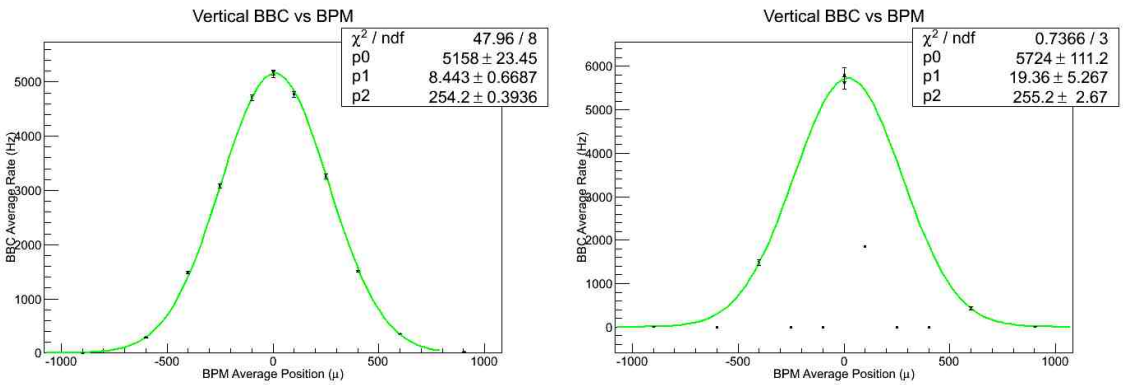

(a) (b)

Figure 5.6: Minimum bias Event rate vs. Beam position in the vertical direction for one bunch crossing for the (a) DST method and the (b) PRDF method. The results for transverse beam widths are consistent between methods, while the maximal event rate differs by more than 3σ. The data points that are used in the fit for the PRDF method have error bars. The data points with a rate of 0 Hz or no error bars are not included in the fit as they had no available livetime correction.

dependent on the event rate, so the variations in event rate that occur between bunch crossings within a scan make it impossible to use a bunch averaged livetime correction to the event rate. If the real, unknown livetime of a bunch crossing is smaller than the calculated average value of livetime, then the calculated maximal event rate will be smaller than in reality, see Figures 5.7 and 5.8. This effect causes the calculated event rate to fall as the true rate increases. The seemingly inverse relationship between the event rate and the number of protons implies that the livetime correction cannot be applied as a bunch average correction, but instead must be considered on a bunch by bunch basis. Because the effect is nonlinear and the relationship cannot be quantified, the PRDF method of livetime calculation cannot be made without introducing large systematic uncertainty that is poorly understood. For all runs prior to 431962, the only available livetime data is the bunch averaged calculation and these are thus excluded from this analysis. The final value of σ_{BBC} is calculated using maximal event rate values of run 431962. The livetime calculation was not required for the

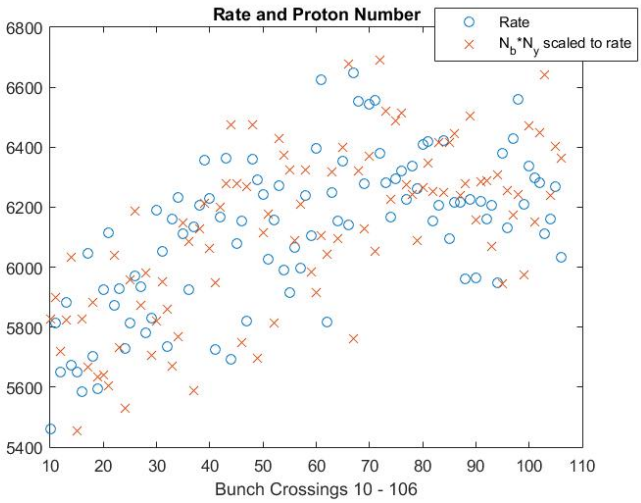

Figure 5.7: Event rate and bunch intensity as a function of bunch crossing for run 431962. The number of protons in each bunch increases with event rate as predicted.

calculation of other parameters, such as the minimum bias trigger efficiency.

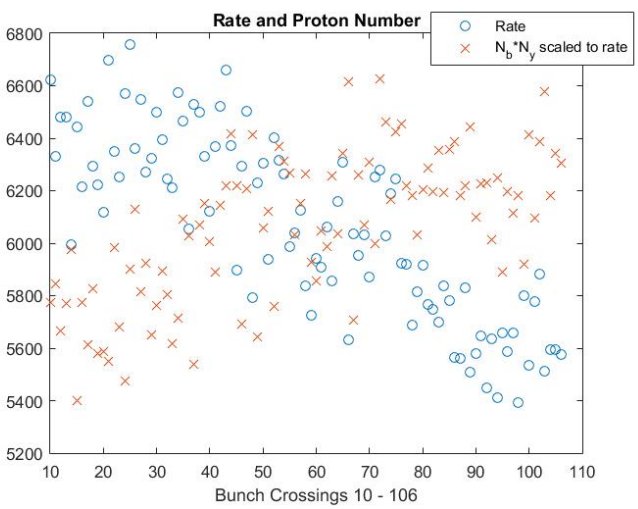

Figure 5.8: The event rate and scaled bunch intensity as a function of bunch crossing using the ppg scaler calculated livetime for run 431962. The decrease in the event rate with the increasing number of protons implies that the livetime correction cannot be applied as a correction to a bunch average, but instead must be applied to individual bunches. Livetime information is not available for individual bunches with the PRDF method and therefore, the true event rates cannot be measured.

5.5 Corrections to the Luminosity

5.5.1 BBC Efficiency

The minimum bias trigger cross section needs to account for the luminosity sampled by the minimum bias trigger, and is effected by the efficiency of the trigger. The Luminosity sampled by the BBC minimum bias trigger is

$$\mathcal{L}_{BBC} = \mathcal{L}_{delivered} \times \epsilon_{BBC}^{MB}, \tag{5.11}$$

where ϵ_{BBC}^{MB}, the minimum bias trigger efficiency, is the fraction of the vertex distribution generated by the total number of BBC triggered events that is triggered on by the minimum bias trigger of the BBC. This is measured by dividing the number of triggers inside the BBCLL1 (>0 tubes) minimum bias trigger width in coincidence with the BBC wide trigger, which gives the total number of events triggered on by the BBC, by the total number of triggers for the BBC. The BBC wide trigger has a vertex range of $z = \pm 144cm$, which is the separation distance of the North and South BBCs along the beamline. The minimum bias trigger efficiency is then

$$\epsilon_{BBC}^{MB} = \frac{N_{BBC}^{MB+wide}}{N_{BBC}^{wide}}. \tag{5.12}$$

The efficiency measurement is common to all crossings. The online cutoff to the BBC vertex is 30 cm, however due to z-vertex smearing, which accounts for the resolution of the BBC, this vertex cutoff was slightly wider. The actual vertex used was $\approx \pm 36$ cm.

Calculation of the minimum bias trigger efficiency involves both live and scaled triggers. As discussed previously, live triggers are accumulated when the DAQ is live. Even though the DAQ is live, storing a high rate of events can be problematic.

To account for this, PHENIX scales the number of events it allows to pass through the DAQ to storage. These scale factors can be varied for individual triggers. Scaled minimum bias triggered events contain full event information, such as event vertex information, that is essential to the Vernier analysis.

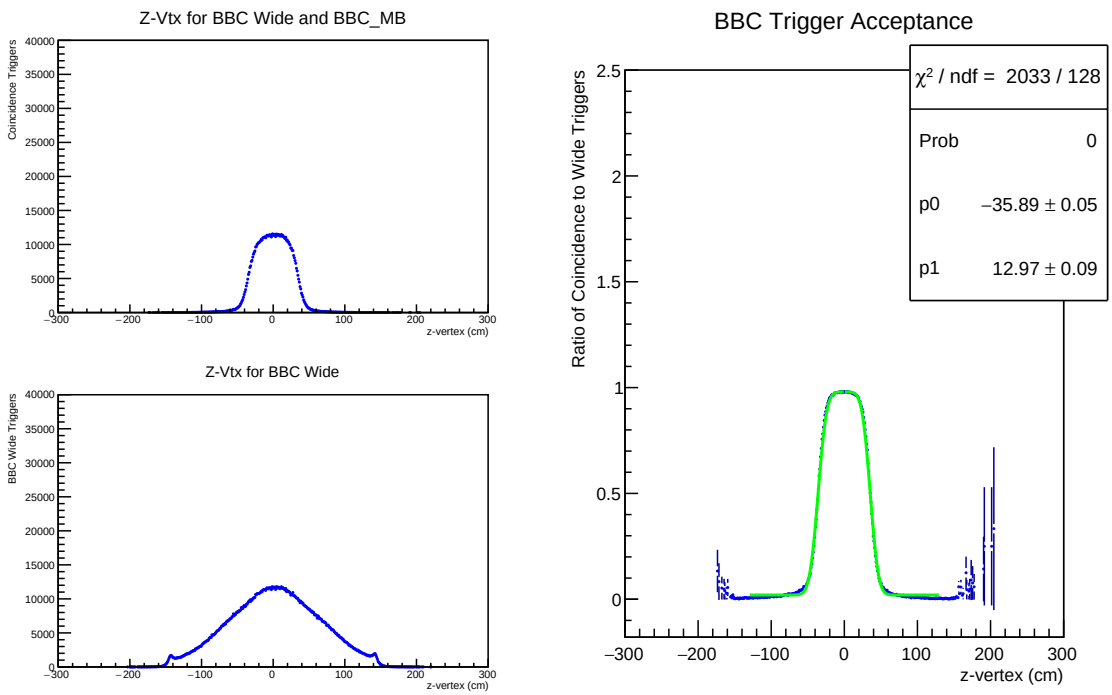

Figure 5.9: Run 431962 BBC z-vertex distributions for the coincidence of live minimum bias triggers with scaled BBC wide triggers (top left), scaled BBC wide triggers (bottom left), and the division of the coincidence distribution by the BBC wide vertex distribution (right).

To obtain the trigger efficiency, the number of live minimum bias triggers in coincidence with the number of scaled BBC wide triggers was divided by the number of scaled BBC wide triggers at maximal beam overlap. For the real offline BBC z-vertex we divide the coincidence distribution by the BBC wide distribution. The shape of this ratio plateaus at 1 and the tails fall sharply. A Gaussian error function is fit to this shape. The offset of the fit function determines the true z-vertex width

used in the analysis as shown in the right plot in Figure 5.9. The z-vertex width used is from -35.9cm to 35.4cm.

Z-Dependence of BBC Trigger Efficiency

The BBC acceptance is dependent on the z-vertex position of the collision. The z-vertex dependence of the acceptance will undercount the real number of triggered events and narrow the BBC vertex position distribution. To correct for the vertex dependence, the ZDC is used to examine the vertex efficiency being located 18 m away from the center of PHENIX. The far distance away from the center of PHENIX relative to the z-vertex width examined makes the z-dependence in the region of the BBC negligible. The vertex efficiency is determined by the ratio of the ZDC z-vertex distributions of the coincidence triggers of the live BBC wide and the scaled ZDC wide with the scaled ZDC wide distribution, see Figure 5.10. This ratio, ϵ^z, is the z-vertex efficiency correction to the minimum bias trigger efficiency. It is applied to the uncorrected efficiency as:

$$\epsilon_{BBC}^{corr} = \frac{\sum_i \frac{\mathrm{N}_i^{mb\&w}}{\epsilon_i^z}}{\sum_i \frac{\mathrm{N}_i^{wide}}{\epsilon_i^z}} \tag{5.13}$$

where i corresponds to a discrete 1cm bin in z. The z-vertex efficiency is dependent upon z-vertex position around the nominal IP and is accounted for in the correction. Run 15 BBC efficiency measurements are approximately 15% lower than in previous

Run	Uncorrected ϵ	Corrected ϵ
424347	0.381	0.340
426254	0.383	0.343
431723	0.386	0.347
431962	0.390	0.351

Table 5.2: Minimum bias trigger uncorrected and corrected efficiency values for each Vernier Scan.

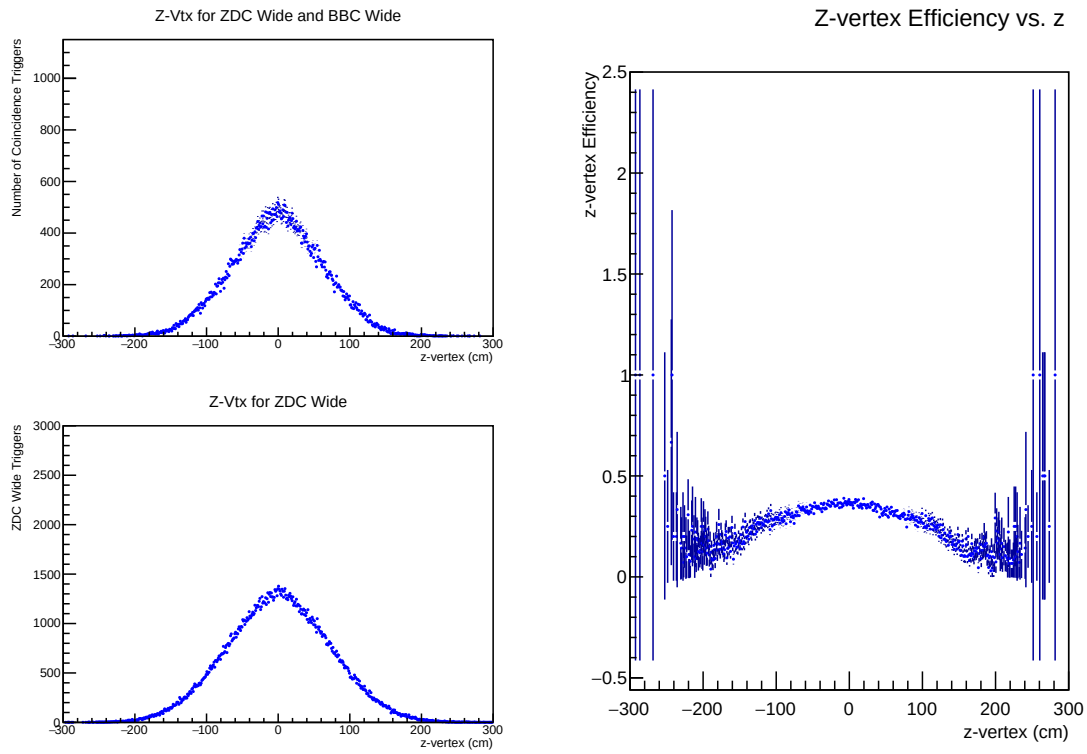

Figure 5.10: Run 431962 ZDCC z-vertex distributions for the coincidence of live minimum bias triggers with scaled ZDC wide triggers (top left), scaled ZDC wide triggers (bottom left), and the division of the coincidence distribution by the ZDC wide vertex distribution (right). The distribution on the right is the z-vertex efficiency of the BBC.

Run years. There is a question as to whether the electronics or detector saturation could render the BBCs at PHENIX and STAR unsuitable for luminosity monitoring at high beam luminosities[109].

5.5.2 Intensity Falloff

As proton bunches collide during the course of a fill, the number of available protons for collisions decreases. During the Vernier scan, the beams can have some

scraping along the beam pipe, especially at minimally overlapped steps, which will also decrease the luminosity. The WCM can monitor these effects when plotted as a function of time; at each step, the intensity is normalized with respect to the first DCCT intensity values, and then multiplied by the associated rate. Data points are typically fit to a linear polynomial, Figures 5.11, however, due to some scans displaying a non-linear decrease, Figure 5.13, the rate values are corrected individually for each step. These corrections are on the order of 1-3%.

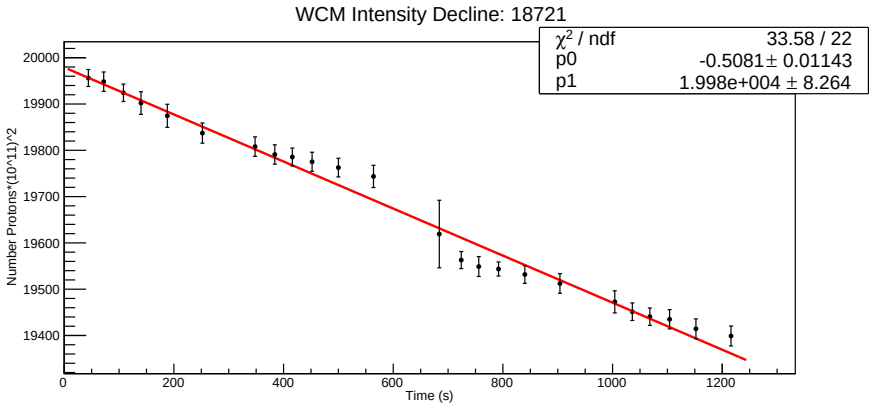

Figure 5.11: Intensity fall off of WCM data for run 424347, versus time.

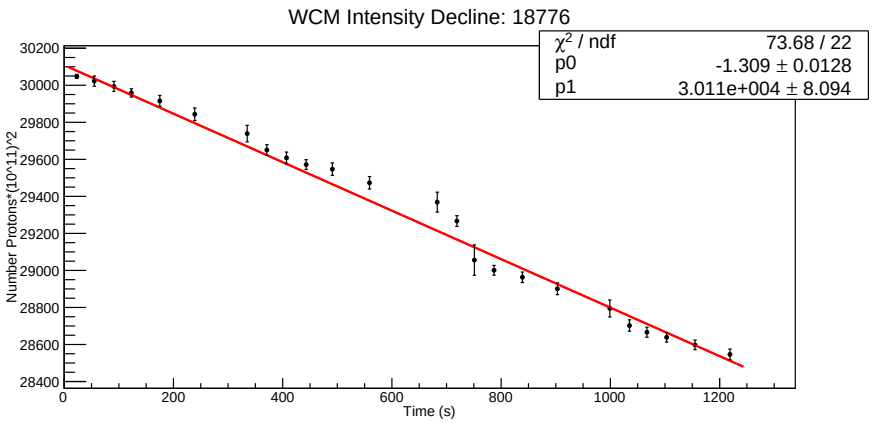

Figure 5.12: Intensity fall off of WCM data for run 426254, versus time.

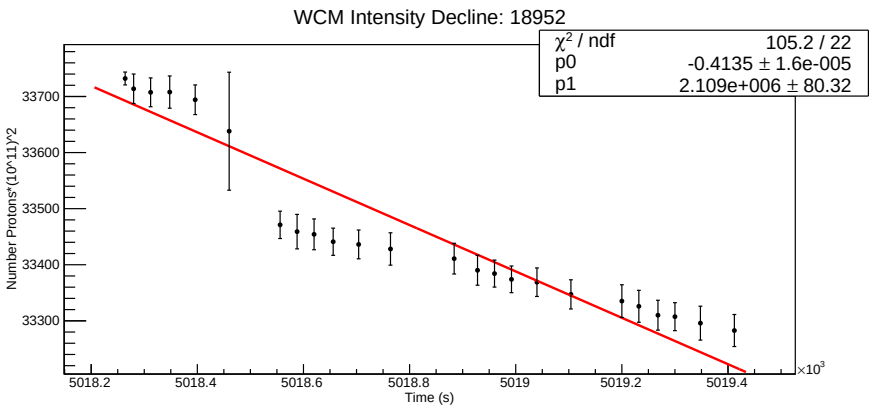

Figure 5.13: Intensity fall off of WCM data for run 431942, versus time.

5.5.3 Multiple Collisions

As a consequence of higher beam luminosities in recent RHIC run years, the multiple collisions effect is examined. The BBC was designed to detect only one collision per bunch crossing, as RHIC luminosities were lower at the time of design. However, as CAD has increased beam intensity, the effect of multiple collisions has become significant. Quantifying the effect of multiple collisions is difficult due to the design of the BBC and its triggering system. The trigger requires hits in both the North and South BBCs and then will reconstruct a single event vertex based upon the timing of the hits. Since the BBC is incapable of differentiating one collision per crossing from two, systematic error is introduced, as the luminosity will be undercalculated. The method used to correct for the multiple collisions effect was developed for the Run 9 Vernier Scan Analysis [111].

Describing the true event rate is the equation,

$$R_{true} = \mu * \epsilon_{side}^2 * \epsilon_{BBC} * f \tag{5.14}$$

where μ is the average number of collisions per bunch crossing, ϵ_{side} is the efficiency of the separate North and South BBCs, ϵ_{BBC} is the minimum bias trigger efficiency,

and f is the frequency of bunch crossings. The average number of collisions per bunch crossing, μ, cannot be directly measured. From Poisson statistics the predicted rate is [112],

$$R_{pred} = \epsilon_{BBC}[1 - 2e^{-2\mu\epsilon_{side}} + e^{-\mu\epsilon_{side}(2-\epsilon_{side})}]. \tag{5.15}$$

An iterative procedure of Newton's method of root finding is utilized to minimize the the difference between observed rate and the predicted rate from Equation 5.15 in order to calculate μ. A value for μ is calculated for each step position, giving an uncertainty in the rate of 5-10% at maximal overlap, and <1% at minimal overlap.

The parameter ϵ_{side} is related to k_n and k_s, the parameters determined in the relative luminosity studies in Run 9[113, 111]. Regarding the BBC, the probability of observing a collision can be broken down into its constituent probabilities:

$$1 = \epsilon_N + \epsilon_S + \epsilon_{NS} + \epsilon_0 \tag{5.16}$$

where $\epsilon_{N(S)}$ is the probability of an event being detected by the north (south) arm, and not being detected by the other arm. ϵ_{NS} is the probability of being seen by both arms, and ϵ_0 is the probability that a collision is not seen [113]. In relative luminosity studies, the parameter of interest is

$$\epsilon_{NS} = \frac{\epsilon_{N(S)}}{k_{N(S)}} \tag{5.17}$$

which is not the quantity needed for the Vernier scan analysis. Instead, the necessary parameter is,

$$\epsilon_{side} = (k_{N(S)} + 1)\epsilon_{NS}. \tag{5.18}$$

An assumption is that hit probability differences in the north and south BBCs are small, and a nominal value for $\epsilon_{side} = .79$ is used. To compensate for possible differences in the North and South hit probabilities, ϵ_{side} is varied by $\pm 3\%$ which gives a systematic error for the multiple collisions correction. Typical values of μ at maximal overlap are 0.4.

5.5.4 The Hourglass Correction

There are quadrupole magnets which focus the beam around the IP. As the beam approaches the IP, it becomes narrower and then spreads out after passing the IP to the stable beam width for storage in the ring. This places a z-dependence on the luminosity.

To find the z-dependent bunch structure and its effects on the luminosity, the bunch density is integrated in four dimensions

$$\mathcal{L} = 2f_0 \iiiint_{-\infty}^{\infty} \rho_+(x,y,z,ct)\rho_-(x,y,z,ct)\,dx\,dy\,dz\,cdt. \tag{5.19}$$

Here, $\rho_\pm$ is the density of each bunch as a function of x, y, z, and ct. Assuming a Gaussian bunch structure in x, y, and z$\pm$ct,

$$\rho_\pm(x,y,z\pm ct) = \frac{N^\pm}{(2\pi)^{3/2}\sigma_x(z)\sigma_y(z)\sigma(z)} e^{(\frac{-x^2}{2\sigma_x(z)}+\frac{-y^2}{2\sigma_y(z)}+\frac{-(z\pm ct)^2}{2\sigma_z})}. \tag{5.20}$$

To account for the dependence of the beam width on z position due to the beam focusing near the IP, the shape of each bunch is modeled as a β function [114]

$$\sigma_{x(y)}(z) = \sigma'_{x(y)}\sqrt{1+(\frac{z}{\beta^*})^2}, \tag{5.21}$$

where $\sigma'_{x(y)}$ is the actual beam width at the nominal interaction poin$\sigma_{x(y)}(z)$, is the bunch overlap width as a function of z-position, and β^* is the focusing parameter, which indicates how much the beams are focused at the nominal interaction point. The luminosity then becomes

$$\mathcal{L} = 2f_0 \frac{N_+N_-}{(2\pi)^3\sigma_x\prime^2\sigma_y\prime^2\sigma_z^2} \iiiint_{-\infty}^{\infty} e^{\frac{-x^2}{\sigma_x^2(z)}+\frac{-y^2}{\sigma_y^2(z)}}\,dx\,dy \frac{e^{\frac{-(z+ct)}{2\sigma_z}+\frac{-(z-ct)}{2\sigma_z}}}{\{1+(\frac{z}{\beta^*})^2\}^2}\,dz\,dt, \tag{5.22}$$

where the dependence on x and y is integrated out to

$$\mathcal{L} = 2f_0 \frac{N_+N_-}{(2\pi)^3\sigma_x\prime^2\sigma_y\prime^2\sigma_z^2} \iint_{-\infty}^{\infty} \pi\sigma_x\prime\sigma_y\prime\{1+(\frac{z}{\beta^*})^2\} \frac{e^{\frac{-(z+ct)}{2\sigma_z}+\frac{-(z-ct)}{2\sigma_z}}}{\{1+(\frac{z}{\beta^*})^2\}^2}\,dz\,dt. \tag{5.23}$$

The beam width is replaced by the overlap width measured in the Vernier Scan, $\sigma_{x(y)} = \sqrt{2} * \sigma_{x(y)}\prime$, and yields

$$\mathcal{L} = f_0 \frac{N_+ N_-}{2(\pi)^2 \sigma_x \sigma_y \sigma_z^2} \iint_{-\infty}^{\infty} \frac{e^{\frac{-(z+ct)}{2\sigma_z} + \frac{-(z-ct)}{2\sigma_z}}}{1 + (\frac{z}{\beta^*})^2} \, dz \, dt, \tag{5.24}$$

where the value of β^* affects the final luminosity, see Figure 5.14. The value of the beta function at the IP is the value of β^*. A perfectly cylindrical bunch would have a β^* value of infinity and as the value decreases, the longitudinal bunch shape becomes an hourglass cross section in the x-z and y-z planes. An hourglass bunch shape increases the luminosity at the IP and further from the IP, the luminosity decreases. The value for the focusing parameter in the x-and y-directions are considered equivalent.

The model for the luminosity needs to be corrected for the true longitudinal bunch structure. The bunch shape is approximated by a Gaussian at first order, but the sensitivity of the correction to the luminosity requires a complete understanding of the bunch shape. The true bunch shape is extracted from WCM data and measured in radio frequency (RF) cavities. When bunches are initially injected into RHIC, they are initially in a single Gaussian bucket which is wider than the final longitudinal bunch structure. An RF cavity reduces the longitudinal bunch width, but not all of the protons in a bunch are compressed by the cavity. After this squeezing, the true bunch shape is a triple Gaussian, see Figure 5.15. The WCM data is fit for the average of all bunches, as the longitudinal bunch distribution is not available for individual bunches. The three Gaussian distributions are combined for numerical integration of the z-dependent luminosity formula.

As bunches collide at the crossing points of RHIC, there is a slight crossing angle in the $x - z$ plane that decreases the luminosity, and this also places a z-dependence on its magnitude. For PHENIX, the crossing angle in the y-z plane is small enough to be neglected. To account for the crossing angle in the numerical computation, the

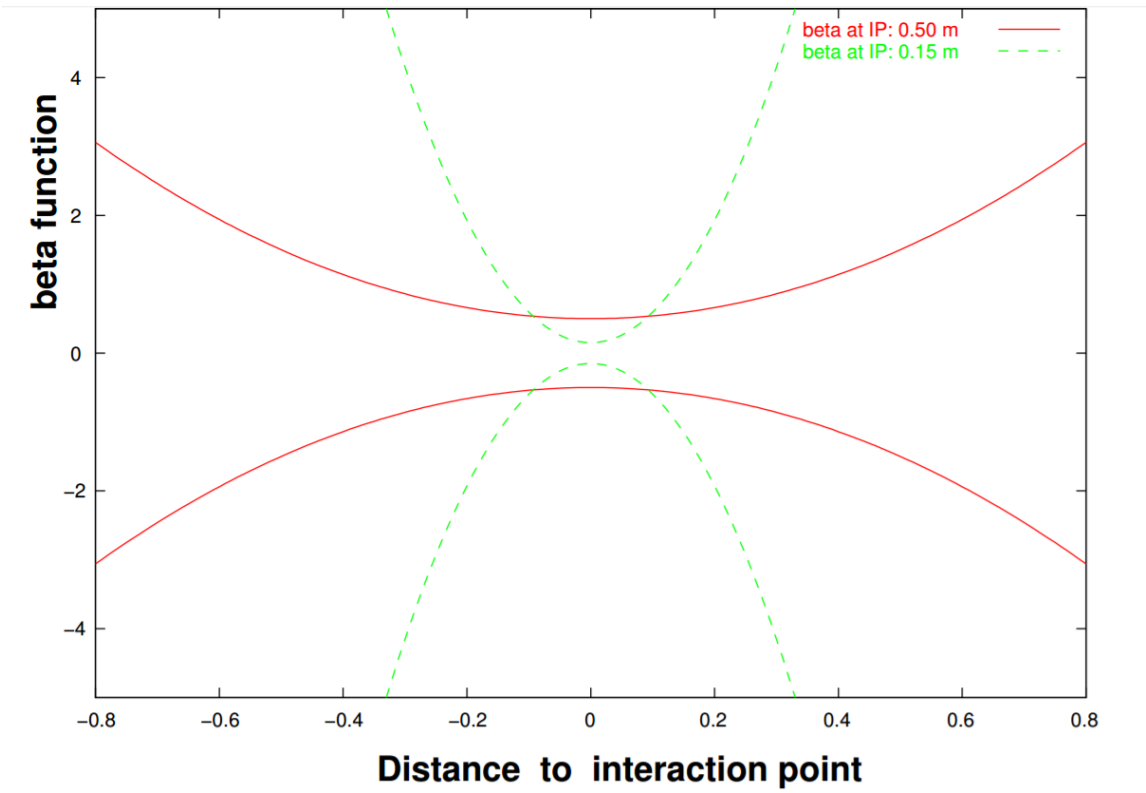

Figure 5.14: Examples of dfferent β^* values as functions of distance to the IP in meters[114].

coordinate system in which the luminosity is calculated is rotated through an angle θ representative of the value of the crossing angle.

Simulations of bunch crossings quantify the effect of β^* and a crossing angle on σ_{BBC}. For a beam without a crossing angle and an infinite β^*, the longitudinal distribution of the event vertex would be Gaussian at each step in the Vernier scan. With a non-infinite β^*, a Gaussian vertex distribution is expected at maximal beam overlap, but at more transversely displaced steps, a double-peaked Gaussian vertex distribution would be measured due to the hourglass shape of the bunches. Combining this effect with a small crossing angle in the x-z plane would still yield a Gaussian at maximal overlap, but at transversely displaced steps, the double-peaked

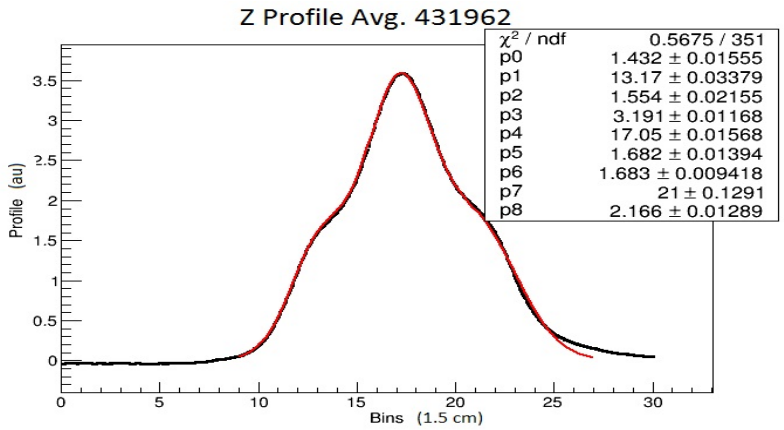

Figure 5.15: Measured longitudinal bunch structure (blue) and the triple Gaussian fit (red) for an individual bunch. The fit parameters represent the fits to the sum of three Gaussian functions to replicate the bunch shape. Each Gaussian has three parameters that represent the normalization, mean, and width of the Gaussian respectively, where p0-p2 correspond to the left Gaussian, p3-p5 to the center Gaussian, and p6-p8 to the right Gaussian.

Gaussians would have unequal amplitudes. The crossing angle causes greater overlap of bunches on one side, causing more collisions in that region. This effect is depicted in the ZDC z-vertex distribution data for different steps, see Figure 5.16.

A numerical longitudinal vertex distribution of the luminous region is generated from the overlap integrals and compared to the ZDC vertex distribution in order to determine β^* and the crossing angle. The ZDC data was selected as the ZDC has no longitudinal efficiency dependence and is able to reconstruct vertices outside the longitudinal acceptance of the BBC. Numerical integration of the full luminosity equation, including the β^* and crossing angle parameters, as well as the true longitudinal bunch structure, is completed over all space to acquire a distribution of z vertices as a function of time. The distribution is normalized and a z-vertex distribution is generated by summing over discrete values of time. To account for the resolution effects of the ZDC, the vertex positions are smeared with a Gaussian for which the position resolution is $\sigma_{ZDC} = 15$cm.

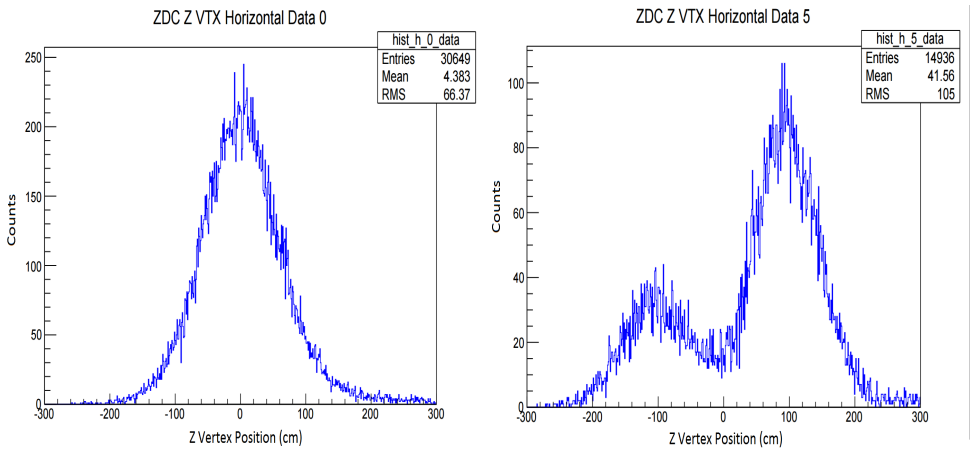

(a) (b)

Figure 5.16: ZDC z Vertex distribution for run 431962 at (a) maximum overlap and (b) minimum overlap. The double peaked z-distribution on the right is a result of the longitudinal changes in bunch structure, where the effect of a finite focusing parameter and a nonzero crossing angle is evident.

Results of this numerical distribution generation are then compared to the data, where the hourglass and crossing angle parameters are optimized to a best fit, then extracted, see Figures 5.5.4, 5.18, and 5.19. Final values of the hourglass correction were found to be approximately $\beta^* = 90$cm and $\theta = 0.06$mrad. It is critical to note that the complexity of the bunch structure and the coarseness of the data introduce large systematic errors, making convergence on specific hourglass parameters difficult. The simulation is used as a confirmation of the parameters quoted by CAD within an uncertainty of ten percent. The normalization parameter to the luminosity S is calculated by dividing the physical luminosity with the extracted values of β^* and the crossing angle by the first order luminosity with an infinite β^* and a crossing angle of 0,

$$S = \frac{\mathcal{L}_{physical}}{\mathcal{L}_{FO}}. \tag{5.25}$$

The luminosity delivered to PHENIX is then

$$\mathcal{L}_{delivered} = S\mathcal{L}_{FO}. \tag{5.26}$$

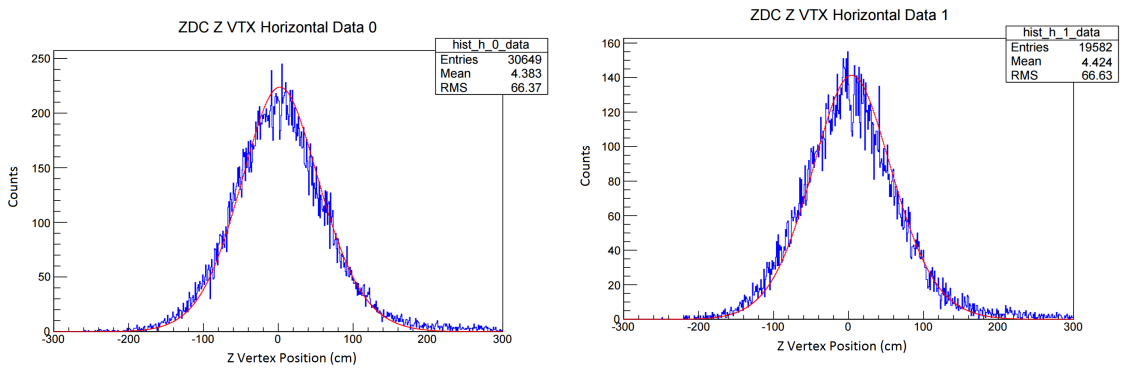

(a) (b)

Figure 5.17: Run 431962 ZDC z-vertex distribution (blue)and the generated numerical ZDC distribution (red) for (a) step 0 (maximal overlap) and (b) step 1 of the Vernier scan.

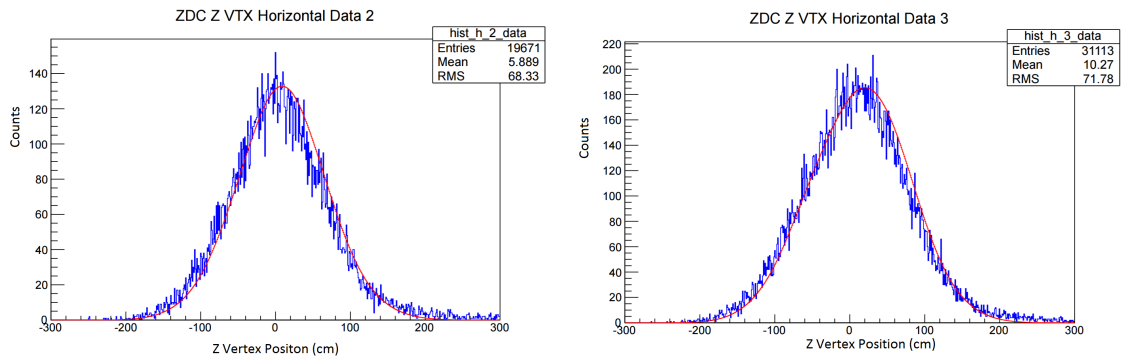

(a) (b)

Figure 5.18: Run 431962 ZDC z-vertex distribution (blue)and the generated numerical ZDC distribution (red) for (a) step 2 (b) and step 3 of the Vernier scan. The simulated z-vertex distribution matches the data.

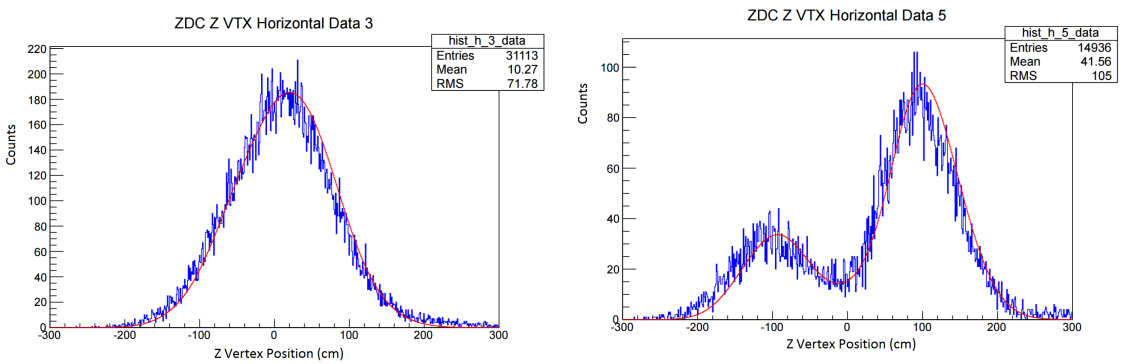

(a) (b)

Figure 5.19: Run 431962 ZDC z-vertex distribution (blue) and the generated numerical ZDC distribution (red) for (a) step 4 (b) and step 5 of the Vernier scan.

5.6 Error Analysis

Systematic errors are associated with each of the parameters of the Vernier Scan analysis. The final systematic error is a function of the errors for each parameter defined by

$$\delta\sigma_{BBC} = \sigma_{BBC}\sqrt{\sum_{i=1}^{n}(\frac{\delta p_i}{p_i})^2}. \tag{5.27}$$

where, p represents any of the parameters used in the minimum bias cross section measurement and δp_i is the systematic error for that parameter.

The systematic error for each parameter was calculated for the uncorrected value, and all of its corrections. The total systematic error for that parameter is the uncorrected error and error for the corrections summed in quadrature.

There are several parameters that did not have any associated systematic errors. For the maximal event rate, R_{max}, the uncorrected value is the total number of minimum bias trigger counts divided by timing information from the CLOCK trigger.

The luminosity decrease during the duration of the Vernier Scan was neglected as the 1% decrease in luminosity was within the systematic error of 2% of the WCM.

Systematic errors for the step positions are calculated from comparing values of R_{max} measured from quoted CAD steps, to BPM steps. The 1.5% difference in the maximal event rate is an associated systematic error. Another systematic error associated with R_{max} from the effect of multiple collisions is discussed in Section 5.5.3. The systematic error from multiple collisions varies with each step, as minimally overlapped bunches will have a lower probability for multiple collisions than maximally overlapped bunches, and the final systematic error is taken as an average over each bunch crossing, for all beam steps. This is applied only to the rate correction and not the overall rate calculation. The systematic error for the corrected R_{max} is $\approx$3%.

CAD values of the systematic errors for the WCM and DCCT readings are used for the calculation of the systematic error for the intensity. The WCM has an error of 2%, and the DCCT a systematic error of 0.2%. Since $N_{b(y)}$ is normalized by intensity readings from the DCCT, the associated systematic error is approximately .8%, which comes from the error of the DCCT adjusted by error from correlation between the DCCT and WCM.

Systematic errors for the bunch overlap widths, σ_x and σ_y, are calculated as combinations of errors in the rate and step positions. The event rate error is obtained by measuring values of $\sigma_{x(y)}$ from the uncorrected event rate, then extracting the fit parameter using the corrected rate. The error, calculated by the differences in $\sigma_{x(y)}$ is approximately 0.5%, with these values calculated similarly to the systematic step position error on the event rate. The fit parameters for $\sigma_{x(y)}$ are taken using CAD quoted steps, then BPM measured steps, and the difference is the systematic error. The error for σ_x is 0.7% and for σ_y, 0.5%.

The systematic error in the minimum bias trigger efficiency, ϵ_{BBC}, is the square root of the variance of the ϵ_{BBC} values for all Vernier scans taken during Run 15. The final value for the systematic error is 0.00439. For run 431962, the systematic error is 1.2%.

The β^* and the crossing angle correction to the luminosity has a large systematic error since the simulation is matched to the data by eye. The range of β^* and crossing angle values around the best matching values between numerical simulation and data that still appear to give a matching z vertex distribution for all steps in the scan are used to compute error for the correction factors. Once the correction factors are calculated using the range of matching values, the difference between them is used as an absolute error on the β^* and crossing angle correction, and the systematic error for these parameters is 10%, which is comparable to the systematic uncertainty from previous analyses[111]. Please see Table 5.3 for a list of all parameters and their associated errors.

Parameter	Error
R_{max}	3%
$N_{b(y)}$	0.8%
$\sigma_{x(y)}$	0.7%(0.5%)
ϵ_{BBC}	1.2%
β^* and θ	10%

Table 5.3: Table of parameters and associated errors.

5.7 Results

The final calculated minimum bias trigger cross section, σ_{BBC}, is measured as

$$\sigma_{BBC} = \frac{R_{max}}{\mathcal{L}_{BBC}} = \frac{R_{max}}{\epsilon_{trig} S \mathcal{L}_{delivered}} = \frac{R_{max}}{f_0 \epsilon_{BBC}} \sum_{crossings} \frac{2\pi\sigma_x\sigma_y}{N_b N_y}. \tag{5.28}$$

The minimum bias cross section is calculated for each bunch crossing, and then a χ^2 minimized fit to a constant function is applied to all bunches. The constant fit parameter is the total minimum bias cross section, see Figure 5.20. The final measurement of the minimum bias trigger cross section, using event rate data from only run 431962, is

$$\sigma_{BBC} = \left(30.0 \pm 1.8^{stat} \pm 3.4^{sys}\right) \text{ mb.} \tag{5.29}$$

where the statistical error is the standard deviation of the bunch-by-bunch minimum bias cross section and the systematic error is 11.3%, discussed in Section 5.6.

It is necessary to acknowledge in Figure 5.20 that the leading bunch crossings in the beam are statistically higher than the following bunch crossings. These bunch crossings are included in the final measurement, because the increase in σ_{BBC} is thought to be a result of the inability of the β^* and crossing angle corrections to be applied to individual bunches. The eight bunches at the beginning of the beam follow a series of empty buckets in the beam known as the abort gap, used for the dumping of the beam at the end of a fill. Due to the abort gap, the effect of space charge is decreased on the beginning bunches in the beam. This effect is well understood, and is observed in other Vernier scans in previous run years [110], and was ignored in the final measurement.

For further information please see the Analysis note[107]. The Run 13 Vernier analysis completed by CAD was performed for the ZDC as the luminosity counter [110].

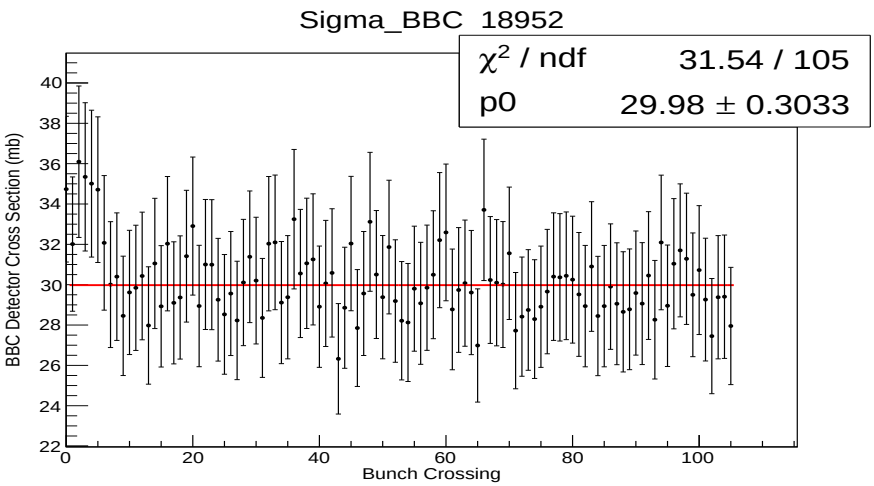

Figure 5.20: The minimum bias cross section, σ_{BBC}, for each bunch crossing of run 431962. The fit function is a constant. The result for σ_{BBC} is parameter p0.

Chapter 6

Summary and Outlook

The inclusive, unpolarized differential production cross section of the J/ψ meson is measured using the PHENIX detector for $p+p$ collisions at $\sqrt{s} = 510$ GeV using the 2013 RHIC dataset. The measurement is performed using the dimuon decay channel for rapidity ranges of $1.2 < |y| < 2.2$ and for transverse momenta up to 12 GeV/c.

While the differential J/ψ production cross section results with respect to rapidity and transverse momentum fall within the predicted range for CGC+NRQCD calculations for low transverse momentum, a more complete picture is needed. The differential $J/\psi \rightarrow e^+e^-$ cross section at mid-rapidity should be measured. This could provide a stricter comparison with theoretical predictions.

The results of this thesis will be published after reaching a consensus with the J/ψ cross section analyzers from Georgia State University (GSU), who performed an independent analysis.

While the 2013 dataset had plentiful statistics, it was plagued with systematic effects from pile-up in the Muon Arms. A substantial amount of corrections concerning pile-up in the MuTr and the MuID due to increased luminosity were necessary

to complete this measurement. These corrections were not necessary for previous datasets, as the beam luminosity was lower. These correction techniques will need to be applied to future datasets to accurately account for the decrease in detector and trigger efficiencies due to pile-up from multiple collisions. The PHENIX simulation framework has already been altered from these studies to easily accommodate correction factors for the MuTr for later datasets.

As RHIC upgrades its technology, it is necessary to have detectors that are able to adapt to changing beam luminosity. As PHENIX is upgrading to sPHENIX, the changing needs of the future accelerator capabilities need to be considered in detector design to avoid systematic issues with future measurements.

Appendices

Appendix A

PYTHIA Simulation Input Parameters

```
roots   510
proj    p
targ    p
frame   cms
msel    0     // turn on all prod. mechanisms manually
msub    86 1  // g+g->j/psi
msub    106 1   // g+g -> J/psi+gamma turned ON
msub    107 1   // g+gamma -> J/psi+g turned ON
msub    108 1   // gamma+gamma->J/psi+gamma turned ON
mdme 858 1 0  // j/psi -> ee turned off
mdme 859 1 1  // j/psi -> mumu turned on
mdme 860 1 0  // j/psi -> random turned off
mstp    51 10041    // structure function for CTEQ6L
mstp    52 2    // use LHAPDF
```

Appendix B

Runs Excluded from Run 13 J/ψ Analysis

North	South
387078	387078
387713	389445
388633	389571
389434	389906
389445	392353
389571	393581
389762	394533
389906	394538
392225	398122
392277	398137

North	South
392280	
393531	
393581	
394389	
394391	
394538	
397207	
398031	
398120	
398122	
398137	

Appendix C

Runs Included in Run 13 J/ψ Analysis

C.1 South Arm

386773 386775 386776 386777 386825 386826 386827 386828 386829 386830 386831
386833 386838 386839 386841 386843 386844 386881 386882 386883 386884 386941
386942 386943 386946 386947 386948 386950 386951 386952 386954 387027 387068
387070 387072 387073 387076 387077 387081 387082 387083 387128 387129 387131
387138 387139 387227 387247 387250 387290 387292 387412 387414 387423 387424
387428 387430 387431 387433 387436 387539 387541 387543 387546 387550 387551
387552 387557 387558 387560 387561 387564 387565 387566 387570 387571 387649
387651 387658 387659 387660 387661 387666 387668 387669 387670 387672 387673
387674 387676 387710 387719 387721 387724 387725 387784 387785 387787 387788
387790 387792 387793 387801 387802 387803 387806 387808 387809 387963 387966
387967 387968 387969 388004 388019 388020 388021 388022 388023 388038 388039
388042 388047 388050 388051 388052 388261 388263 388264 388265 388266 388403

388404 388405 388495 388536 388537 388538 388539 388540 388541 388545 388547
388548 388632 388633 388634 388638 388640 388692 388693 388694 388696 388697
388698 388699 388700 388720 388721 388723 388724 388726 388742 388743 388744
388745 388837 388838 388839 388840 388858 388859 388860 388862 388863 388864
388865 388866 388978 388980 388981 388984 388985 388986 389119 389120 389121
389122 389123 389124 389126 389257 389320 389321 389322 389323 389324 389325
389326 389327 389334 389335 389336 389338 389339 389424 389434 389435 389436
389444 389446 389447 389471 389557 389558 389559 389560 389562 389570 389573
389575 389576 389577 389578 389579 389586 389587 389588 389589 389590 389702
389703 389750 389752 389755 389756 389758 389759 389760 389761 389762 389765
389766 389767 389768 389904 389907 389908 389909 390026 390029 390030 390031
390032 390033 390038 390039 390174 390175 390176 390230 390231 390232 390234
390236 390237 390239 390306 390311 390312 390313 390314 390315 390316 390318
390319 390418 390419 390421 390422 390423 390424 390425 390507 390510 390511
390512 390515 390517 390518 390519 390537 390538 390539 390540 390541 390542
390613 390615 390667 390669 390670 390674 390677 390942 390943 390944 390946
390952 390954 390955 390958 390959 390961 390962 390963 390964 390965 390966
391036 391041 391047 391048 391049 391050 391051 391100 391167 391169 391170
391173 391174 391175 391177 391288 391291 391293 391296 391371 391372 391374
391375 391376 391377 391442 391445 391446 391447 391449 391450 391465 391466
391467 391468 391469 391470 391471 391566 391567 391569 391573 391579 391580
391583 391584 391585 391588 391722 391728 391813 391815 391816 391817 391818
391819 391857 391860 391861 391862 391863 391868 391869 391870 391871 391872
391873 391875 391876 391966 391967 391968 391969 391970 391982 391998 392014
392015 392021 392022 392023 392026 392027 392028 392102 392103 392104 392106
392147 392152 392154 392155 392156 392157 392160 392162 392218 392220 392223
392225 392226 392227 392228 392231 392267 392276 392277 392279 392280 392281
392282 392285 392292 392293 392294 392296 392297 392298 392299 392354 392355

392359 392415 392418 392420 392421 392422 392428 392429 392430 392431 392540
392541 392542 392545 392546 392548 392712 392713 392714 392715 392716 392811
392814 392818 392819 392820 392821 392836 392837 392838 392840 392842 392844
392845 392846 392848 392922 392923 392925 392926 392928 392934 392941 392942
392943 392944 392946 392947 393051 393054 393056 393061 393062 393064 393066
393067 393068 393164 393167 393175 393176 393177 393178 393179 393180 393341
393342 393343 393345 393349 393351 393456 393457 393458 393460 393461 393462
393464 393469 393471 393478 393481 393482 393483 393484 393485 393486 393487
393529 393530 393531 393534 393574 393575 393576 393577 393578 393579 393598
393599 393600 393601 393616 393619 393627 393628 393673 393674 393677 393795
393798 393805 393809 393810 393883 393885 393886 393888 393890 393891 393897
393898 393901 393902 393905 394002 394003 394004 394005 394048 394049 394050
394053 394054 394055 394056 394057 394060 394061 394062 394065 394066 394067
394068 394069 394070 394072 394266 394269 394272 394368 394388 394389 394390
394391 394398 394400 394402 394403 394407 394416 394417 394420 394421 394422
394423 394525 394526 394528 394532 394534 394539 394669 394671 394676 394677
394679 394682 394683 394684 394689 394690 394692 394693 394698 394699 394700
394701 394702 394703 394704 394739 394741 394742 394743 394744 394745 394746
394748 394750 394751 394962 394963 394964 394965 394968 394969 394970 394976
394977 394978 394979 394980 394981 394982 395096 395098 395099 395102 395103
395223 395225 395228 395229 395230 395231 395233 395238 395239 395242 395244
395389 395390 395396 395397 395398 395399 395402 395405 395406 395407 395408
395411 395412 395413 395419 395420 395430 395431 395432 395526 395527 395544
395545 395546 395549 395550 395551 395552 395553 395587 395588 395589 395590
395591 395592 395593 395594 395595 395597 395599 395639 395640 395641 395642
395643 395645 395646 395647 395648 395731 395732 395733 395734 395768 395769
395770 395771 395775 395776 395777 395808 395809 395810 395811 395813 395816
395817 395819 395882 395884 395899 395901 395907 395908 395939 395940 395941

396048 396049 396050 396051 396054 396056 396058 396061 396063 396064 396065
396066 396067 396069 396070 396072 396073 396074 396075 396268 396269 396274
396276 396277 396279 396280 396363 396366 396412 396413 396414 396415 396417
396418 396433 396434 396435 396437 396438 396439 396440 396544 396545 396546
396547 396549 396552 396554 396560 396561 396562 396563 396612 396614 396615
396616 396617 396618 396619 396627 396628 396629 396630 396631 396633 396634
396635 396636 396677 396678 396680 396681 396682 396683 396684 396760 396761
396762 396764 396765 396766 396767 396768 396785 396790 396799 396802 396803
396887 396888 396889 396890 396891 396910 396911 396914 396915 396916 396918
396919 396921 396993 396994 396995 396997 396998 396999 397000 397049 397062
397065 397066 397067 397068 397069 397070 397176 397177 397178 397181 397182
397184 397201 397205 397206 397207 397208 397290 397291 397293 397294 397295
397296 397297 397313 397315 397316 397317 397318 397319 397320 397322 397401
397402 397403 397404 397407 397431 397432 397433 397434 397436 397437 397438
397440 397511 397512 397513 397515 397516 397517 397519 397520 397524 397525
397526 397527 397531 397532 397533 397534 397535 397577 397580 397581 397582
397585 397587 397588 397589 397590 397692 397694 397700 397702 397705 397706
397708 397710 397711 397712 397714 397715 397735 397737 397738 397864 397866
397867 397868 397917 397929 397933 397934 397935 397938 397989 397990 398005
398007 398009 398010 398011 398012 398013 398014 398017 398018 398019 398020
398026 398027 398028 398029 398030 398031 398119 398120 398123 398124 398125
398129 398130 398131 398132 398133 398134 398138 398139 398140 398142 398144
398145 398146 398147 398148 398149

C.2 North Arm

386773 386775 386776 386777 386825 386826 386827 386828 386829 386830 386831
386833 386838 386839 386841 386843 386844 386881 386882 386883 386884 386941
386942 386943 386946 386947 386948 386950 386951 386952 386954 387027 387068
387070 387072 387073 387076 387077 387081 387083 387086 387128 387129 387131
387138 387139 387227 387247 387250 387290 387292 387412 387414 387423 387424
387428 387430 387431 387433 387436 387539 387541 387543 387546 387550 387551
387552 387557 387558 387560 387561 387564 387566 387570 387571 387649 387651
387658 387659 387660 387661 387666 387668 387669 387670 387672 387673 387674
387676 387710 387719 387721 387724 387725 387784 387785 387787 387788 387790
387792 387793 387801 387802 387803 387806 387808 387809 387963 387966 387967
387968 387969 388004 388019 388020 388021 388022 388023 388038 388039 388042
388047 388050 388051 388052 388261 388263 388264 388265 388266 388403 388404
388405 388495 388536 388537 388538 388539 388540 388541 388545 388547 388548
388632 388634 388638 388640 388692 388693 388694 388696 388697 388698 388699
388700 388720 388721 388723 388724 388726 388742 388743 388744 388745 388837
388838 388839 388840 388858 388859 388860 388862 388863 388864 388865 388866
388978 388980 388981 388984 388985 388986 389119 389120 389121 389122 389123
389124 389126 389252 389257 389320 389321 389322 389323 389324 389325 389326
389327 389334 389335 389336 389338 389339 389424 389435 389436 389444 389446
389447 389471 389557 389558 389559 389560 389562 389570 389573 389575 389576
389577 389578 389579 389586 389587 389588 389589 389590 389702 389703 389750
389752 389755 389756 389758 389759 389760 389761 389765 389766 389767 389768
389904 389907 389908 389909 390026 390029 390030 390031 390032 390033 390038
390039 390174 390175 390176 390230 390231 390232 390234 390236 390237 390239
390306 390311 390312 390313 390314 390315 390316 390318 390319 390418 390419
390421 390422 390423 390424 390425 390507 390510 390511 390512 390515 390517

390518 390519 390537 390538 390539 390540 390541 390542 390613 390615 390667
390669 390670 390674 390677 390942 390943 390944 390946 390952 390954 390955
390958 390959 390961 390962 390963 390964 390965 390966 391036 391041 391047
391048 391049 391050 391051 391100 391167 391169 391170 391173 391174 391175
391177 391288 391291 391293 391371 391372 391374 391375 391376 391377 391442
391445 391446 391447 391449 391450 391465 391466 391467 391468 391469 391470
391471 391566 391567 391569 391573 391579 391580 391583 391584 391585 391588
391722 391728 391813 391815 391816 391817 391818 391819 391857 391860 391861
391862 391863 391868 391869 391870 391871 391872 391873 391875 391876 391966
391967 391968 391969 391970 391982 391998 392014 392015 392021 392022 392023
392026 392027 392028 392102 392103 392104 392106 392147 392152 392154 392155
392156 392157 392160 392162 392218 392220 392223 392226 392227 392228 392231
392267 392276 392279 392281 392282 392285 392292 392293 392294 392296 392297
392298 392299 392353 392354 392355 392359 392415 392418 392420 392421 392422
392428 392429 392430 392431 392540 392541 392542 392545 392546 392548 392712
392713 392714 392715 392716 392811 392814 392818 392819 392820 392821 392836
392837 392838 392840 392842 392844 392845 392846 392848 392922 392923 392925
392926 392928 392934 392941 392942 392943 392944 392946 392947 393051 393054
393056 393061 393062 393064 393066 393067 393068 393164 393167 393175 393176
393177 393178 393179 393180 393341 393342 393343 393345 393349 393351 393456
393457 393458 393460 393461 393462 393464 393469 393471 393478 393481 393482
393483 393484 393485 393486 393487 393529 393530 393534 393574 393575 393576
393577 393578 393579 393598 393599 393600 393601 393616 393619 393627 393628
393673 393674 393677 393795 393798 393805 393809 393810 393883 393885 393886
393888 393890 393891 393897 393898 393901 393902 393905 394002 394003 394004
394005 394048 394049 394050 394053 394054 394055 394056 394057 394060 394061
394062 394065 394066 394067 394068 394069 394070 394072 394266 394269 394272
394388 394390 394398 394400 394402 394403 394407 394416 394417 394420 394421

394422 394423 394525 394526 394528 394532 394533 394534 394539 394669 394671
394676 394677 394679 394682 394683 394684 394689 394690 394692 394693 394698
394699 394700 394701 394702 394703 394704 394739 394741 394742 394743 394744
394745 394746 394748 394750 394751 394962 394963 394964 394965 394968 394969
394970 394976 394977 394978 394979 394980 394981 394982 395096 395098 395099
395102 395103 395223 395225 395228 395229 395230 395231 395233 395238 395239
395242 395244 395389 395390 395396 395397 395398 395399 395402 395405 395406
395407 395408 395411 395412 395413 395419 395420 395430 395431 395432 395526
395527 395544 395545 395546 395549 395550 395551 395552 395553 395587 395588
395589 395590 395591 395592 395593 395594 395595 395597 395599 395639 395640
395641 395642 395643 395645 395646 395647 395648 395731 395732 395733 395734
395768 395769 395770 395771 395775 395776 395777 395808 395809 395810 395811
395813 395816 395817 395819 395882 395884 395899 395901 395907 395908 395939
395940 395941 396048 396049 396050 396051 396054 396056 396058 396061 396063
396064 396065 396066 396067 396069 396070 396072 396073 396074 396075 396268
396269 396274 396276 396277 396279 396280 396363 396366 396412 396413 396414
396415 396417 396418 396433 396434 396435 396437 396438 396439 396440 396544
396545 396546 396547 396549 396552 396554 396560 396561 396562 396563 396612
396614 396615 396616 396617 396618 396619 396627 396628 396629 396630 396631
396633 396634 396635 396636 396677 396678 396680 396681 396682 396683 396684
396760 396761 396762 396764 396765 396766 396767 396768 396785 396790 396799
396802 396803 396887 396888 396889 396890 396891 396910 396911 396914 396915
396916 396918 396919 396921 396993 396994 396995 396997 396998 396999 397000
397049 397062 397065 397066 397067 397068 397069 397070 397176 397177 397178
397181 397182 397184 397201 397205 397206 397208 397290 397291 397293 397294
397295 397296 397297 397313 397315 397316 397317 397318 397319 397320 397322
397401 397402 397403 397404 397407 397431 397432 397433 397434 397436 397437
397438 397440 397511 397512 397513 397515 397516 397517 397519 397520 397524

397525 397526 397527 397531 397532 397533 397534 397535 397577 397580 397581
397582 397585 397587 397588 397589 397590 397692 397694 397700 397702 397705
397706 397708 397710 397711 397712 397714 397715 397735 397737 397738 397864
397866 397867 397868 397917 397929 397933 397934 397935 397938 397989 397990
398005 398007 398009 398010 398011 398012 398013 398014 398017 398018 398019
398020 398026 398027 398028 398029 398030 398119 398123 398124 398125 398129
398130 398131 398132 398133 398134 398138 398139 398140 398142 398144 398145
398146 398147 398148 398149

Appendix D

Raw Yield Extraction from Fitting

D.1 North Arm Fits for Rapidity Integrated p_T Bins

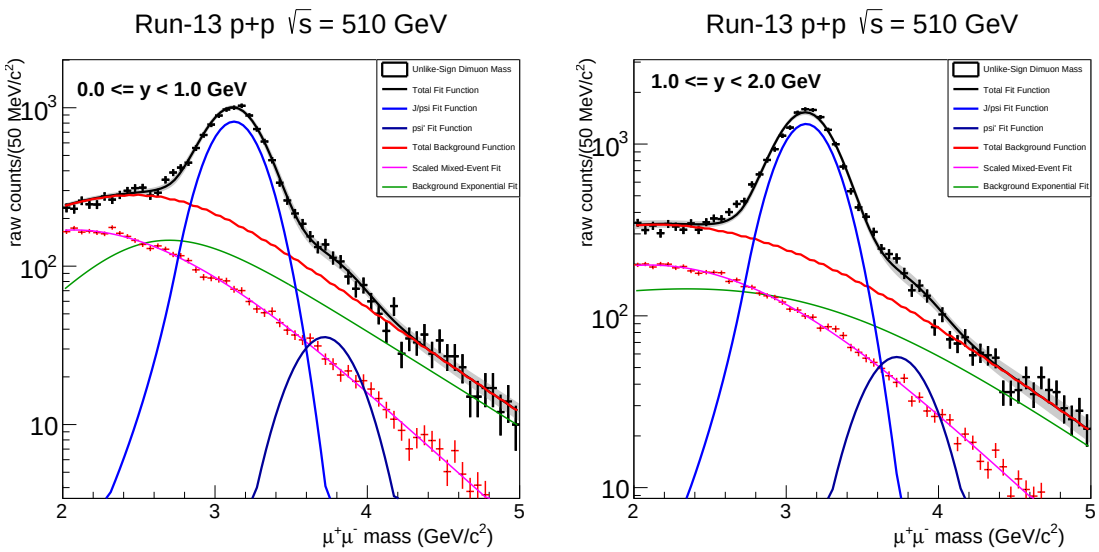

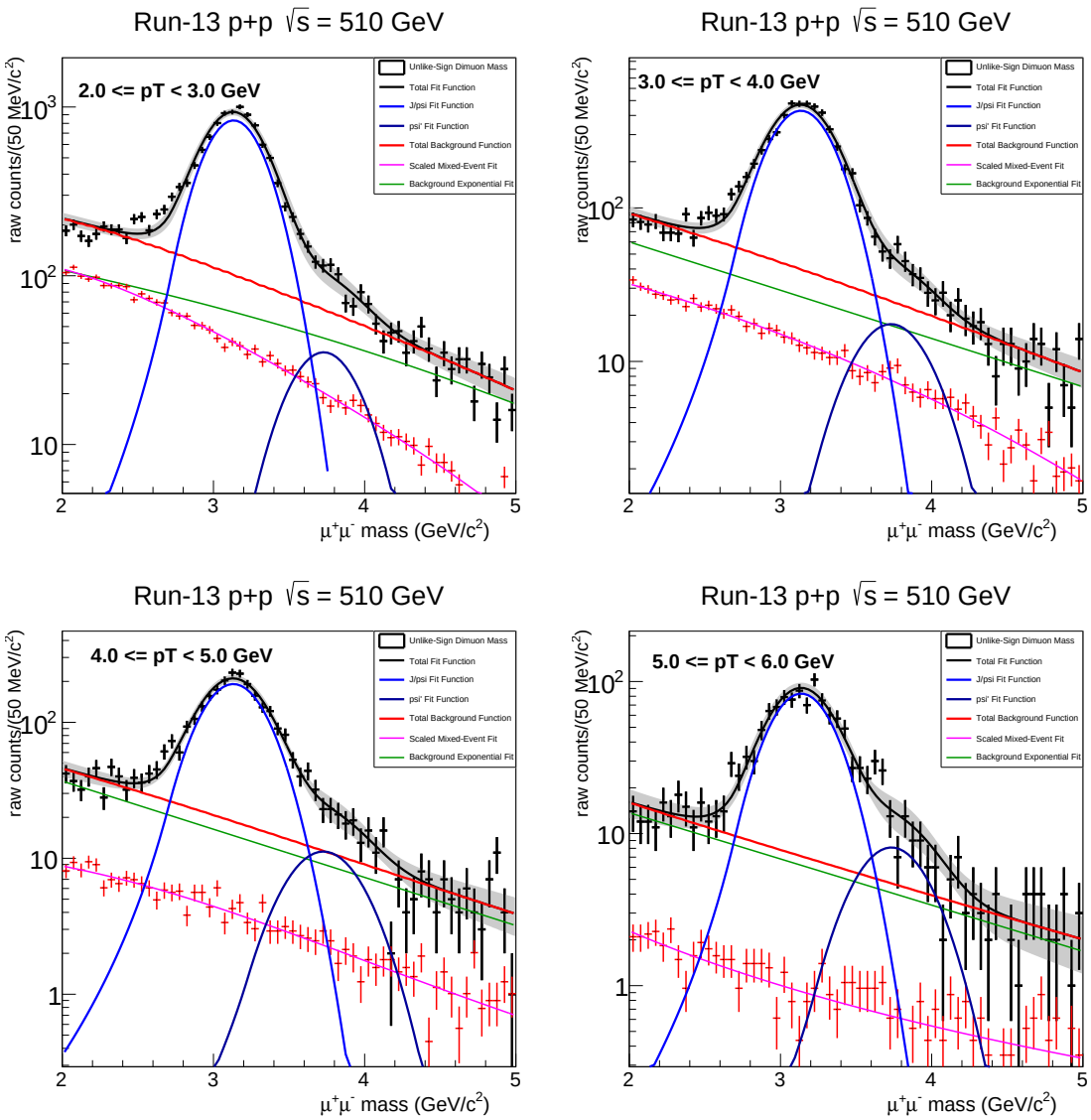
Run-13 p+p √s = 510 GeV
2.0 <= pT < 3.0 GeV
3.0 <= pT < 4.0 GeV
4.0 <= pT < 5.0 GeV
5.0 <= pT < 6.0 GeV
Unlike-Sign Dimuon Mass
Total Fit Function
J/psi Fit Function
psi' Fit Function
Total Background Function
Scaled Mixed-Event Fit
Background Exponential Fit
raw counts/(50 MeV/c²)
μ⁺μ⁻ mass (GeV/c²)

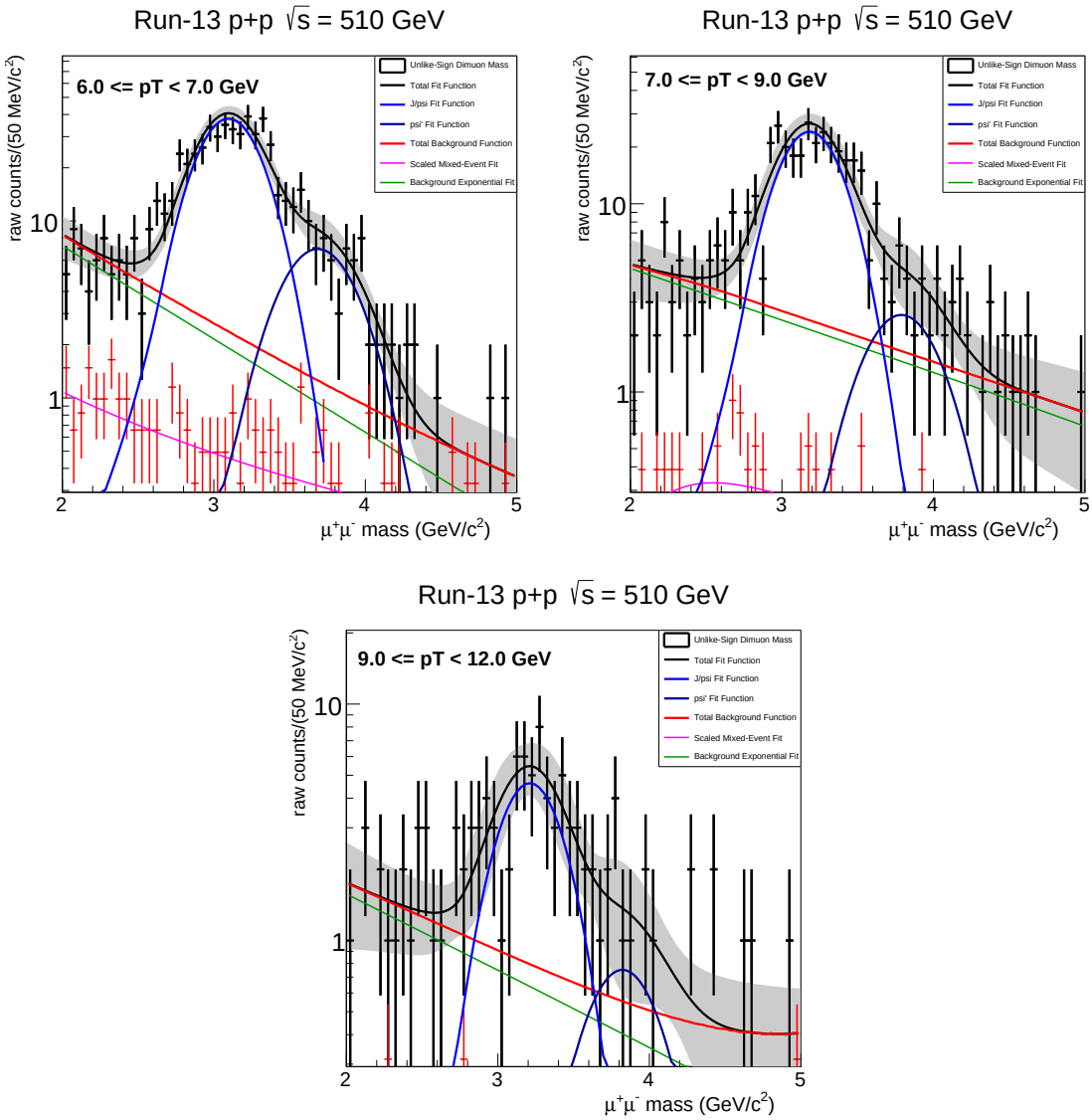

Figure D.-1: North arm dimuon mass spectrum for transverse momentum bins from 0 to 12 GeV. The J/ψ and $\psi\prime$ mass peaks are each fit with a Gaussian plus a crystal ball function. The mixed event backgroun

D.2 South Arm Fits for Rapidity Integrated p_T Bins

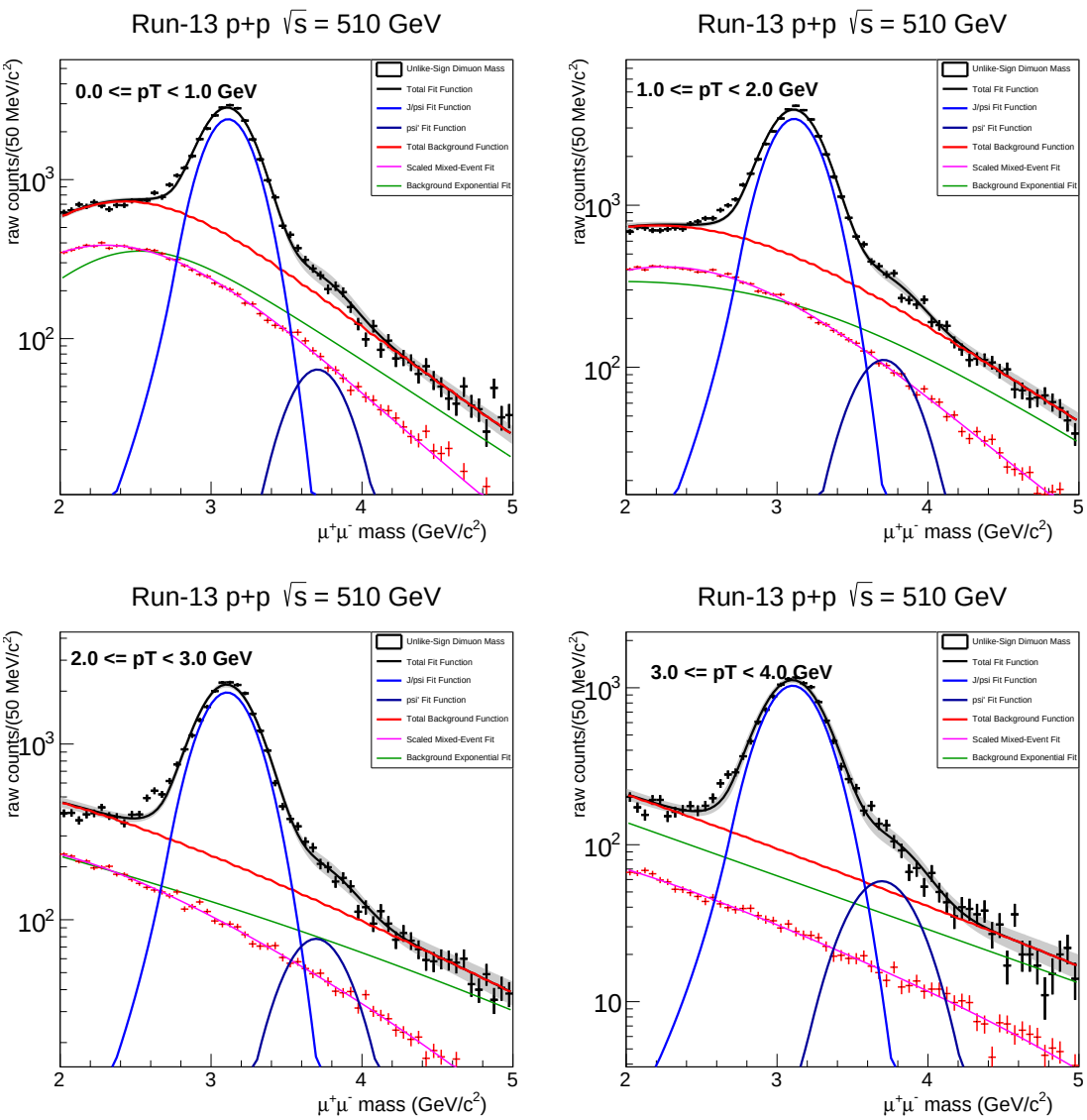

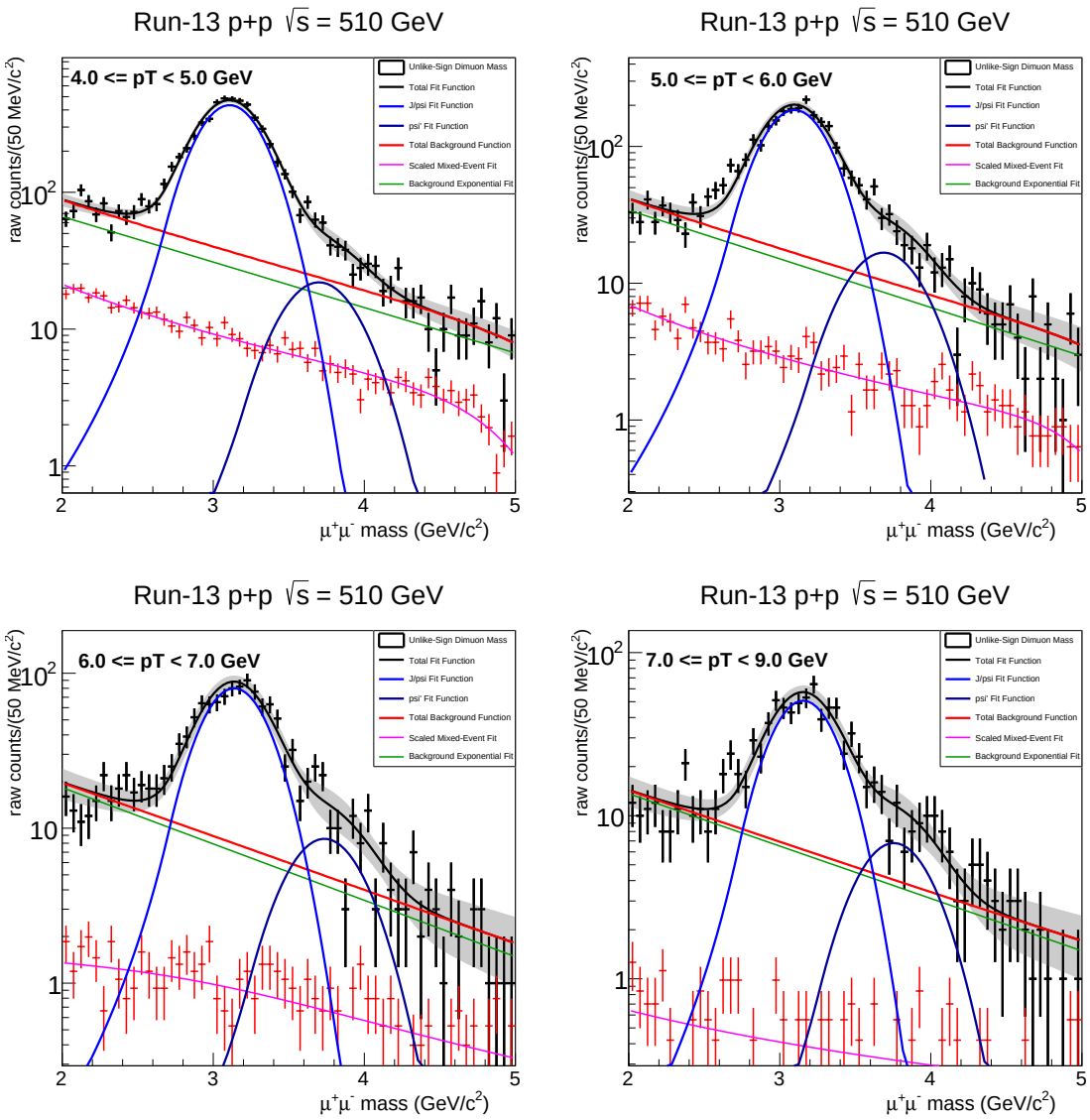
Run-13 p+p $\sqrt{s}$ = 510 GeV
4.0 <= pT < 5.0 GeV
Unlike-Sign Dimuon Mass
Total Fit Function
J/psi Fit Function
psi' Fit Function
Total Background Function
Scaled Mixed-Event Fit
Background Exponential Fit
raw counts/(50 MeV/c^2)
$\mu^+\mu^-$ mass (GeV/c^2)
Run-13 p+p $\sqrt{s}$ = 510 GeV
5.0 <= pT < 6.0 GeV
Unlike-Sign Dimuon Mass
Total Fit Function
J/psi Fit Function
psi' Fit Function
Total Background Function
Scaled Mixed-Event Fit
Background Exponential Fit
raw counts/(50 MeV/c^2)
$\mu^+\mu^-$ mass (GeV/c^2)
Run-13 p+p $\sqrt{s}$ = 510 GeV
6.0 <= pT < 7.0 GeV
Unlike-Sign Dimuon Mass
Total Fit Function
J/psi Fit Function
psi' Fit Function
Total Background Function
Scaled Mixed-Event Fit
Background Exponential Fit
raw counts/(50 MeV/c^2)
$\mu^+\mu^-$ mass (GeV/c^2)
Run-13 p+p $\sqrt{s}$ = 510 GeV
7.0 <= pT < 9.0 GeV
Unlike-Sign Dimuon Mass
Total Fit Function
J/psi Fit Function
psi' Fit Function
Total Background Function
Scaled Mixed-Event Fit
Background Exponential Fit
raw counts/(50 MeV/c^2)
$\mu^+\mu^-$ mass (GeV/c^2)

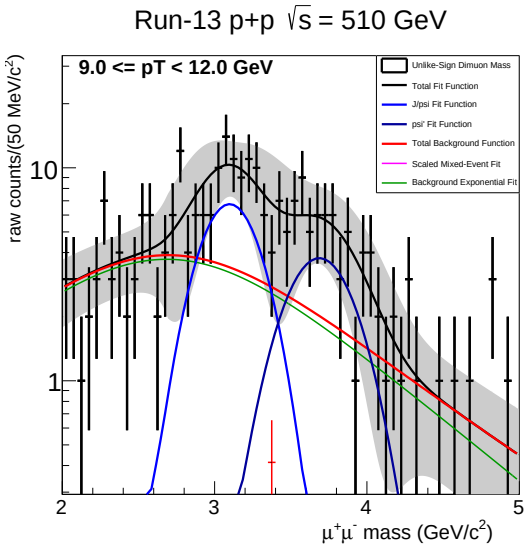

Figure D.-2: South arm dimuon mass spectrum for transverse momentum bins from 0 to 12 GeV. The J/ψ and $\psi\prime$ mass peaks are each fit with a Gaussian plus a crystal ball function. The mixed event backgroun

D.3 North Arm p_T Integrated Rapidity Bins

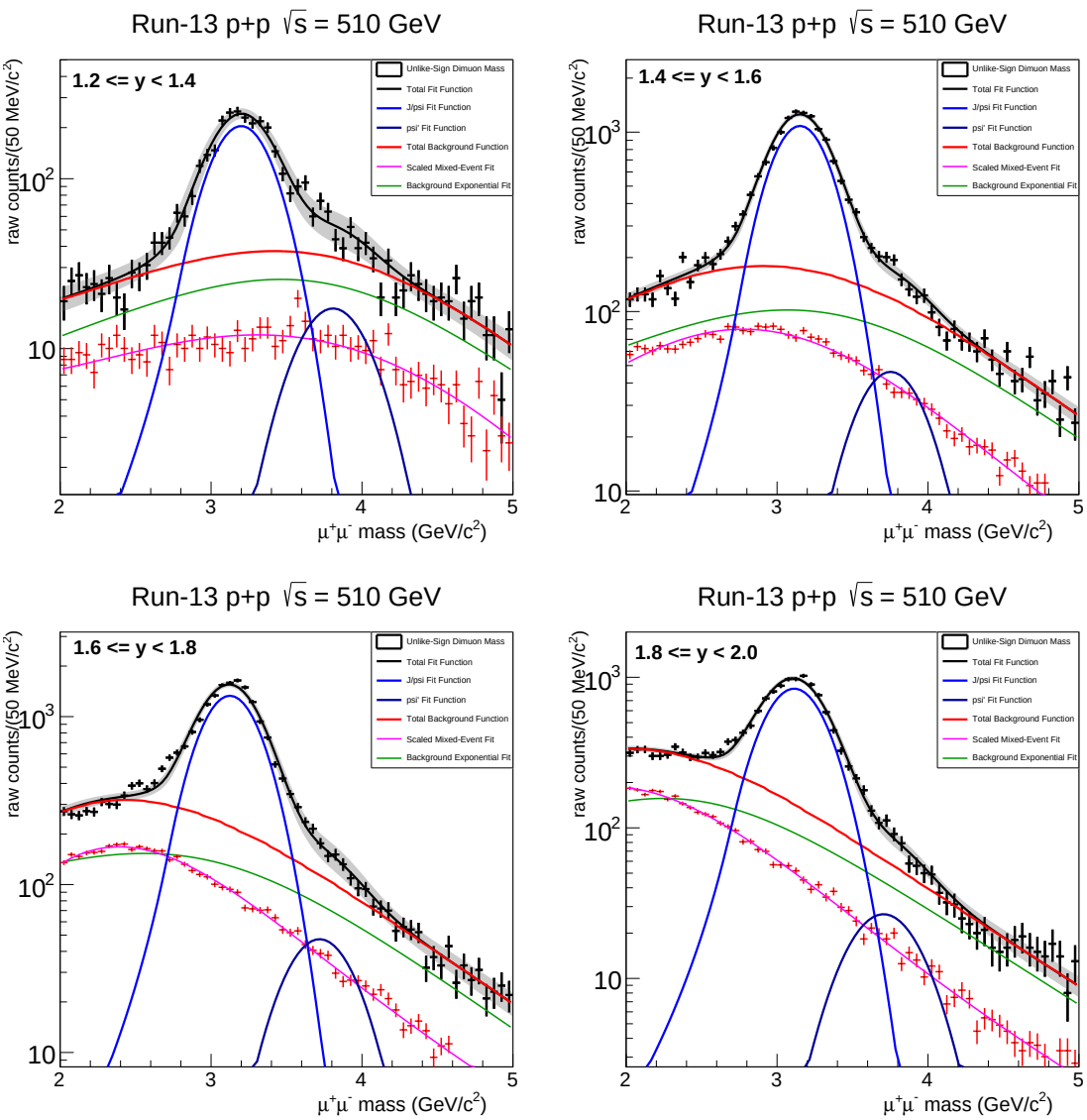

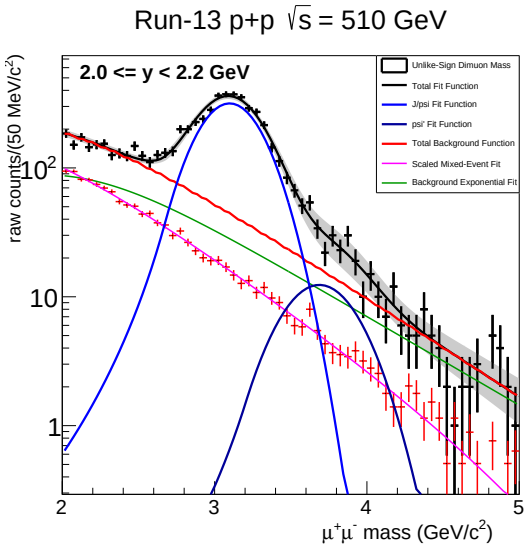

Figure D.-2: South arm dimuon mass spectrum for transverse momentum bins from 0 to 12 GeV. The J/ψ and $\psi\prime$ mass peaks are each fit with a Gaussian plus a crystal ball function. The mixed event backgroun

D.4 South Arm p_T Integrated Rapidity Bins

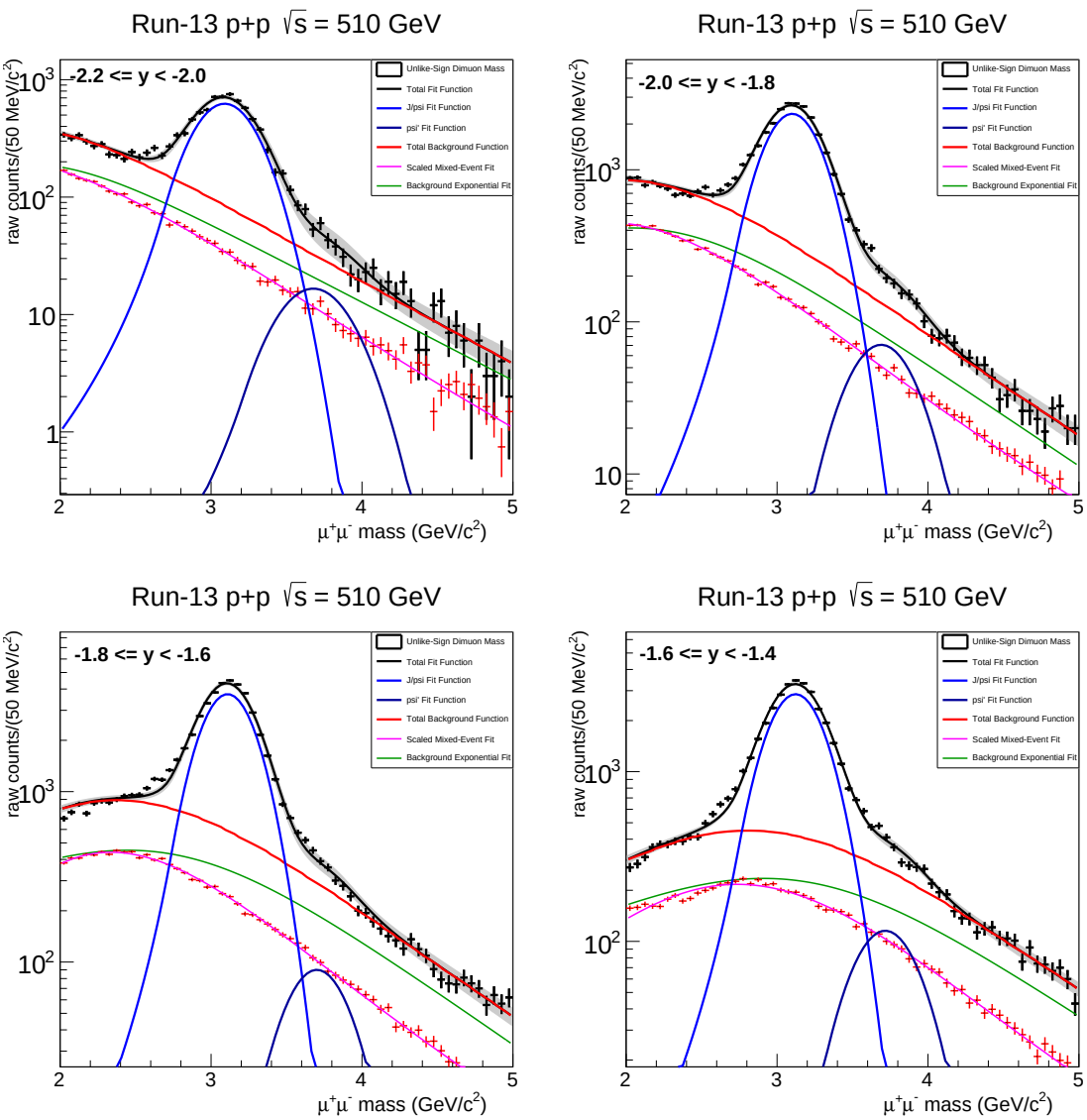

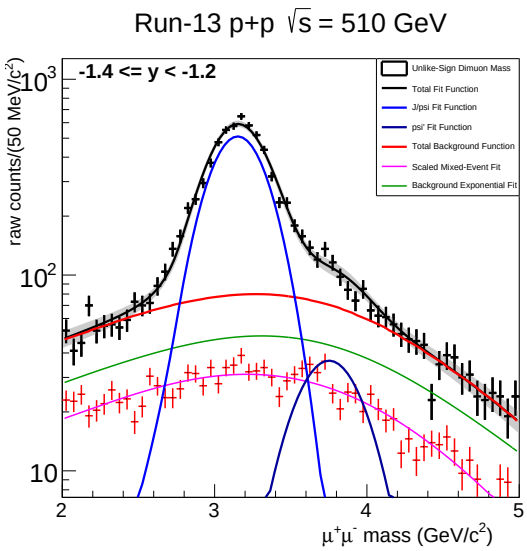

Figure D.-2: South arm dimuon mass spectrum for transverse momentum bins from 0 to 12 GeV. The J/ψ and $\psi\prime$ mass peaks are each fit with a Gaussian plus a crystal ball function. The mixed event backgroun

Appendix E

MuID2D Scaled Runs

Run	Scale Factor
388978	1
391169	1
391291	1
391442	1
391566	1
391722	1
391813	5
391815	1
391982	1
392015	1
393478	2
394048	1
394417	1
394526	1
394682	5
394683	1
394739	1
394962	1
395587	1
395639	1
395731	1
395882	1
396056	1
396760	1
396993	1
397290	1
397989	1
398005	1
398130	1

Table E.1: Runs that have a scale down factor for the MuID2D trigger have the number of events recorded by the DAQ scaled down by ScaleFactor + 1. The total luminosity counted by the Minimum Bias trigger must then be corrected for runs with scale down factors.

References

[1] M. Harrison, T. Ludlam, and S. Ozaki. Rhic project overview. *Nuclear Instruments and Methods in Physics Research Section A: Accelerators, Spectrometers, Detectors and Associated Equipment*, 499(2):235 – 244, 2003. The Relativistic Heavy Ion Collider Project: RHIC and its Detectors.

[2] H. Hahn et al. The rhic design overview. *Nuclear Instruments and Methods in Physics Research Section A: Accelerators, Spectrometers, Detectors and Associated Equipment*, 499(2):245 – 263, 2003. The Relativistic Heavy Ion Collider Project: RHIC and its Detectors.

[3] Robert Rathbun Wilson. The Tevatron. *Phys. Today*, 30N10:23–30, 1977.

[4] A. Adare et al. Ground and Excited Charmonium State Production in $p + p$ Collisions at $\sqrt{s} = 200$ GeV. *Phys. Rev.*, D85:092004, 2012.

[5] M. Krämer. Quarkonium production at high-energy colliders. *Progress in Particle and Nuclear Physics*, 47(1):141 – 201, 2001.

[6] Yan-Qing Ma and Raju Venugopalan. Comprehensive Description of J/ψ Production in Proton-Proton Collisions at Collider Energies. *Phys. Rev. Lett.*, 113:192301, 2014.

[7] Yan-Qing Ma, Kai Wang, and Kuang-Ta Chao. $J/\psi(\psi')$ Production at the Tevatron and LHC at $\mathcal{O}(\alpha_s^4 v^4)$ in Nonrelativistic QCD. *Phys. Rev. Lett.*, 106:042002, 2011.

[8] Chris Quigg. *Gauge Theories of the Strong, Weak, and Electromagnetic Interactions*, volume 56 of *Frontiers in Physics*. The Benjamin/Cummings Publishing Company, Inc., 1983.

[9] K. A. Olive et al. (Particle Data Group). Review of Particle Physics. *Chinese Physics C*, 38(9):090001, 2014.

[10] M. Gell-Mann. A Schematic Model of Baryons and Mesons. *Physics Letters*, 8(3):214–215, 1964.

[11] G Zweig. An SU_3 Model for Strong Interaction Symmetry and its Breaking; Version 2. (CERN-TH-412):80 p, Feb 1964. Version 1 is CERN preprint 8182/TH.401, Jan. 17, 1964.

[12] David Griffiths. *Introduction to Elementary Particles*. Wiley-VCH Verlag GmbH & Co., second edition, 2008.

[13] D. J. Gross and F. Wilczek. Ultraviolet Behavior of Non-Abelian Gauge Theories. *Physical Review Letters*, 30:1343–1346, June 1973.

[14] H. D. Politzer. Reliable Perturbative Results for Strong Interactions? *Physical Review Letters*, 30:1346–1349, June 1973.

[15] I.J.R. Aitchison, A.J.G. Hey. *Gauge Theories in Particle Physics*. Graduate Student Series in Physics. Adam Hilger, Ltd, 1982.

[16] B.R. Martin. *Nuclear and Particle Physics: An Introduction*. John Wiley & Sons, 2006.

[17] F. Halzen, A.D. Martin. *Quarks and Leptons: An Introductory Course in Modern Particle Physics*. John Wiley & Sons, 1984.

[18] J. Collins. *Foundations of Perturbative QCD*. Cambridge University Press, March 2011.

[19] J.J. Thomson. On the Structure of the Atom. *The London, Edinburgh, and Dublin Philosophical Magazine and Journal of Science*, 7(39):237–265, March 1904.

[20] Professor E. Rutherford F.R.S. LXXIX. The Scattering of α and β Particles by Matter and the Structure of the Atom. *Philosophical Magazine Series 6*, 21(125):669–688, 1911.

[21] S.L. Glashow Howard Georgi. Unity of All Elementary-Particle Forces. *Physical Review Letters*, 32(8):438–441, February 1974.

[22] P.D.B. Collins and A.D. Martin. *Hadron Interactions*. Graduate Student Series in Physics. Adam Hilger Ltd., Bristol, 1984.

[23] Carleton E. DeTar. Momentum Spectrum of Hadronic Secondaries in the Multiperipheral Model. *Phys. Rev. D*, 3:128–144, 1971.

[24] H. Abramowicz et al. Combination of Measurements of Inclusive Deep Inelastic $e^{\pm}p$ Scattering Cross Sections and QCD analysis of HERA data. *The European Physical Journal C*, 75(12):580, 2015.

[25] Vladimir Chekelian. Proton Structure and Parton Distribution Functions from HERA. *EPJ Web Conf.*, 126:02005, 2016.

[26] C.G. Callan Jr. and D.J. Gross. High-Energy Electroproduction and the Constitution of the Electric Current. *Phys. Rev. Lett., 22: 156-9 (Jan. 27, 1969).*, Jan 1969.

[27] J. D. Bjorken. Asymptotic Sum Rules at Infinite Momentum. *Phys. Rev.*, 179:1547–1553, 1969.

[28] J. D. Bjorken and Emmanuel A. Paschos. Inelastic Electron Proton and gamma Proton Scattering, and the Structure of the Nucleon. *Phys. Rev.*, 185:1975–1982, 1969.

[29] R. Brandelik et al. Evidence for Planar Events in e+e Annihilation at High Energies. *Phys. Lett. B*, 86:243–249, 1979.

[30] C. Berger et al. Evidence for Gluon Bremsstrahlung in e+e Annihilation at High Energies. *Phys. Lett. B*, 86:418–425, 1979.

[31] W. Bartel et al. Observation of Planar Three-Jet Events in e+e Annihilation and Evidence for Gluon Bremsstrahlung. *Phys. Lett. B*, 91:142–147, 1979.

[32] M. Jonker et al. Experimental study of neutral-current and charged-current neutrino cross sections. *Phys. Lett. B*, 99(3):265 – 270, 1981.

[33] Henry W. Kendall. Deep Inelastic Scattering: Experiments on the Proton and the Observation. *Rev. Mod. Phys.*, 63:597–614, 1991.

[34] Jerome I. Friedman. Deep Inelastic Scattering: Comparisons with the Quark Model. *Rev. Mod. Phys.*, 63:615–629, 1991.

[35] Richard E. Taylor. Deep Inelastic Scattering: The Early years. *Rev. Mod. Phys.*, 63:573–595, 1991.

[36] Aaron, F. D. et. al. Combined Measurement and QCD analysis of the Inclusive $e^{\pm}p$ Scattering Cross Sections at HERA. *Journal of High Energy Physics*, 2010(1):109, 2010.

[37] A. D. Martin, W. J. Stirling, R. S. Thorne, and G. Watt. Parton distributions for the LHC. *Eur. Phys. J.*, C63:189–285, 2009.

[38] R. Keith Ellis et al. Factorization and the Parton Model in QCD. *Physics Letters B*, 78(2):281 – 284, 1978.

[39] J. C. Collins, D. E. Soper, and G. Sterman. Soft Gluons and Factorization. *Nuc. Phys. B*, 308:833, 1988.

[40] J. J. Aubert et al. Experimental Observation of a Heavy Particle J. *Phys. Rev. Lett.*, 33:1404–1406, 1974.

[41] Samuel C C Ting. The Discovery of the J Particle; A Personal Recollection. *Physica Scripta*, 15(1):7, 1977.

[42] J. E. Augustin et al. Discovery of a Narrow Resonance in e^+e^- Annihilation. *Phys. Rev. Lett.*, 33:1406–1408, 1974. [Adv. Exp. Phys.5,141(1976)].

[43] Nobelprize.org Nobel Media AB 2014. The Nobel Prize in Physics 1976. http://www.nobelprize.org/nobel_prizes/physics/laureates/1976.

[44] S. Okubo. Consequences of Quark Line (Okubo-Zweig-Iizuka) Rule. *Phys. Rev.*, D16:2336–2352, 1977.

[45] C. Patrignani et al. (Particle Data Group). *Chin. Phys. C,*, 40(100001), 2016.

[46] Stanley J. Brodsky and Jean-Philippe Lansberg. Heavy-Quarkonium Production in High Energy Proton-Proton Collisions at RHIC. *Phys. Rev.*, D81:051502, 2010.

[47] S. Okubo. ϕ-Meson and Unitary Symmetry Model. *Physics Letters*, 5(2):165 – 168, 1963.

[48] G. Zweig. An SU(3) Model for Strong Interaction Symmetry and its Breaking. Version 2. In D.B. Lichtenberg and Simon Peter Rosen, editors, *Developments in the Quark Theory of Hadrons. Vol. 1. 1964- 1978*, pages 22–101. 1964.

[49] J. Iizuka, K. Okada, and O. Shito. Systematics and Phenomenology of Boson Mass Levels. III. *Progr. Theoret. Phys. (Kyoto)*, Vol: 35, Jun 1966.

[50] M.B. Einhorn and S.D. Ellis. Hadronic Production of the New Resonances: Probing Gluon Distributions. *Physi. Rev. D.*, 12(7):2007, 1975.

[51] R. Baier and R. Ruckl. Hadronic Production of J/ψ and Υ: Transverse Momentum Distributions. *Phys. Lett.*, B102:364, 1981.

[52] H. Fritzsch. Producing Heavy Quark Flavors in Hadronic Collisions: A Test of Quantum Chromodynamics. *Phys. Lett.*, B67:217, 1977.

[53] J. F. et al. Amundson. Quantitative Tests of Color Evaporation: Charmonium Production. *Physics Letters B*, 390:323–328, February 1997.

[54] G. T. Bodwin, E. Braaten, and G. P. Lepage. Rigorous QCD Analysis of Inclusive Annihilation and Production of Heavy Quarkonium. *Phys. Rev. D*, 51:1125, 1995. Erratum-ibid. D 55 (1995).

[55] N. Brambilla et al. Heavy Quarkonium: Progress, Puzzles, and Opportunities. *Eur. Phys. J. C*, 71(arXiv:1010.5827. TUM-EFT 11-10. CLNS 10-2066. ANL-HEP-PR-10-44. ALBERTA THY 11-10. CP3-10-37. FZJ-IKP-TH-2010-24. INT-PUB-10-059):1534. 181, Oct 2010.

[56] B. Gong, X. Q. Li, and J. X. Wang. QCD Corrections to J/ψ Production via Color Octet States at Tevatron and LHC. *Phys. Lett.*, B673:197–200, 2009.

[57] F. Abe et al. J/ψ adn $\psi(2s)$ Production in $p\bar{p}$ Collisions at $\sqrt{s} = 1.8$ TeV. *Phys. Lett. B*, 79:572, 1997.

[58] F. Abe et al. Production of J/ψ Mesons from χ_c Meson decays in $p\bar{p}$ Collisions at $\sqrt{s} = 1.8$ TeV. *Phys. Lett. B*, 79:578, 1997.

[59] J. P. Lansberg. QCD Corrections to J/ψ Polarisation in pp Collisions at RHIC. *Physics Letters B*, 695:149–156, January 2011.

[60] A.D. Frawley, T. Ullrich, and R. Vogt. Heavy Flavor in Heavy-Ion Collisions at RHIC and RHIC II. *Physics Reports*, 462(4–6):125 – 175, 2008.

[61] Mathias Butenschön and Bernd A. Kniehl. Reconciling J/ψ Production at HERA, RHIC, Tevatron, and LHC with Nonrelativistic QCD Factorization at Next-to-Leading Order. *Phys. Rev. Lett.*, 106:022003, Jan 2011.

[62] Matteo Cacciari, Paolo Nason, and Ramona Vogt. QCD Predictions for Charm and Bottom Quark Production at RHIC. *Phys. Rev. Lett.*, 95:122001, Sep 2005.

[63] Fred Cooper, Ming X. Liu, and Gouranga C. Nayak. J/Ψ. *Phys. Rev. Lett.*, 93:171801, Oct 2004.

[64] Leonard S. Kisslinger and Debasish Das. J/ψ, ψ(2S) Production in pp Collisions at $E = 510$ GeV. *Int. J. Theor. Phys*, 54:2737, 2015.

[65] Leonard S. Kisslinger, Ming X. Liu, and Patrick McGaughey. Heavy-quark-State Production in $p - p$ collisions. *Phys. Rev. D*, 84:114020, Dec 2011.

[66] G.W. Wheeler et al. The Brookhaven 200-MeV Proton Linear Accelerator. *Particle Accelerators*, 9:1–156, 1979.

[67] AGS Booster Project, Accelerator Development Department, Brookhaven National Laboratory, Upton, NY. *Booster Design Manual*, 1988.

[68] Associated Universities Inc. Alternate Gradient Synchrotron Project Construction Completion Report. Technical report, Brookhaven National Laboratory, Upton, NY, December 1966.

[69] Accelerator Division. *RHIC Configuration Manual*. Collider-Accelerator Department, Brookhaven National Laboratory, Upton, NY, September 2006.

[70] I. Alekseev et al. *Configuration Manual, Polarized Proton Collider at RHIC*. Brookhaven National Laboratory, Upton, NY, January 2006.

[71] M. Anerella et al. The RHIC Magnet System for NIM . 610-20 (AM-MD-311), 2001.

[72] Peter Cameron et al. The rhic wall current monitor system. volume 3, pages 2146 – 2148 vol.3, 02 1999.

[73] J. Claus. Beam position monitor for rhic. 9 1988.

[74] D. Bruno et al. Rhic magnet electrical system. *Nuclear Instruments and Methods in Physics Research Section A: Accelerators, Spectrometers, Detectors and Associated Equipment*, 499(2):316 – 348, 2003. The Relativistic Heavy Ion Collider Project: RHIC and its Detectors.

[75] K. Adcox et al. PHENIX Detector Overview. *Nucl. Instr. and Meth.*, A499:469–479, 2003.

[76] M. Allen et al. PHENIX Inner Detectors. *Nucl. Instr. and Meth.*, A499:549–559, 2003.

[77] S.H. Aronson et al. PHENIX Magnet System. *Nucl. Instr. and Meth.*, A499:480–488, 2003.

[78] L. Aphecetche et al. The PHENIX Calorimeter. *Nucl. Instr. and Meth.*, A499:521–536, 2003.

[79] K. Adcox et al. PHENIX Central Arm Tracking Detectors. *Nucl. Instr. and Meth.*, A499:489–507, 2003.

[80] M. Aizawa et al. PHENIX Central Arm Particle I.D. Detectors. *Nucl. Instr. and Meth.*, A499:508–520, 2003.

[81] H. Akikawa et al. PHENIX Muon Arms. *Nucl. Instr. and Meth.*, A499:537–548, 2003.

[82] S.S. Adler et al. PHENIX On-line Systems. *Nucl. Instr. and Meth.*, A499:560–592, 2003.

[83] S.S. Adler et al. PHENIX On-line and Off-line Computing. *Nucl. Instr. and Meth.*, A499:593–5602, 2003.

[84] C. Aidiala et al. The PHENIX Forward Silicon Vertex Detector. *Nucl. Instr. and Meth.*, A755:44–61, aug 2014.

[85] Jin Huang, 2011. Photograph for the PHENIX collaboration.

[86] T. Aaltonen et al. Operational Experience, Improvements, and Performance of the CDF Run II Silicon Vertex Detector. *Nucl. Instr. and Meth.*, A729:153–181, 2013.

[87] S.N. Ahmed et al. The D0 Silicon Microstrip Tracker. *Nucl. Instr. and Meth.*, A634(1):8–46, 2011.

[88] F. Hartmann. Silicon Tracking Detectors in High-Energy Physics. *Nucl. Instr. and Meth.*, A666:25–46, 2012.

[89] Paul W. Lisowski and Kurt F. Schoenberg. The Los Alamos Neutron Science Center. *Nucl. Instr. and Meth.*, A562(2):910–914, 2006.

[90] J. Asai et al. Radiation Damage Study of Silicon Stripixel Sensor (for PHENIX Experiment). *International Journal of Modern Physics E*, 16(07n08):2535–2540, 2007.

[91] T. Aaltonen et al. Operational experience, improvements, and performance of the cdf run ii silicon vertex detector. *Nuclear Instruments and Methods in Physics Research Section A: Accelerators, Spectrometers, Detectors and Associated Equipment*, 729:153 – 181, 2013.

[92] A. Adare et al. $\Upsilon(1S + 2S + 3S)$ Production in d+Au and $p + p$ Collisions at $\sqrt{s_{NN}} = 200$ GeV and Cold-Nuclear Matter Effects. *Phys. Rev.*, C87(4):044909, 2013.

[93] A. Adare et al. Measurement of the Relative Yields of $\psi(2S)$ to $\psi(1S)$ Mesons Produced at Forward and Backward Rapidity in $p + p$, p + Al, p + Au, and ^{3}He + Au Collisions at $\sqrt{s_{NN}} = 200$ GeV. *Phys. Rev. C*, 95:034904, Mar 2017.

[94] J.E. Gaiser. *Appendix-F Charmonium Spectroscopy from Radiative Decays of the J/ψ and $\psi\prime$*. PhD thesis, Stanford University, 1982. SLAC-R-255.

[95] H.J. Oreglia. *A Study of the Reactions of the $\psi\prime \to \gamma\gamma\psi$*. PhD thesis, Stanford University, 1980. SLAC-R-255, Appendix D.

[96] T. Skwarnicki. *A Study of the Radiative Cascade Transitions between the $\Upsilon\prime$ and Υ Resonances*. PhD thesis, DESY F31-86-02, 1986. Appendix E.

[97] Matt Durham et al. Run 13 $\psi(2s) \to \mu^+\mu^-$ with the FVTX. PHENIX Analysis Note 1185, 2014.

[98] Torbjörn Sjöstrand et al. High-energy-physics event generation with Pythia 6.1. *Computer Physics Communications*, 135(2):238 – 259, 2001.

[99] René Brun et al. *GEANT: Detector Description and Simulation Tool; Oct 1994*. CERN Program Library. CERN, Geneva, 1993. Long Writeup W5013.

[100] Alexander Bazilevsky et al. Central Arm W Analysis. PHENIX Analysis Note 923, 2011.

[101] A. Manion. Method For Determining Relative Luminosity From Detection Probabilities (Run9 200 GeV). PHENIX Analysis Note 953, 2013.

[102] M. Chiu et al. New Ideas on Relative Luminosity Determination in Run09 500 GeV Polarized Proton Collisions. PHENIX Analysis Note 1184, 2014.

[103] Sanghoon Lim and Matt Durham. Inclusive J/ψ at Muon Arms in Small Collision Systems. PHENIX Analysis Note 1354, 2018.

[104] P. McGaughey. Private Communication.

[105] A. et al Adare. j/ψ production versus transverse momentum and rapidity in $p+p$ collisions at $\sqrt{s} = 200$ GeV. *Phys. Rev. Lett.*, 98:232002, 2007.

[106] Gregory Ottino. Vernier Scan Analysis for PHENIX Run 15 $p+p$ Collisions at $\sqrt{s} = 200$ GeV, 2017. Honor's Thesis, University of New Mexico.

[107] G. Ottino and K. DeBlasio. Vernier Scan Analysis for Run 15 p+p Collisions, $\sqrt{s} = 200$ GeV.

[108] S van der Meer. Calibration of the effective beam height in the ISR. *CERN-ISR-P0-68-31*, 01 1968.

[109] K.A. Drees and T. D'Ottavio. Results from Vernier Scans during the RHIC 2008 PP Run. In *Proceedings of PAC09*, pages 2480–2482, 2009.

[110] A. Drees. Analysis of Vernier Scans during RHIC Run 13. Technical report, Collider-Accelerator Department, Brookhaven National Laboratory, Oct 2013. 10.2172/1104828.

[111] Amaresh Datta and Dave Kawall. σ_{BBC} Using Vernier Scans for 500 GeV pp. PHENIX Analysis note on the Run 9 Vernier Scan, sep 2010.

[112] D. Kawall and A. Datta. Relative Luminosity Considerations . https://www.phenix.bnl.gov/WWW/p/draft/kawall/pwg/pwg090304dmk.pdf, Mar. 2009.

[113] Scott Justin Wolin et al. New Ideas on Relative Luminosity Determination in Run09 500 GeV Polarized Proton Collisions. PHENIX Analysis Note, apr 2014.

[114] Werner Herr and B Muratori. Concept of luminosity. 2006. http://cds.cern.ch/record/941318.